Soft ω-meson production in pp collision at $\sqrt{s}$= 5.02 TeV with ALICE

MASTER THESIS

Merle Luisa Wälde

20.08.2024

Institut für Kernphysik
Fachbereich Physik
Goethe Universität Frankfurt

Supervisor:
Prof. Dr. Harald Appelshäuser
Dr. Raphaelle Bailhache

Contents

1 Introduction

Heavy-ion collisions make it possible to study the smallest particles as well as the conditions at the beginning of our universe. Such heavy-ion collisions can be performed at the LHC (**L**arge **H**adron **C**ollider). Here, several dedicated experiments have been set up to study the matter produced in these collisions. One of these experiments is ALICE (***A** **L**arge **I**on **C**ollider **E**xperiment*), which was designed to investigate the properties of strongly interacting matter. In lead-lead (Pb–Pb) collisions, the energy density and temperature are high enough to produce a Quark-Gluon-Plasma (QGP). To be able to characterize and understand the particularity of the QGP, reference measurements in more elementary collisions (proton-proton(pp) or proton-lead (p–Pb)) where no QGP is expected are mandatory.
The measurement of neutral meson production in pp collisions is important as a reference for heavy-ion studies and to test our understanding of corresponding theories, like quantum chromodynamics (QCD). Especially in the low momentum range, the production rate of neutral mesons is a crucial input for measurements of direct photons and dielectrons.
The ω meson is published for different LHC energies by the ALICE collaboration, however, these measurements are limited in their p_{T} reach down to a few GeV/c. This thesis presents the ω measurement at midrapidity in pp collisions at $\sqrt{s} = 5.02$ TeV down to $p_{\mathrm{T}} = 0$, which is possible by using the $\omega \to \mathrm{e}^+\mathrm{e}^-$ decay channel, using data from the 2017 pp run measured by ALICE at a center-of-mass energy of $\sqrt{s} = 5.02$ TeV.

This thesis is structured as follows. It begins with a brief overview of hadrons and light mesons, with a particular focus on the ω meson with its dielectron decay. Next, a description of the ALICE subdetectors such as the ITS (Inner Tracking System), TPC (Time Projection Chamber), and TOF (Time of Flight), which are used for electron identification (see section 3), is provided. The dataset used and the selection criteria applied are detailed in section 4.1. Section 5 covers the analysis, including the signal extraction, correction of the ω signal, and details on the systematic uncertainties of different origins. The results are presented in section 6, and the thesis concludes with a summary and outlook in section 7.

2 Hadrons

Hadrons consist of elementary particles called quarks and are classified as subatomic particles, which are particles that are smaller than atoms, such as elementary particles (like electrons or quarks), or compositions of quarks into hadrons (like baryons, e.g. neutrons and protons, or mesons, e.g. ω). Elementary particles are the smallest known particles meaning they are not divisible into other particles and are characterized by intrinsic quantum numbers. Elementary particles are considered as point like objects, whereas a bound state of elementary particles has an internal structure [1].
In the **Standard Model** (SM) those elementary particles (quarks, leptons, and exchange particles) and the interacting forces between them are described. The SM includes three of the four fundamental forces, which are the electromagnetic, the strong, and the weak force. The SM doesn't include the fourth fundamental force, gravity, but is considered as the best theory to unite as many forces in one gauge theory. The search for the "ultimate theory of everything" is still ongoing [2].
Elementary particles can be subdivided into two groups: fermions and bosons. This categorization into fermion/bosons is done by the intrinsic angular momentum of the particles, called spin. Fermions have half-integer spin whereas bosons have integer spin values.
Quarks and leptons (+ anti-particles) are **fermions**. There are 12 particles in total, six of them quarks, and six leptons. Those can be grouped into three generations, the mass of the first generation is smaller than the second and those have smaller masses than the third generation. A set of two quarks and two leptons belongs to one generation, which differ by the charge. For the quarks the charges(Q) are $+\frac{2}{3}$ and $-\frac{1}{3}$, for the leptons the charge is either -1 or 0, the uncharged leptons are also called neutrinos. Anti-particles have the oppisite charge [2].

		d	u	s	c	b	t
Q	- electric charge	$-\frac{1}{3}$	$+\frac{2}{3}$	$-\frac{1}{3}$	$+\frac{2}{3}$	$-\frac{1}{3}$	$+\frac{2}{3}$
I	- isospin	$\frac{1}{2}$	$\frac{1}{2}$	0	0	0	0
I_z	- isospin z-component	$-\frac{1}{2}$	$+\frac{1}{2}$	0	0	0	0
S	- strangeness	0	0	-1	0	0	0
C	- charm	0	0	0	+1	0	0
B	- bottomness	0	0	0	0	-1	0
T	- topness	0	0	0	0	0	+1

Table 1: Additive quark quantum numbers [3].

In Tab. 1 the quark quantum numbers for all six quarks are shown. The quark flavour numbers (I_z, S, C, B, or T) have by conventions the same sign as its charge Q [3].
Contrary to fermions, **bosons** have integer spin. Bosons with spin=1 are called vector bosons. Bosons with Spin=0 are called scalar bosons, like e.g. the Higgs boson.
The three exchange particles of the weak force are Z^0 and $W^{\pm}$, which interact with left-handed fermions and right-handed antifermions, are responsible for the β-decay, and can change the flavour ("up", "down", ...) of quarks. Due to symmetry breaking, they have a mass of non-negligible size ($m_{Z^0} = 91.19$ GeV/c^2 and $m_{W^{\pm}} = 80.38$ GeV/c^2). The effective range of the weak force is limited to subatomic distances $\ll$ 1fm. The photon (γ) is the mass less exchange particle of the electromagnetic interaction with an infinite range. The strong interaction is described by the quantum chromodynamics (QCD). QCD is a quantum field

theory with SU(3) local gauge symmetry with three "colour" charges: red(R), blue(B) and green(G) (or anti-colors $\bar{R}$, $\bar{B}$, $\bar{G}$). Strongly interacting particles have this so-called colour charge, i.e. quarks(one colour charge) and gluons (colour and anti-colour charge). The gluon is the mass less exchange particle of the strong interaction, with a range of $\approx$ 1fm. There are $N_c^2 - 1 = 8$ non-Abelian gauge fields, i.e. gluons. Both quarks and gluons are confined in colorless states, so-called hadrons [3].
These colorless states are realized in bound states - hadrons, so either baryons or mesons.
The bound state of **baryons** consists of usually three quarks (qqq). Other "exotic" states of an odd number of quarks are for example a tetraquark state. Baryons are colorless states in which quarks and gluons are confined. Known baryons are the constituents of nuclei, neutrons(udd) and protons(uud), which are composed of first-generation quarks *up* and *down*. Baryons are due to their half-integer spin also fermions.
For this analysis, important hadrons are **mesons**, bound states of quark and anti-quark pairs ($q\bar{q}$), also colorless states. Heavier mesons decay into light mesons, which then decay into electrons, neutrinos, and photons. Due to their integer spin mesons are also bosons, with parallel (spin = 1) or anti-parallel (spin = 0) alignment of their constituent quarks.

Mesons and baryons can be classified in J^{PC} multiplets, with the spin J given by $|l - s| \geq J \geq |l + s|$ (s quark spin, l orbital angular momentum of the hadron), the spatial parity $P = (-1)^{l+1}$ and the charge parity $C = (-1)^{l+s}$. Here, P and C in the J^{PC} multiplets can be either even (+) or odd (−).

2.1 Light mesons

Light mesons are mesons constituted of the three lightest quarks u, d, and s. There are a total of 9 combinations of all three light-flavour quarks and three anti-quarks with each other.
These can be classified in J^{PC} multiplets. The $l = 0$ states are differentiated into pseudoscalars (0^{-+}) and vectors (1^{--}) mesons. In Figure 2.1 the nonet with the corresponding mesons for both pseudoscalar and vector mesons are shown. The mesons are divided according to the flavour numbers Isospin (I_3), Strangeness (S) as well as the electric charge ($Q = I_3 + \frac{1}{2}S$). While I_3 is the flavour number related to the first generation quarks u ($I_3 = +\frac{1}{2}$) and d ($I_3 = -\frac{1}{2}$), the Strangeness is the flavour number for the s-quarks with ($S = -1$).

In Table 2 the quark compositions for the ground-state ($l = 0$) light mesons are shown for the pseudoscalar (0^{-+}) and vector (1^{--}) mesons. For the $I_3 = 0$ states ($u\bar{u}, d\bar{d}, s\bar{s}$) f' and f are the functions of the mixtures of these states, defined in Eq. 2.1. Here the mesons with the light quark states with the same J^{PC} mix. Mixing with the heavier quarks (charmonium and bottonium) are assumed to be negligible [3].

The $I = 0$ states of the pseudoscalar (η and η') and the vector (ω and ϕ) mesons are underlying a flavour-symmetric interaction for mixing $q\bar{q}$ configurations of different flavours ($u\bar{u} \leftrightarrow d\bar{d} \leftrightarrow s\bar{s}$). This mixing of states is given by the following functions f' and f, with:

$$\begin{aligned} f' &= \psi_8 \cos\theta - \psi_1 \sin\theta, \\ f &= \psi_8 \sin\theta + \psi_1 \cos\theta, \end{aligned} \tag{2.1}$$

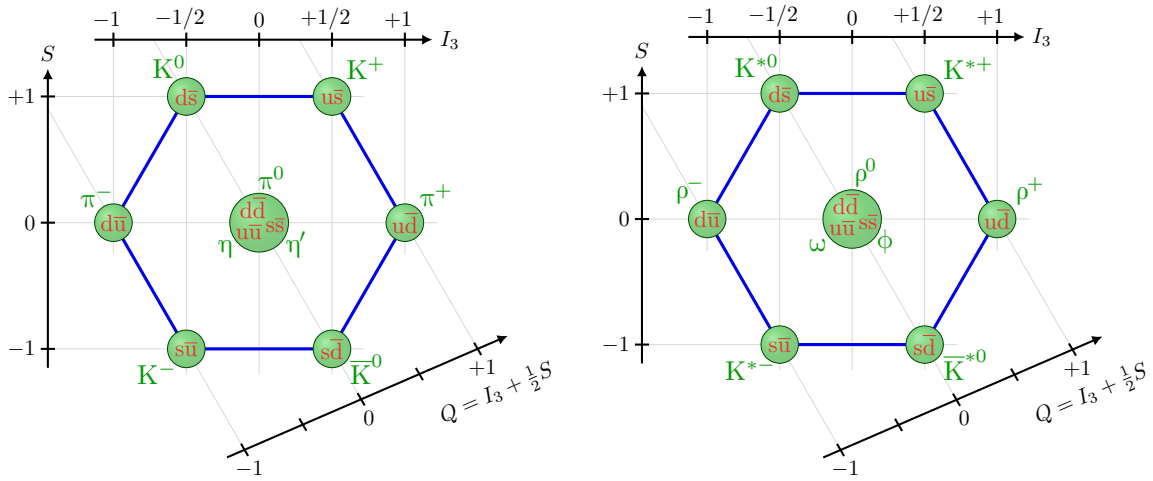

Figure 2.1: Nonet of light-flavour mesons : pseudoscalar (left) and vector (right) [4].

$n^{2s+1}l_J$	J^{PC}	I = 1	I = $\frac{1}{2}$	I = 0	I = 0
		$u\bar{d}, \bar{u}d,$	$u\bar{s}, \bar{u}s,$	f'	f
		$\frac{1}{\sqrt{2}}(d\bar{d} - u\bar{u})$	$d\bar{s}, \bar{d}s$		
1^1S_0	0^{-+}	π	K	$\eta(547)$	$\eta'(958)$
1^3S_1	1^{--}	$\rho(770)$	K^*	$\phi(1020)$	$\omega(782)$

Table 2: Suggested $q\bar{q}$ states from the quark model with the lightest mesons u,d, and s quarks for $l = 0$ [3]

.

the mixing angle θ and the wave functions ψ_1 and ψ_8:

$$\begin{aligned} \psi_8 &= \frac{1}{\sqrt{6}}(u\bar{u} + d\bar{d} - 2s\bar{s}), \\ \psi_1 &= \frac{1}{\sqrt{3}}(u\bar{u} + d\bar{d} + s\bar{s}). \end{aligned} \tag{2.2}$$

The "ideal" mixing angle is $\theta_i = \frac{1}{\sqrt{2}}$ (or $\theta_i = 35.3°$) for the decoupling of the $u\bar{u} + d\bar{d}$ and $s\bar{s}$ components [3].
The mixing angle of the mesons can then be calculated using the following relation:

$$\tan^2(\theta) = \frac{4m_K - m_a - 3m_{f'}}{-4m_K + m_a + 3m_f}, \tag{2.3}$$

with the index K for $I = \frac{1}{2}$ states and the index a for $I = 1$ states.

2.2 ω meson

The ω meson is an isoscalar light-flavour state with a pole mass of $m_\omega = (782.66 \pm 0.13)$ MeV/c^2 [3]. As already mentioned above the $I = 0$ states are mixed states of the light-flavour $q\bar{q}$ configurations. The mixing angle of the ground-state vector mesons ($\omega = f$ and $\phi = f'$) can then be calculated with the Eq. 2.3, using the published vector meson masses from the

particle data group (PDG) [3] with $m_K = m_{K^*} \simeq 895$ MeV/c^2, $m_a = m_\rho \simeq 775$ MeV/c^2, $m_{f'} = m_\phi \simeq 1019$ MeV/c^2 and $m_f = m_\omega \simeq 782$ MeV/c^2. The mixing angle of the vector mesons ω and ϕ is then $\theta_V \simeq 36.5°$. Thus the mixing angle is almost the "ideal" mixing angle, it follows with Eq. 2.1 that ϕ is a pure $s\bar{s}$ state whereas ω has nearly no strange mixing contributions. The wave function of the ω meson is then $|\omega\rangle = \frac{1}{\sqrt{2}}\langle|u\bar{u}\rangle + \left|d\bar{d}\right\rangle\rangle$.

The average life time of the ω is quite short with $\tau_\omega = \frac{\hbar}{\Gamma_\omega} = (7.58 \pm 0.11)10^{-23}$s, calculated with the full width $\Gamma_\omega = (8.68 \pm 0.13)$ MeV/c^2 provided by the PDG [3].
The ω decays via different decay channels, the most probable of them is the $\omega \to \pi^+\pi^-\pi^0$ decay with a branching ratio of 89%. The next probable decay channel is with 8% via the decay $\omega \to \pi^0\gamma$. Some of the decay modes are presented in Tab. 3, one of the smallest branching ratios with 0.0074% is the $\omega \to \mathrm{e}^+\mathrm{e}^-$ decay channel.

$\omega \to \pi^+\pi^-\pi^0$	89.20 %
$\omega \to \pi^0\gamma$	8.35 %
$\omega \to \pi^+\pi^-$	1.53 %
...	
$\omega \to \pi^0 e^+e^-$	0.077 %
$\omega \to e^+e^-$	0.0074 %
...	

Table 3: Decay channels of the ω meson [3].

2.2.1 Published measurements

The ω meson can be reconstructed by the daughter particles of the decays. The ω was measured in pp collisions at several collision energies by the ALICE and PHENIX collaborations. The ALICE collaboration published a ω meson measurement in pp collisions at $\sqrt{s} = 7$ TeV (from 2020 [5]) provided by a reconstruction of ω via the $\omega \to \pi^+\pi^-\pi^0$ decay channel in $(2 < p_\mathrm{T} < 17)$ GeV/c. Furthermore, preliminaries are available for pp and p–Pb collisions at $\sqrt{s} = 5.02$ TeV, where the ω meson is reconstructed using the $\omega \to \pi^+\pi^-\pi^0$ decay channel [6].
The PHENIX collaboration published in 2011 the measurement of ω production in pp collisions at $\sqrt{s} = 200$ GeV, reconstructed via multiple decay channels: $\omega \to \pi^+\pi^-\pi^0$ in $(2 < p_\mathrm{T} < 13.5)$GeV/$c$, $\omega \to \pi^0\gamma$ in $(2 < p_\mathrm{T} < 12)$ GeV/c and $\omega \to \mathrm{e}^+\mathrm{e}^-$ in $(0 < p_\mathrm{T} < 4)$ GeV/c [7]. As one can see, the ω measurements that are already published are limited at low p_T, except when the $\omega \to \mathrm{e}^+\mathrm{e}^-$ decay channel is used for the reconstruction. At LHC energies, there is no publication down to $p_\mathrm{T} = 0$ available.

Dielectron decay $\omega \to e^+e^-$

The dielectron decay channel is very rare compared to other decay channels, but reconstructing the ω meson via this decay channel has the advantage that only two particles are needed for reconstruction. Moreover, dielectrons do not participate in the strong interaction and thus the dielectron decay channel has the advantage to not be affected by final-state interactions of the decay particles contrary to the other decay channels with strongly interacting daughter particles. Although the ω decay into three pions is very probable, it is not more suitable than the measurement via the dielectron decay channel due to the strongly

interacting pions, but also due to the reconstruction via more than two particles. Here, the reconstruction of ω via the three-pion decay channel is suitable for high p_{T} ranges, while the reconstruction for the dielectron decay channel is suitable for lower p_{T} ranges.

Hadronic cocktail of dielectron sources

The $\mathrm{e^+e^-}$ decay channel is a decay channel for many mesons. The signal of all hadronic sources decaying into dielectron pairs (+ other) are represented by the dielectron spectrum measurements. In Figure 2.2 the measured dielectron cross-section for pp collisions at $\sqrt{s} =$ 5.02 TeV is shown as the blue markers [8]. The expected hadronic contributions of the different dielectron sources are summed up in the so-called hadronic cocktail sum, here shown as the black line. This sum is composed of light-flavour as well as heavy-flavour contributions.

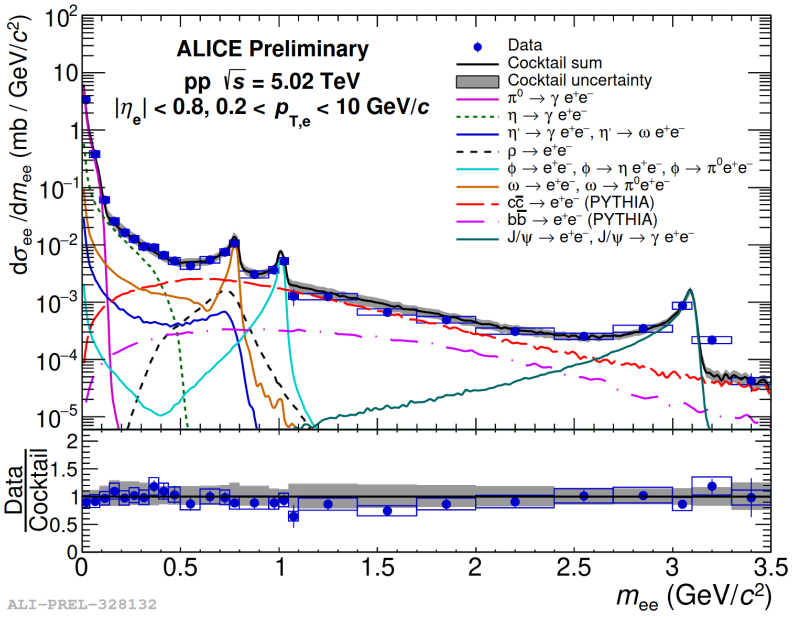

Figure 2.2: Cross section of dielectron production in pp collisions as a function of the $\mathrm{e^+e^-}$ - invariant mass measured at $\sqrt{s} = 5.02$ TeV [8].

Next to the resonance peaks of J/ψ ($\simeq 3096$ MeV/c^2) [3] , as well as the ϕ ($\simeq 1019$ MeV/c^2) meson, is the resonance peak of the ω ($\simeq 782$ MeV/c^2) clearly visible. Due to this a peak-based yield extraction of the ω signal is possible. The ω signal for the dielectron decay as well as the $\omega \rightarrow \pi^0\mathrm{e^+e^-}$ decay is shown as an orange line. Underneath the ω signal are other contributions that are added to the expected hadronic cocktail sum. The main contributors here are from the ρ black dashed line) as well as open-charm (red dashed line) contributions.

3 ALICE

There are four major experiments at the particle accelerator Large Hadron Collider (LHC): ATLAS, CMS, LHCb, and ALICE. ALICE, which stands for **A** **L**arge **I**on **C**ollider **E**xperiment, is a dedicated heavy-ion experiment. In 2009, ALICE detected the first collision events. Since then, the Collaboration has been provided with large data sets to analyse and study strongly interacting matter at high energy densities and temperatures, conditions achieved in Pb–Pb collisions. Reference measurements are also performed in p–Pb and pp collisions, where no hot medium is a priori expected [9]. The following section describes the ALICE detector setup during the LHC Run 2, focusing on the subdetectors required for this analysis.

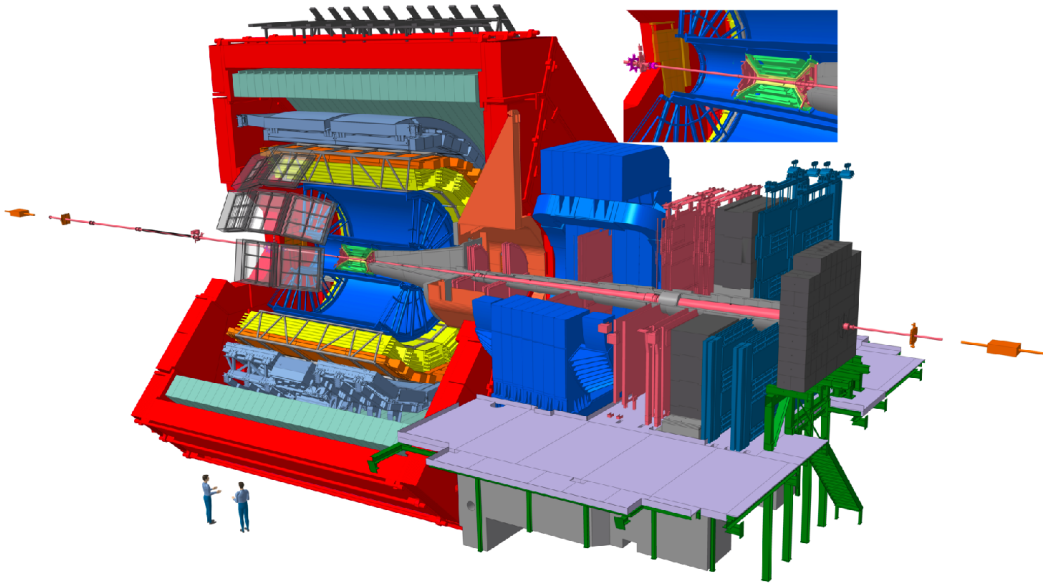

Figure 3.1: Schematic illustration of the ALICE detectors, consisting of the central barrel encased by the L3 magnet (red) and the muon arm built in the forward direction around the beam pipe [10].

The ALICE experiment consists of several subdetector layers, as shown in Figure 3.1. For this analysis, the detectors used for the track selection and particle identification (PID) of electron candidates are the **ITS** (Inner Tracking System, green), the **TPC** (Time Projection Chamber, blue) and **TOF** (Time Of Flight detector, orange). All of these are located in the central barrel, covering the full azimuthal angle around the interaction point. Additional information is provided by the T0 detectors and the V0 detectors, which are located along the beam pipe. While with the T0- detectors the start time of the collision can be measured, the V0 detectors are used for the minimum bias trigger [11].

3.1 Inner Tracking System (ITS)

The ITS is the innermost detector in the central barrel, closest to the interaction point. Therefore, its main purpose is the reconstruction of the collision point (*primary vertex*), and the search for the *secondary vertices* resulting from weak decays [12]. It consists of six cylindrical layers located at radial distances from the beam line between 3.9 cm and 43.0 cm. Three different technologies are used as shown in Figure 3.2. The innermost two layers are *Silicon Pixel Detectors* (SPD), followed by two layers of *Silicon Drift Detectors* (SDD)

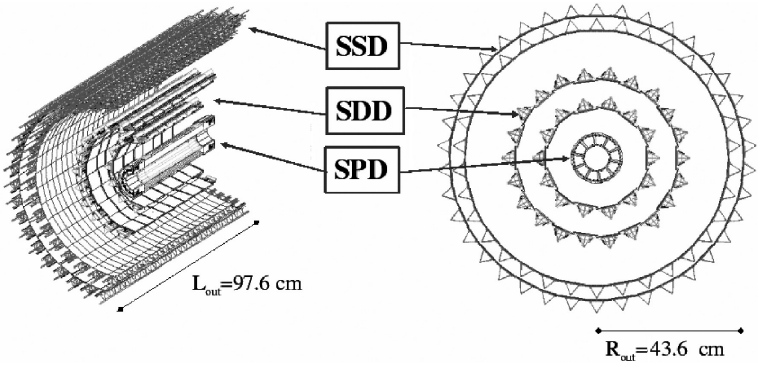

Figure 3.2: Schematic illustration of the ITS with its 6 layers of silicon detectors [13].

layers and the two outer layers of *Silicon Strip Detectors* (SSD) [12].
All layers cover the full azimuth angle and at least a pseudorapidity range of $|\eta| < 0.9$. The dimensions of each layer and corresponding precision are shown in Table 4. Its position resolution ranges from approximately 400μm (few tracklets in the SPD) to about 70μm at higher multiplicity (high number of tracklets) in the z-direction, and ranges from about 500μm to 120μm in the rφ plane [14].

layer	type	acceptance	radius (cm)	length (cm)	spatial precision rφ(μm)	spatial precision z(μm)	cell size (μm^2)
1	pixel	$\|\eta\| < 2.0$	3.9	28.2	12	100	50×425
2		$\|\eta\| < 1.4$	7.6	28.2			
3	drift	$\|\eta\| < 0.9$	15.0	44.4	35	25	150×300
4		$\|\eta\| < 0.9$	23.9	59.4			
5	strip	$\|\eta\| < 1.0$	38.0	86.2	20	830	95×40000
6		$\|\eta\| < 1.0$	43.0	97.8			

Table 4: Dimensions of the ITS detector from the inner layer (1) to the outer layer (6). [11, 13, 15]

The two innermost SPD layers are mainly used to localize the *primary vertices*, as they are the closest to the collision point. These layers are also important for measuring the impact parameters of tracks, such as the distance of closest approach (DCA) to the primary vertex [11]. For tracks reconstructed in the ITS and TPC with a transverse momentum of 0.4 GeV/c the DCA resolution in the plane perpendicular to the beam axis is better than 130 μm [15].

The four outer layers (drift and strip) of the ITS provide space points for reconstructing particle trajectories and the specific ionization energy loss of the particles (dE/dx) in the detector material. The two outermost layers (SDD) are crucial for the matching of the reconstructed tracks in the TPC and the tracklets in the ITS.

3.2 Time Projection Chamber (TPC)

Surrounding the ITS is the Time Projection Chamber (TPC). It is used for track finding and particle identification. Figure 3.3 shows a schematic illustration of the TPC barrel. The

cylindrical chamber of the TPC is located at radii from 80 to 280 cm in the central barrel, covering the full azimuthal angle in a pseudorapidity range of $|\eta| < 0.9$. The volume of around 90 m^3 is filled with a gas mixture of $Ne - CO_2 - N_2$ in a ratio 90-10-5 [11]. The TPC field cage is divided in the middle by a high-voltage electrode (100 kV), creating a homogeneous electrical field towards the end plates of the cylinder [16].

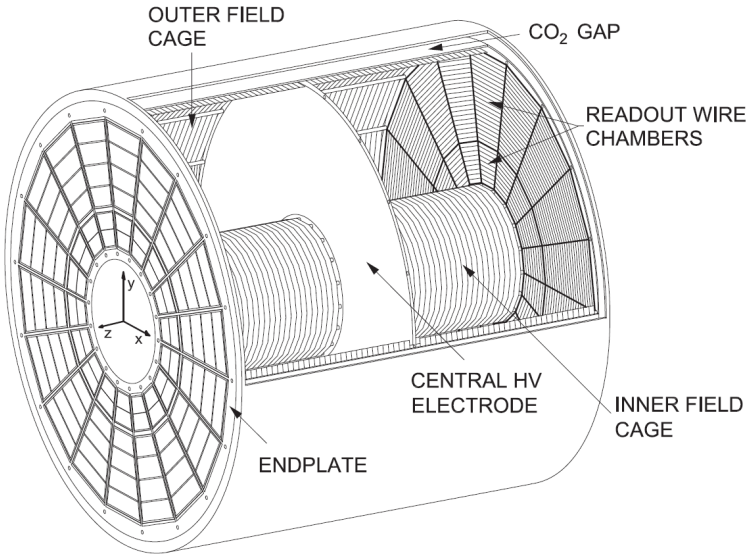

Figure 3.3: Schematic illustration of the TPC [17].

For the readout, multiwire proportional chambers (MWPC) are installed at the end plates. Both end plates are segmented into 18 sectors, each sector consisting of inner and outer readout chambers with active areas ranging from 84 to 132 cm and from 134 to 246 cm in the radial direction. A sector has 159 pad rows (pads in radial direction). To take the topology of the particle spectra and density into account, three different pad sizes are used: 63 rows of smaller pads in the inner readout chambers ($4 \times 7.5\text{mm}^2$), and two sets of pad sizes in the outer readout chambers, with 64 rows of midsize pads ($6 \times 10\text{mm}^2$) and 32 rows with the pad size of $6 \times 15\text{mm}^2$. [17]

A schematic illustration of the function of a multiwire proportional chamber is shown in Figure 3.4. Here the black line represents the track of a charged particle traversing the TPC and hereby ionizing the gas inside the TPC leaving ion-electron pairs behind. Due to the electric field within the TPC, the released electrons drift towards the readout chambers.

In the MWPC, electrons are amplified by a factor of 2×10^4 between the cathode and anode plane. The ions of the secondary ion-electron pairs induce a signal on the readout pads through the method of image charge, forming so-called clusters. The electric signal is proportional to the specific energy loss $\mathrm{d}E/\mathrm{d}x$ of the charged particle. As the track is projected on the pad plane ($\mathrm{r}\varphi$), additional information is needed for the z-coordinate. Given that the measurement is time-dependent and the drift velocity of the electrons within the gas is known, the z-coordinate can be reconstructed. This results in the creation of three-dimensional space points in the TPC volume, which are then reconstructed into tracks using complex track-finding algorithms. The reconstructed track can be characterized by the χ^2-value of the parametrization of the space points, providing a measure of the track's quality. The track reconstruction in the TPC is performed over a larger p_T range, ranging

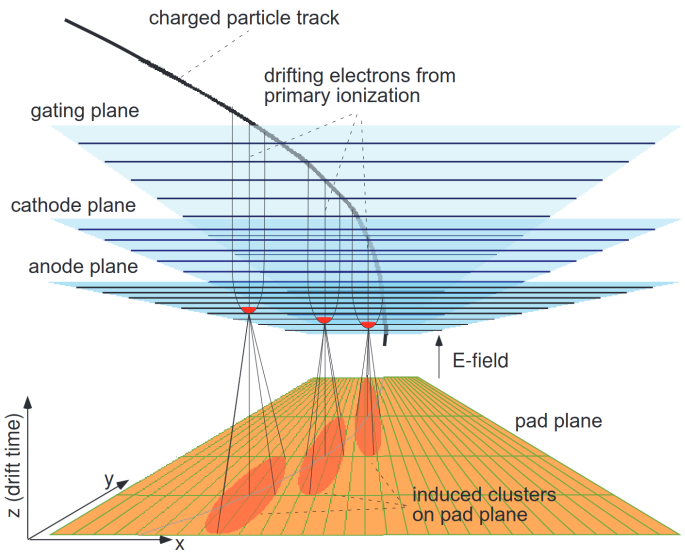

Figure 3.4: Schematic illustration of a multiwire proportional chamber used for track reconstruction [18].

from about 0.1 GeV/c up to 100 GeV/c with a good momentum resolution particularly when the tracks are matched to the ITS tracklets.

In Figure 3.5, the energy deposit per unit length (keV/cm) of charged particles in the TPC as a function of momentum is shown in pp collisions at $\sqrt{s} = 13$ TeV. The specific energy loss ($\mathrm{d}E/\mathrm{d}x$) of charged particles passing through matter can be described by the Bethe-Bloch formula, with the mean specific energy loss as [17]:

$$\left\langle \frac{dE}{dx} \right\rangle = \frac{4\pi N e^4}{mc^2} \left(\frac{Z}{A}\right) \left(\frac{1}{\beta^2}\right) \left(\log\left(\frac{2mc^2}{I^2} \beta^2\gamma^2 \right) - \beta^2 - \frac{\delta(\beta)}{2} \right), \tag{3.1}$$

where N is the number density of electrons in the traversed matter, e is the elementary charge, mc^2 is the rest energy of the electron, Z and A are the atomic number and mass of the traversing particle, β is the velocity, γ is the Lorentz factor, and I is the mean excitation energy of the atom in the gas.

The energy loss is dependent on the charge and the speed of the particles. The Bethe-Bloch formula refers only to energy loss due to ionization, not to losses due to Bremsstrahlung. As Bremsstrahlung is significant for particles of small masses, the parametrization for electrons must be modified. This modified Bethe-Bloch formula, depending on β and γ, can be parameterized as proposed by the ALEPH experiment and is defined as: [17]

$$f(\beta,\gamma) = \frac{P_1}{\beta^{P_4}} \left(P_2 - \beta^{P_4} - \log\left(P_3 + \frac{1}{(\beta\gamma)^{P_5}} \right) \right), \tag{3.2}$$

with fit parameters P_{1-5}. In Figure 3.5 the black lines on top of the $\mathrm{d}E/\mathrm{d}x$ bands show the modified Bethe-Bloch parameterizations for pions, electrons, kaons, protons as well as deuterons. The particle identification is limited in the overlap regions of the $\mathrm{d}E/\mathrm{d}x$ bands, where the particles can't be distinguished from each other. Additional information from other detectors is needed to identify the electrons in these overlapping regions.

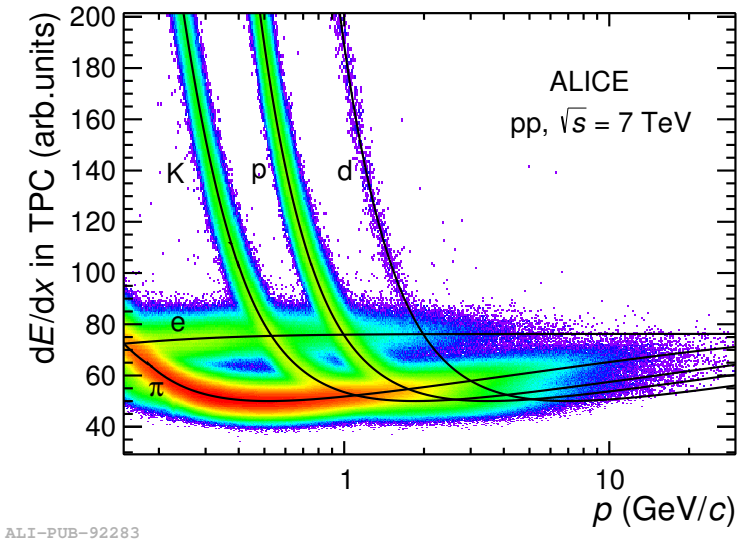

Figure 3.5: Measured energy loss ($\mathrm{d}E/\mathrm{d}x$) in arbitrary units of charged particles in the TPC produced in pp collisions at $\sqrt{s} = 7$ TeV [19].

3.3 Time of Flight (TOF)

The additional information for the PID in the intermediate momentum range can be provided by the Time of Flight (TOF) detector. It is the second detector after the TPC located at the radial position of 370 < r < 399 cm, covering the full azimuthal angle and the pseudorapidity range of $|\eta| < 0.9$. The TOF detector has a modular structure with 18 sectors in the φ direction and 5 segments in the z direction. [11]

Using multi-gap resistive plate chambers (MRPC) technology for readout, the TOF detector is a gas detector just like the TPC. As the name suggests, the TOF measures the time of flight of the particle by measuring with high precision its passing time (t_{TOF}). The start time t_0 is provided by the T0 detectors. If the start time is not available from the T0 detectors the TOF has its own algorithm to estimate the start time from the measured signal of all particles produced in the collision. The particle identification, based on a time difference measurement together with the track length (L) information, is then used to determine the velocity and the invariant mass with [11]:

$$m = p \cdot \frac{t_{TOF} - t_0}{L} \cdot \sqrt{1 - \frac{L^2}{c^2(t_{TOF} - t_0)^2}}. \tag{3.3}$$

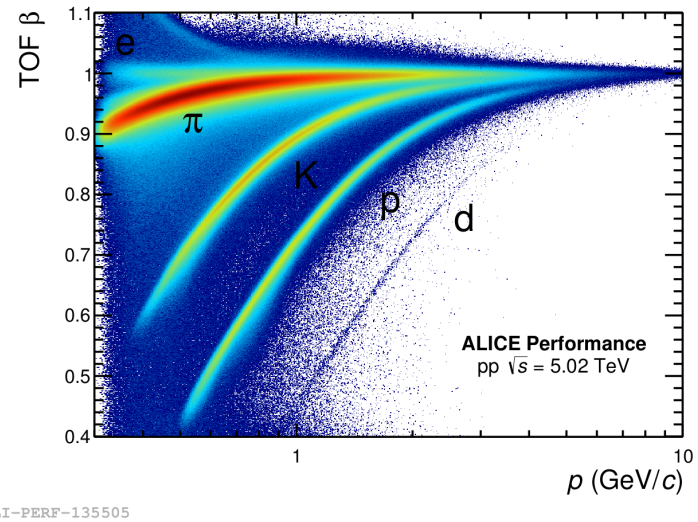

Figure 3.6: Relativistic velocities (β) of the particles in dependence of the momentum for charged particles passing through the TOF detector in pp collisions at $\sqrt{s} = 5.02$ TeV [20].

The particle velocity as a function of momentum can then be seen in Figure 3.6. Comparing the overlapping regions of the particle from Figure 3.6 with those in Figure 3.5, it can be seen that the overlapping and therefore indistinguishable regions are in different momentum ranges for TPC and TOF. Electrons and kaons are easily distinguished up to about 2.5 GeV/c, and electrons and protons up to about 4 GeV/c. With the additional information provided by the TOF it is now possible to distinguish these particles/tracks so that the overlapping areas in the TPC are rejected for PID purposes and the information from the TOF can be used here [11].

3.4 V0 detectors

The V0 detector consists of two segmented scintillator detectors, V0A and V0C, located at asymmetric distances on either side to the interaction point along the beam pipe. Covering pseudorapidity ranges $2.8 < \eta < 5.1$ (V0A) and $-3.7 < \eta < -1.7$ (V0C), the V0A is located 330 cm from the interaction point opposite the muon spectrometer, while the V0C is 90 cm from the interaction point. [21] The purpose of the V0 detectors is to operate as fast triggers for the central barrel detectors, to provide a minimum-bias trigger (and further centrality triggers for Pb–Pb collisions), to characterize events by multiplicity and centrality, as well as to measure the luminosity(L) in pp collisions. Luminosity relates to the cross-section of events σ and the event rate R, with $R = \mathrm{L}\sigma$.

3.5 L3 magnet

The central barrel is encased by the L3 magnet (Figure 3.1, shown in red). The L3 magnet generates a solenoid field of 0.5 T with field lines parallel to the beam pipe and the electric field generated in the TPC. Depending on the charge and momentum of the particle, its track is bent accordingly (momentum) to the corresponding direction (charge) in the plane transverse to the magnetic field. Due to the magnetic field, charged particles must have a momentum $p_{\mathrm{T}} > 300$ MeV/c to reach the TOF detector, otherwise the curvature of the particle track will be too strong.

4 Data set and electron selection

This section describes in detail the data set and the selection criteria for the electron candidates used for this analysis.

4.1 Data set

The presented analysis is based on pp collision data from 2017, measured at a center-of-mass energy of $\sqrt{s} = 5.02$ TeV and a magnetic field of 0.5 T, collected by the ALICE experiment. This analysis extends the published paper on dielectron production in pp collisions at $\sqrt{s} = 5.02$ TeV [22]. The data set was collected in several runs during the so-called `LHC17p` data-taking period. During the data-taking period, a run is defined as a period in which the detector performance is expected to be constant and the same detector and trigger setup has been used. Each run consists of different trigger clusters of recorded events corresponding to different detector busy times. The relevant trigger clusters for this analysis are the `CENT` and `FAST` trigger clusters. The `CENT` trigger condition refers to the data where all detectors are available in the central barrel. The `FAST` trigger condition doesn't require the availability of the SDD layers of the ITS. To be able to combine these two data samples, the (`CENT`) sample was reconstructed without the SDD layers (`CENT_woSDD`). This gives the same conditions as the `FAST` data sample. As the data set provides information from only 4 ITS layers instead of 6, the ITS is not used for electron identification as the ITS PID is performed with the four outer layers of the ITS.

The analysis is performed on the first reconstruction pass that was provided centrally. Although a second reconstruction pass with minor improvements is available, this analysis remained on the first reconstruction pass to be consistent with the previously mentioned publication of the dielectron production paper. In the `LHC17p`(pass 1) data set a total of 1178M reconstructed events were recorded, 781M reconstructed events with the `FAST` trigger cluster and 396M reconstructed events with the `CENT_woSDD` trigger cluster. Events were collected using a minimum-bias trigger, which requires a time coincident signal in both V0 detectors (V0AND) to start the data collection.

The data format of this analysis are so-called Analysis Object Data(AOD) files, which is a pre-filtered data format of the fully reconstructed data of so-called Event Summary Data (ESD). While ESDs contain more information, AODs are providing only the necessary information for this analysis and with that the usage of AODs results in faster processing times.

The Monte Carlo (MC) productions that are used for this analysis are so-called 'anchored' MC productions. 'Anchored' MC productions reflect the detector conditions during the different runs. The used MC productions are anchored to the runs of the `LHC17p` data-taking period that can be found in the appendix A.1. PYTHIA8 [23] is used as MC generator, while the interaction of the particles with the detector material is simulated with the transport code GEANT 3 [24]. To gain sufficient statistics several MC productions are used.

The used productions are each the `fast` and `cent_woSDD` versions of the following productions:

- `LHC17l3b`: a general-purpose MC production anchored to LHC17p/q,
- `LHC18j2`: an extension of the general-purpose MC productions anchored to LHC17p/q and
- `LHC19h8`: MC production for the LHC17p/q data-taking period with heavy-flavour enhanced dielectron contributions with extra statistics.

For the data analysis, the `LHC17p` data-taking period is used to obtain the central values of the measurement as well as an estimation of the systematic uncertainties from an insufficient reproduction of the detector response in the MC simulations. Efficiency and acceptance corrections as well as the raw signal shape of the ω peak were estimated using the anchored MC simulations (`LHC17l3b` & `LHC18j2`). The estimations for the efficiency maps to create the cocktail templates were done with the heavy-flavour enhanced MC simulation (`LHC19h8`).

4.2 Event Selection

For the event selection, each event is required to have a primary vertex reconstructed from tracklets reconstructed in the SPD layers of the ITS. The reconstructed primary vertex of the event is required to be within 10 cm of the nominal interaction point along the beam (z) axis to assure an uniform detector acceptance and efficiency. In addition, there needs to be at least one contributing tracklet to the vertex.

4.3 Track Selection

The following track selection is about selecting primary electrons and discarding secondary electrons. Primary tracks refer to tracks originating from the hadronic collision, while secondary tracks refer to tracks originating from photon conversions in the detector material. The first selection applied to all tracks is based on a standard selection of global tracks with loose DCA cuts. For the selection of reconstructed tracks, there are different variables of interest [25]:

- The *number of clusters* refers to the number of signals on pads or hits attached to the reconstructed tracks. The maximum number of clusters for the track reconstruction of particles passing through the detector is 159 clusters for the TPC and 4 clusters (6 minus the 2 SDD layers) for the ITS.
- The *number of shared clusters* is the number of clusters that the reconstructed track shares with other reconstructed tracks.
- The *number of crossed rows* of a reconstructed track gives the number of pad rows on which the track was reconstructed. If a cluster is missing in a pad row along the reconstructed track, while the neighboring pad rows have a cluster signal for that track, this missing pad row is also counted to the number of crossed rows.
- The *number of findable clusters* represents the number of clusters that could have been found along the path of the reconstructed track. This number can be greater than the number of clusters if the track is projected onto more than one sector.

The track selections used for primary electron selection are listed in Table 5. For the electron/positron acceptance, $p_{\mathrm{T}} > 0.2$ GeV/c and $|\eta| < 0.8$ are required. For track reconstruc-

tion in the ITS, at least two clusters in the 4 layers (SPD, SSD) are required with a hit in the first ITS layer. Tracks sharing ITS clusters are not allowed, in order to reduce the number of tracks originating from photon conversion. For the tracks in the TPC, the number of clusters has to be greater than 80 and the number of rows greater than 100. Along the track, the number of crossed rows to findable clusters has to be above 70%. The fraction of shared TPC clusters has to be below 40%. In addition, the tracks are required to have a successful refit in the ITS and TPC.

Track observable	Requirement
Fiducial selection	
p_{T}	> 0.2 GeV/c
$\lvert\eta\rvert$	< 0.8
ITS requirements	
ITS refit	required
Number of ITS clusters	≥ 2
χ^2 per ITS cluster	< 6.5
No ITS shared cluster	required
Hit in first layer	required
DCA_{xy}	< 1 cm
DCA_z	< 3 cm
TPC requirements	
TPC refit	required
Number of TPC clusters	> 80
Number of crossed rows	> 100
Ratio of crossed rows / findable clusters	≥ 0.7
Fraction of shared TPC clusters	≤ 0.4
χ^2 per TPC cluster	< 3.0

Table 5: Summary of global track cuts used in this analysis.

4.4 Electron identification

Electron identification in this analysis is based on the measurement of the specific energy loss $\mathrm{d}E/\mathrm{d}x$ in the TPC and the time of flight measurement in the TOF. The selection and rejection of a particle is always performed in the $n\sigma_i^{det}$ where i is the particle species and det is the detector (TPC or TOF). The calculation is done by subtracting the expected signal ($\langle S_{det}^i \rangle$) for the particle of type i from the measured signal (S_{det}) in the detector and normalizing it to the expected signal resolution in units of its standard deviation (σ_{det}) at the given momentum. Thus, the variable $n\sigma_i^{det}$ indicates how well the measured signal for electron identification matches the signal expected from theoretical predictions. $n\sigma_i^{det}$ is defined as:

$$n\sigma_i^{det} = \frac{S_{det} - \langle S_{det}^i \rangle}{\sigma_{det}}, \tag{4.1}$$

The information from TOF and TPC are combined to select electrons and reject pions, kaons and protons as follows. A sample of electrons is selected within $\left|n_{\sigma_e}^{TPC}\right| < 3$ in the TPC. Due to hadron contamination in the overlap areas of the hadron bands with the electron bands (as in Figure 3.5), the following rejections are applied in the TPC PID:($n_{\sigma_\pi}^{TPC} < 4$), ($-2.5 < n_{\sigma_p}^{TPC} < 3.5$) and ($\left|n_{\sigma_K}^{TPC}\right| < 3$).
In the next step, the TOF information is used to fill the holes from the kaon and proton rejection in the TPC. This is done by selecting the TOF PID signal within $\left|n_{\sigma_e}^{TOF}\right| < 2$ and the TPC PID selection of electrons and rejection of pion as before. Another way of describing this procedure is that a clean sample is selected using only the TPC information by rejecting pions, kaons and protons. A complimentary sample is selected by selecting electrons as well as rejection pions in the TPC, and then rejecting kaons and protons in the TOF. In the latter sample only tracks with an associated TOF signal are allowed. The criteria for both are summarised in Table 6.

Particle	Value
TPC sample	
Electron selection TPC	$\left\|n_{\sigma_e}^{TPC}\right\| < 3$
Pion rejection TPC	$n_{\sigma_\pi}^{TPC} < 4$
Kaon rejection TPC	$-2.5 < n_{\sigma_p}^{TPC} < 3.5$
Proton rejection TPC	$\left\|n_{\sigma_K}^{TPC}\right\| < 3$
TOF sample	
Electron selection TOF	$\left\|n_{\sigma_e}^{TOF}\right\| < 2$
Electron selection TPC	$\left\|n_{\sigma_e}^{TPC}\right\| < 3$
Pion rejection TPC	$n_{\sigma_\pi}^{TPC} < 4$

Table 6: Summary of the particle identification cuts used in this analysis.

5 Analysis

The following section covers the procedure on how to extract the ω meson signal via the dielectron decay channel. The estimation of the background underneath the ω signal is addressed and four methods are presented. Furthermore, the extracted ω signal is correct for acceptance and efficiency losses, as well as other correction factors. Finally, the estimation of related systematic uncertainties is reported.

To extract the transverse momentum spectrum, the analysis is carried out in several p_{T} intervals, as displayed in Table 7.

p_{T} bins	1.	2.	3.	4.	5.	6.	7.
(GeV/c)	$0.0-0.3$	$0.3-0.6$	$0.6-1.0$	$1.0-1.5$	$1.5-2.2$	$2.2-3.2$	$3.2-6.0$

Table 7: p_{T} intervals used for this analysis.

5.1 Signal extraction

The reconstruction of the ω signal via the dielectron decay channel presents several challenges. There is, for example, the very small branching ratio of $\omega \rightarrow \mathrm{e}^+\mathrm{e}^-$ with 0.0074%. Therefore, the probability is small that a ω is produced and decays via the dielectron channel, where both daughters are detected and identified by the detectors. A large number of pp collisions is required for an accurate measurement. However, the fact that only two daughters need to be combined and not more is an advantage for this analysis, which allows for a p_{T} reach down to $p_{\mathrm{T}} = 0$.

The first step in the reconstruction of the ω meson is to pair the daughters. Since it is not possible to say which electron and which positron originate from the ω, a combinatorial approach is taken. All selected electron and positron candidates of the same event are paired with each other into an unlike-sign (ULS) ($\mathrm{e}^+\mathrm{e}^-$) spectrum. This ULS spectrum is composed of different information. It contains not only the pairs of the signal: $\omega \rightarrow \mathrm{e}^+\mathrm{e}^-$, but also background contributions.
In the following subsections different methods to estimate these background contributions are probed. But first, the signal shape of the ω that is to be extracted will be examined.

5.1.1 Signal shape

The ω emerges as a peak in the invariant mass spectrum of the electron and positron pairs around its pole mass of 782 MeV/c^2 [3] with a Gaussian shape. This natural line shape changes due to several effects in the ULS spectrum. One effect is the detector resolution which leads to a broadening of the peak width. Since the ω is reconstructed with light charged particles (electrons/positrons) Bremsstrahlung effects must be taken into account in this analysis. Electrons/positrons lose energy via interactions with the detector material. Since this energy loss is not taken into account in the reconstruction of their initial momentum, their reconstructed p_{T} tends to be smaller than their true p_{T}. This creates an additional tail in the ω signal, by smearing the distribution of the signal shape to masses lower than the pole mass.
In order to constrain the functional shape and study the reconstructed ω for this analysis, a full MC simulation using the ALICE detector with the corresponding material budget is utilized. Figure 5.1 shows the ω signal from a full MC simulation after applying the selection

criteria to the reconstructed tracks over the full integrated p_{T} range. In order to increase the statistical precision, electrons are selected using the MC information. No PID selections are made. This is because PID selections only reduce the data sample, but don't affect the shape, which is the essential part to be studied here. In Figure A.2 the ω signal is shown for all p_{T} intervals used for the analysis. However, due to the limited statistics of the MC sample the higher p_{T} intervals $(2.2 - 3.2)\mathrm{GeV}/c$ and $(3.2 - 6.0)\mathrm{GeV}/c$ are combined.

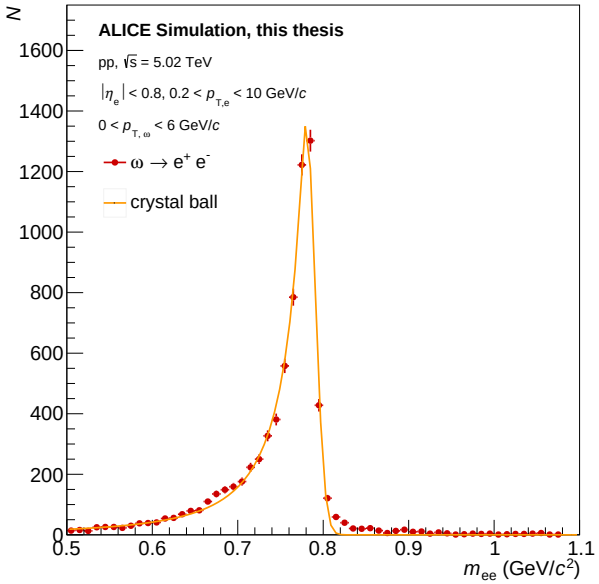

Figure 5.1: Reconstructed ω signal from MC simulations after fiducial and track selections described by a CB function for an integrated p_{T} range 0 - 6 GeV/c.

In Figures 5.1 and A.2 the reconstructed MC signal is shown as red markers, with a parametrization of the signal shape as an orange line. The function used to parametrize the ω signal describes the peak and the tail structure of the signal. The function is defined as

$$f(x;\alpha,N,\bar{x},\sigma) = const \cdot \begin{cases} \exp\left(-\frac{(x-\bar{x})^2}{2\sigma^2}\right), & \text{if } \frac{x-\bar{x}}{\sigma} > -\alpha \\ A \cdot \left(B - \frac{x-\bar{x}}{\sigma}\right)^{-N}, & \text{if } \frac{x-\bar{x}}{\sigma} \leq -\alpha \end{cases} \tag{5.1}$$

with:

$$\begin{aligned} A &= \left(\frac{N}{|\alpha|}\right)^N \cdot \exp\left(-\frac{|\alpha|^2}{2}\right) \\ B &= \frac{N}{|\alpha|} - |\alpha| \\ const &= \frac{1}{\sigma(C+D)} \\ C &= \frac{N}{|\alpha|} \cdot \frac{1}{N-1} \cdot \exp\left(-\frac{|\alpha|^2}{2}\right) \\ D &= \sqrt{\frac{\pi}{2}}\left(1 + \mathrm{erf}\left(\frac{|\alpha|}{\sqrt{2}}\right)\right). \end{aligned}$$

Here $\bar{x}$ is the mean and σ is the width of the Gaussian. A power law describes the Bremsstrahlungs tail with parameters *const* and N. α is a transition parameter between the Gaussian and power law parts. This function $f(x)$ is also known as the crystal ball (CB) function [26]. The CB function describes the general characteristics of the signal shape in both the p_{T} integrated and the differential parameterizations. The values of the four parameters ($\bar{x}$, σ, α, and N) of the CB function after a fit to the data are shown in Fig. 5.2 for the different p_{T}-intervals used in the analysis. In addition to the results in the individual p_{T} intervals (open markers), the p_{T} integrated parameters are shown as full markers. The integrated p_{T} parameters can be compared with a constant (`pol0`) parameterization of the individual p_{T} intervals. Within the uncertainties, both give the same values for all four parameters. As there is no strong p_{T} dependence of the CB parameters, and to minimize the effects of statistical fluctuations in the signal extraction, the analysis is continued using the parameters extracted from the parameterization of the p_{T} integrated ω signal ($0-6$ GeV/c).

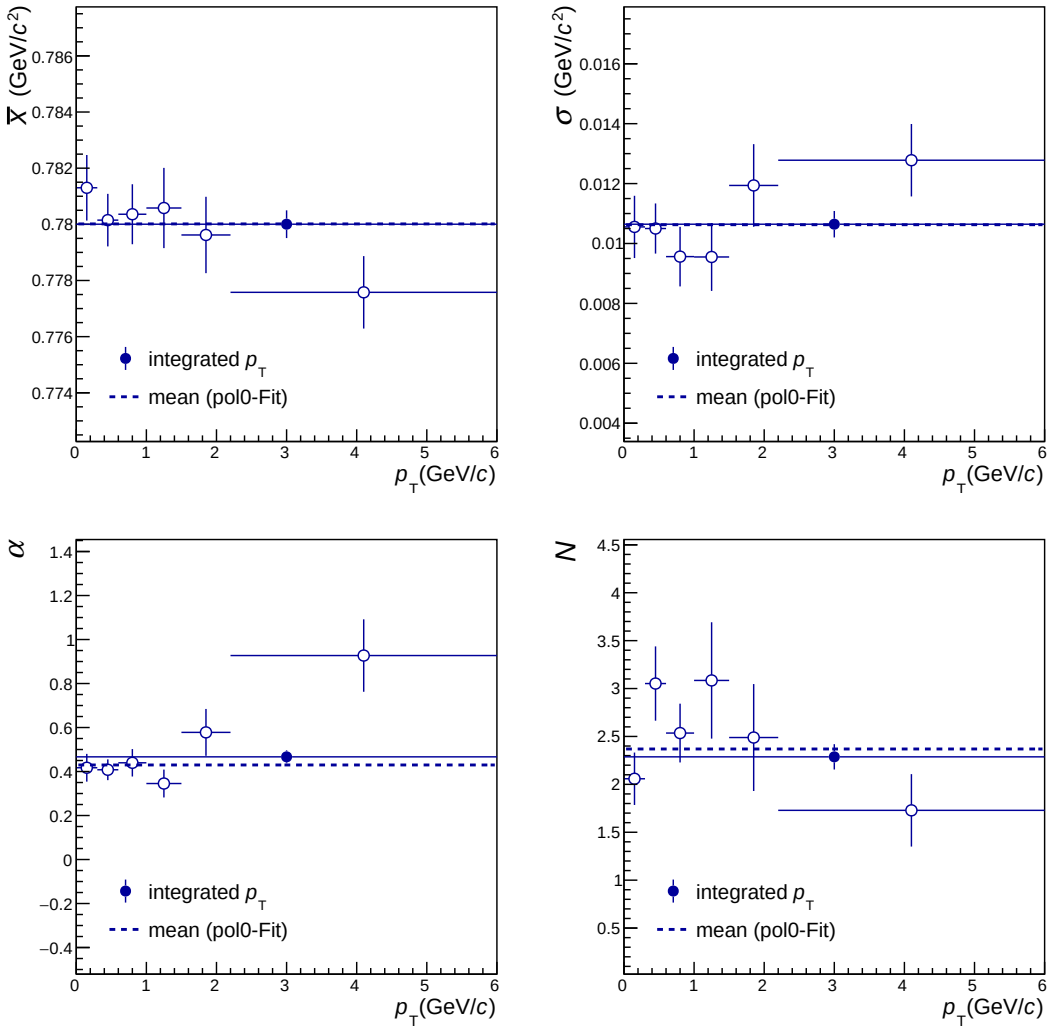

Figure 5.2: Parameters of the CB function extracted from Figure A.2 as a function of p_{T} (open markers), with the corresponding mean value as a dashed line. They are compared to the CB parameters obtained for the p_{T}-integrated ($0-6$ GeV/c) invariant mass spectrum of ω (full markers).

5.1.2 Background estimation

Once the signal shape is parameterized, the background has to be estimated, in order to extract the ω signal. Four different methods are used to estimate the background. It is distinguished between two main ideas for these methods. The first method follows a one-step estimation of the background, the other three methods estimate the background in two steps. The two-step methods differ in their approaches in the second step.

Background estimation via ULS spectrum - Method 1

For the first main idea of the background estimation, minimal input is required. This one-step approach estimates the background directly on the ULS spectrum. The only assumption is that the underlying background below the ω peak is smooth with respect to the background outside the signal region. The estimation is done by parameterizing the ULS spectrum with a polynomial function (`pol2`) part for the background and the crystal ball function for the expected signal shape. The initial parameters for the polynomial function are adopted from a sideband parameterization (a `pol2` parameterization outside the peak region) to stabilize the finding of local minima. The parametrization range throughout the analysis is over the m_{ee} range of $(0.6 - 0.9)$ GeV/c^2.
In the following the background estimation steps are shown only for the $(0.3 < p_{\mathrm{T}} < 0.6)$ GeV/c interval. The result for the remaining p_{T} intervals can be found in the appendix A.3.

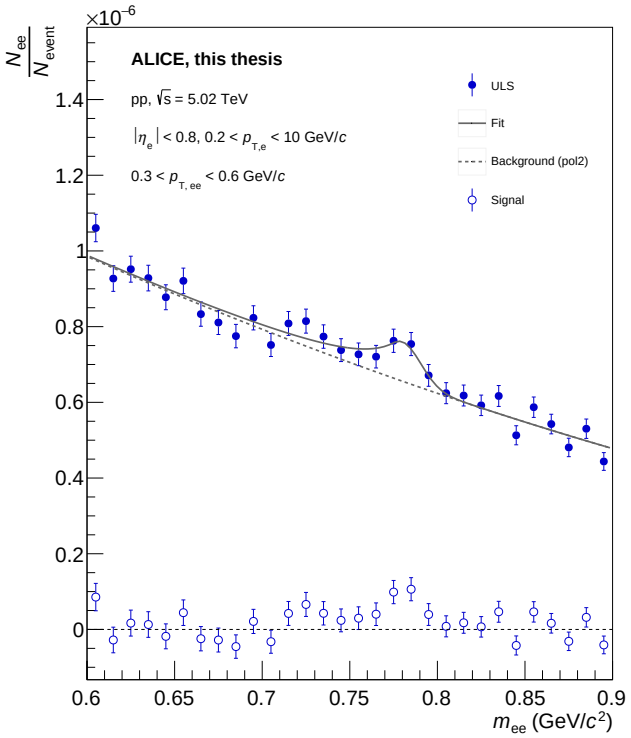

Figure 5.3: ULS - method for the $(0.3 < p_{\mathrm{T}} < 0.6)$ GeV/c interval: the solid gray line is the combined (background+signal) parameterization to the ULS, the dashed line (background) is then subtracted from the ULS resulting in the signal (blue open markers).

In Figure 5.3, the ULS spectrum (blue, full markers) is parameterized with a combined function (gray, solid line) of a second-order polynomial for the background and the parameterized crystal ball. As noted above, the only variable parameter is the amount of yield, while the shape of the signal (four of the five CB parameters) is fixed to the MC signal (see section 5.1.1). This is carried out for each transverse momentum interval independently. The ULS spectrum is normalized to the number of events ($N_{\text{trigger}} = 775\text{M}$) and corrected for the vertex reconstruction efficiency of 96% for pp collisions [22]. In order to extract the signal (blue, open markers), the background (gray, dashed line) is subtracted from the ULS spectrum.

Background estimation via LS spectrum - Method 2

For the second main idea of how to estimate the background, more information than just the ULS spectrum is used. This is due to the fact that in addition to the signal pairs, the ULS also contains pairs from other decays, which in other dielectron analyses are considered as signals, but here these signal pairs contribute to the background below the ω signal. Furthermore, combinatorial pairs are present, which can be correlated or uncorrelated. Correlated pairs originate from electron-positron pairs in fragmenting jets or so-called cross pairs. *Cross pairs* are more dominant in the low invariant mass regime, for example as a result of a Dalitz decay (decay of a neutral pseudoscalar meson → dielectron + [photon/vector meson]) with a photon conversion. This then results in two correlated dielectron pairs from the same decay process. On the other hand *jet fragmentation* predominates at higher invariant masses where multiple dielectron pairs are decay objects from Dalitz decays of pions within a jet. [27]

Thus, in the first method presented, the combinatorial and physical background are estimated in one step. In the remaining methods, the combinatorial and physical background are estimated separately in two steps.

Method 2: First step - Estimation of the combinatorial background For the combinatorial background, the contributions, under charge symmetry, have the same shape for e^+e^-, e^+e^+ and e^-e^- pairs. So the selected electron and positron candidates of the same event are paired in an unlike-sign (e^+e^-) as well as in two like-sign (LS_{--}: e^-e^-, LS_{++}: e^+e^+) spectra, as is done in other dielectron analyses [28, 22]. These two like-sign spectra are then summed to form a LS spectrum ($LS_{\pm\pm}$).
Here, due to the limited statistics, a hybrid calculation is used to minimize the number of empty bins. Primarily, both spectra are added geometrically, but if one spectrum has an empty bin, the arithmetic sum is used.

$$LS_{\pm\pm} = \begin{cases} 2 \cdot R_{acc} \cdot \sqrt{LS_{--} \cdot LS_{++}}, & \text{for } LS_{--} > 0 \text{ and } LS_{++} > 0 \\ LS_{--} + LS_{++}, & \text{for } LS_{--} = 0 \text{ or } LS_{++} = 0 \end{cases} \tag{5.2}$$

with R_{acc} as the correction factor to account for the detector acceptance differences for ULS and LS pairs and is calculated from the ULS (M_{+-}) and LS (M_{++}, M_{--}) spectra of mixed events, as follows [29]:

$$R_{acc} = \frac{M_{+-}}{2 \cdot \sqrt{M_{++} \cdot M_{--}}} \ . \tag{5.3}$$

R_{acc} has deviations from 1 of less than 1% for the lower p_{T} intervals and less than 2% for the last p_{T} interval of this analysis (see section A.3), so the statistical uncertainties are dominant and R_{acc} is negligible. With the additional information provided by the LS spectrum to

estimate the combinatorial part of the background under the ω signal, this approach is closer to the approach used in previous dielectron analyses [28, 22] than of method 1. Contrary to other dielectron analyses, the LS spectrum in this analysis is parametrized by a second-order polynomial function (`pol2`). Whereas in other dielectron analyses the LS spectrum is subtracted in two dimensions (2D: p_{T} and m_{ee}), here the parametrization of the LS spectrum is a valid approach because it is done in small p_{T} and m_{ee} intervals, and by doing so the `pol2`-function minimizes the statistical fluctuations of the LS spectrum.

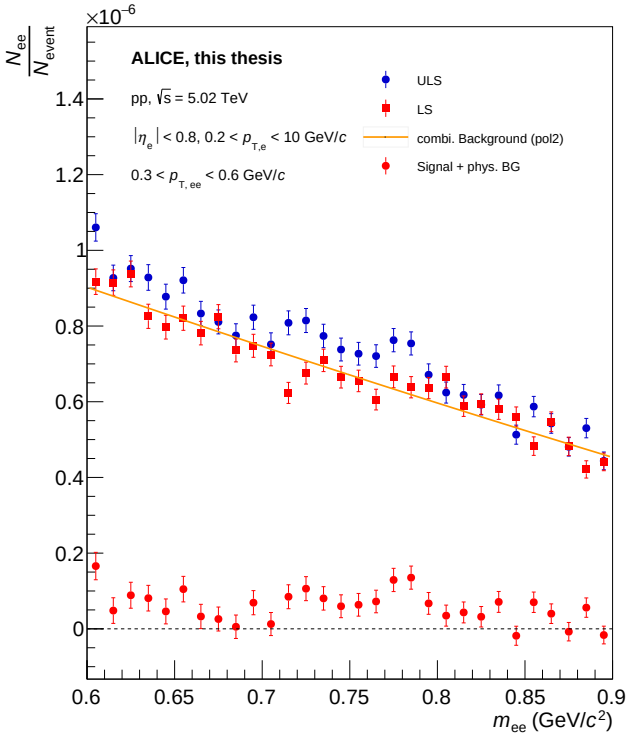

Figure 5.4: First step LS - method for the $(0.3 < p_{\mathrm{T}} < 0.6)$ GeV/c interval: the solid orange line is the combinatorial background parametrization to the LS (red, full markers), which is then subtracted from the ULS resulting in the physical background + signal (red, open markers).

This first step of the background estimation, using the LS spectrum, is shown in Figure 5.4. Here the `pol2` function is shown as an orange line, parametrizing the LS spectrum (red, square markers). This function is then subtracted from the ULS spectrum (blue, round markers), resulting in the red, round spectrum, which still contains the ”physical” background component next to the ω signal.

Method 2: Second step - Estimation of the "physical" background To further subtract the physical background a second step is required. Three different approaches are used to describe the remaining background:

(a) A fully normalized cocktail template of known hadronic sources, based on independent measurements, without the $\omega \rightarrow e^+e^-$ contribution. The normalization is based on independent hadron measurements only.

(b) Using the cocktail template as in method 2(a), except that the normalization is based on a parameterization to the data points.

(c) An ad hoc parameterization with a first order polynomial is used to describe the physical background.

Cocktail template Two of the methods for the physical background estimation uses cocktail templates. The cocktail templates are created based on information from the *hadronic cocktail*. The *hadronic cocktail* takes as input results from experimental analysis and theory to simulate the dielectron contributions from known hadronic sources in the dielectron spectrum. These include contributions from meson decays (pseudoscalar mesons as well as vector mesons) and correlated semileptonic decays of heavy-flavour hadrons.

For this analysis, the same hadronic cocktail is used as in the dielectron production paper [22], which is calculated upon expected hadronic sources in a data-driven fast simulation. Here, several approaches are used to estimate the dielectron yield in m_{ee} and p_T for the different sources. For example, the ρ (mass) line shape is taken from the published ρ line shape of the NA60 collaboration in pA collisions at 400 GeV [30], while the momentum distributions for ρ utilize the $\rho/\pi^{\pm}$ ratio obtained from the Monash 2013 tune of PYTHIA 8. For η, a parametrization of the η/π^0 measured ratio at different energies is taken as input. The η' meson is estimated assuming m_T-scaling. The ϕ meson is obtained from the measured p_T spectrum of the ϕ meson in pp collisions at $\sqrt{s} = 5.02$ TeV with ALICE [31]. The dielectron yield from correlated open-charm ($c\bar{c}$) and open-beauty ($b\bar{b}$) hadron decays is simulated with the leading order (LO) PYTHIA 6 event generator. Both contributions are fitted to the measured dielectron yield as a function of p_T and m_{ee} in the invariant mass ($1.1 < m_{ee} < 2.7$) GeV/c^2 as explained in [22].
To convert the given cocktail, as shown in Figure 5.5, from $d\sigma/dm_{ee}$ to a raw yield, the minimum bias cross section ($\sigma_{MB} = 50.87 \pm 0.04$ mb) [32]) and efficiency effects due to track and electron selection are included based on a full MC simulation. In Figure 5.5 the expected total cocktail sum as a function of m_{ee} is shown as a black dashed line. The $\omega \rightarrow e^+e^-$ peak line is presented by the teal solid line. The "physical" background underneath the signal is described by the expected hadronic cocktail sum with all contributors except the ω signal (shown as the red, solid line). In Figure 5.6 the expected contribution to the raw spectrum of the cocktail sum without the ω signal is shown for the ($0.3 < p_T < 0.6$) GeV/c interval, while the remaining p_T intervals can be found in Figure A.3 in the appendix.

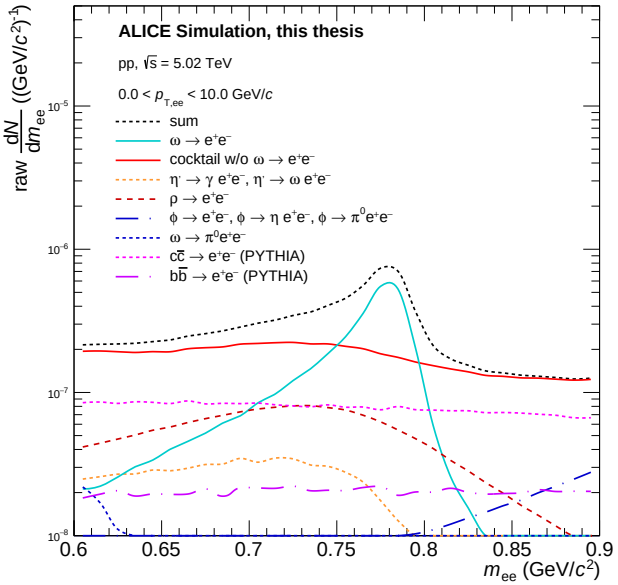

Figure 5.5: Expected hadronic cocktail within the parameterization range of the analysis. Shown is the cocktail sum with all contributions (black, dashed line), $\omega \rightarrow e^+e^-$ (teal, solid line), cocktail sum without the ω signal (red, solid line), as well as other components contributing to the cocktail sum within the parameterization range.

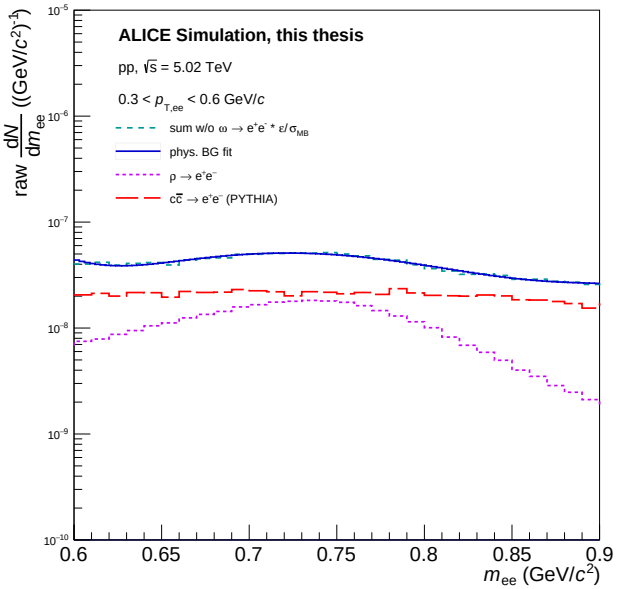

Figure 5.6: Cocktail template for the $(0.3 < p_{\mathrm{T}} < 0.6)$ GeV/c interval using a `pol5` parameterization (blue solid line). The cocktail sum without the ω signal shown in Figure 5.5 is converted from $\mathrm{d}\sigma/\mathrm{d}m_{\mathrm{ee}}$ to a raw yield. Two main contributors to the "physical" background are also shown, $\mathrm{c\bar{c}}$(red line) and ρ (purple line).

Here the cocktail template for the "physical" background (teal, dashed line) is parametrized by a polynomial function (`pol5`) shown as the blue, solid line. The two main contributors

to the "physical" background underneath the ω signal are the wide ρ distribution (purple, dashed line) and the distribution of the charm contributions (red, dashed line). While the heavy flavour contribution is flat, the ρ signal gives the "physical" background a bulged yet smooth trajectory. The `pol5` function adequately describes the distributions in all p_{T} intervals, so these functions are chosen as templates for the "physical" background estimation in methods 2a) and 2b).

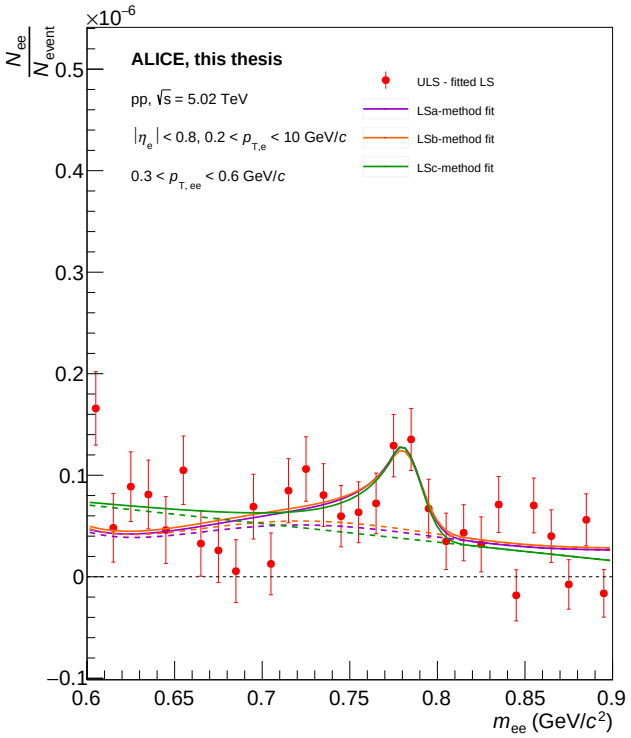

Figure 5.7: Second step of the LS methods shown for the $(0.3 < p_{\mathrm{T}} < 0.6)$ GeV/c interval: the three solid lines are the combined (physical background+signal) parametrization (purple: cocktail template + CB; orange: cocktail template with parameterization + CB; green: constant polynomial+CB) of the subtracted ULS in Figure 5.4. The dashed lines show the physical background, which is still underneath the ω signal.

In Figure 5.4, the invariant mass spectrum after subtraction of the combinatorial background (ULS - fitted LS) is shown as red, round markers for $(0.3 < p_{\mathrm{T}} < 0.6)$ GeV/c. It still contains the contributions of the "physical" background from ρ and charm decays. These are estimated in a second step using the different methods described above. This remaining spectrum is parameterized with a combined parameterization of a CB and a background component. In the case of the LSa method (purple line) - the background component is completely fixed to the cocktail template (`pol5`) discussed in section 5.1.2. The only free variable of this combined parameterization is the amplitude of the ω signal. For the LSb method (orange line) - the cocktail template has a normalization parameter, which is an additional free parameter beside the amplitude of the signal shape. For the third method, LSc method (green line), the "physical" background is estimated using a first-order polynomial parameterization with no further physical input. These three estimated backgrounds, shown as dashed lines, are then subtracted to obtain the ω signal.

ω signal

The ω signals obtained with the four different background estimation methods are shown in Fig. 5.8 for the $(0.3 < p_{\mathrm{T}} < 0.6)$ GeV/c interval. The different colors/markers correspond to the different background estimation methods. The resulting CB parameterizations are shown to guide the eye. The only difference for the signal shape in the CB parameterizations is the absolute normalization since the other parameters are fixed by the parameterization to the MC data and are the same for all p_{T} intervals.

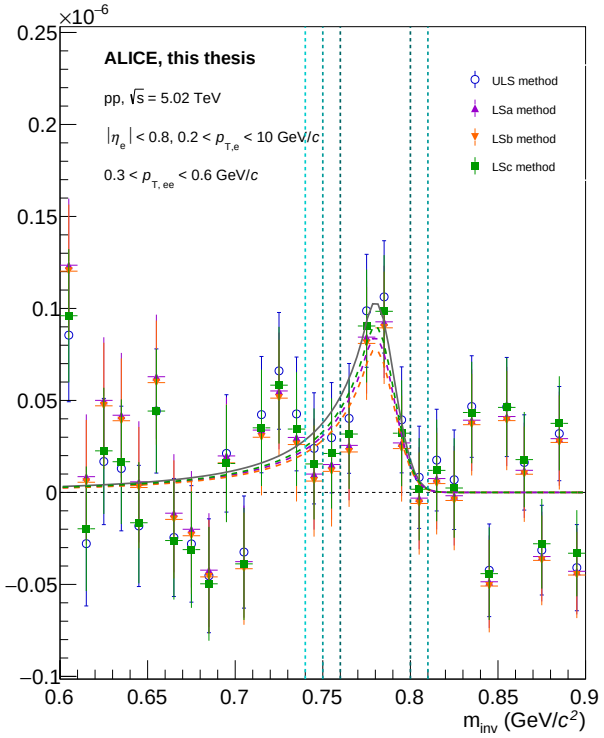

Figure 5.8: Resulting ω signal for the $(0.3 < p_{\mathrm{T}} < 0.6)$ GeV/c interval for all four methods, each with an associated crystal ball function. The bin counting ranges are shown as vertical dashed lines.

Bin counting is performed in designated signal ranges to obtain well-defined statistical uncertainties for the extracted ω yield. This is done due to large statistical fluctuations, especially for the areas outside the signal range.
The ranges in which the signal is counted are based on the Gaussian parameters of the crystal ball parametrization, i.e. the width of the Gaussian peak around its mean. To account for the asymmetric shape (tail) of the signal the lower range can have values of 4, 3, and 2 σ, while only 2 and 3 σ are considered for the upper edge. Since these values of $\bar{x} \pm n\sigma_{true}$ with $n = \{-4, -3, -2, +2, +3\}$, the true $\bar{x} = 0.77995$ GeV/c^2, and the true $\sigma_{true} = 0.01061$ GeV/c^2, are not compatible with the bin edges of the histogram the closest bin edges of the histogram are chosen. The true values as well as the bin edge values used can be seen in table 8. The bin edge values are shown as vertical lines in Figure 5.8.

true	$\bar{x} - 4\sigma_{true}$	$\bar{x} - 3\sigma_{true}$	$\bar{x} - 2\sigma_{true}$	$\bar{x} + 2\sigma_{true}$	$\bar{x} + 3\sigma_{true}$
	0.738 GeV/c^2	0.748 GeV/c^2	0.759 GeV/c^2	0.801 GeV/c^2	0.812 GeV/c^2
bin	0.740 GeV/c^2	0.750 GeV/c^2	0.760 GeV/c^2	0.800 GeV/c^2	0.810 GeV/c^2
	-4σ	-3σ	-2σ	$+2\sigma$	$+3\sigma$

Table 8: Signal ranges for the bin counting of the ω signal. Comparison of the m_{ee} bin edge values to the true values calculated with the CB parameters $\bar{x}$ and σ_{true}.

5.1.3 Yield

After integrating (bin counting) the signal within the ranges discussed above, a correction for the signal outside the range is required. This is done by calculating the fraction of the signal within the range based on the MC signals shown in Figure A.2.

$$Y_{norm} = \frac{Y(A,B)}{\epsilon} \text{ with } \epsilon = \frac{N_{\omega}^{\mathrm{MC}}(A,B)}{N_{\omega}^{\mathrm{MC}}}. \tag{5.4}$$

The fraction ϵ is calculated in each p_{T} interval independently by dividing the number of reconstructed ω mesons within the bin counting range $N_{\omega}^{\mathrm{MC}}(A,B)$ by the total number of ω mesons N_{ω}^{MC}. By dividing the extracted yield in the range [A,B] by the fraction ϵ the total raw yield can be estimated for each p_{T} interval. Since the yield is extracted for $3 \times 2 = 6$ different bin counting ranges and this for each of the four background estimation methods, $4 \times 6 = 24$ raw ω yields are calculated. All are equally justified. The 24 yields can be seen in Figure 5.9, none is better or worse than the others.

Here the marker styles indicate the different bin counting ranges, while the colors correspond to the four background estimation methods. Assuming that all methods are equally justified, one method needs to be chosen for the final spectrum with well-defined uncertainties.

Choice of default spectrum

A spectrum that represents a good average compared to the other results is favored. To do this, the mean of the 24 extracted yields is calculated in each p_{T} interval to create a mean distribution (red markers, in Figure 5.11). To compare how close the single spectra are to the average distribution a Δ_i value is defined. Δ_i is calculated as the squared sum of the relative deviation in each p_{T} interval from the mean for each distribution:

$$\Delta_i = \sum_{p_{\mathrm{T}}} \left(\frac{y_i(p_{\mathrm{T}}) - \bar{y}(p_{\mathrm{T}})}{\bar{y}(p_{\mathrm{T}})} \right)^2, \tag{5.5}$$

where $\bar{y}$ is the mean value in the given p_{T} interval and y_i is the value of the i-th spectrum.

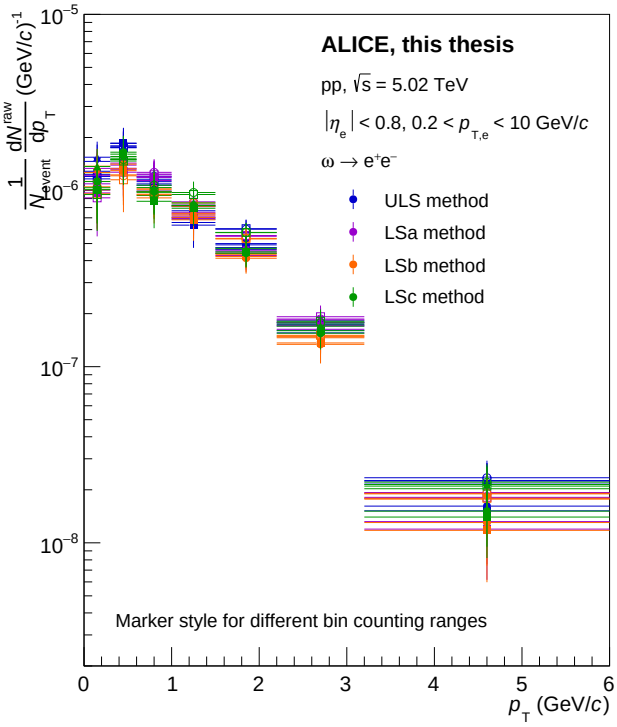

Figure 5.9: Raw ω yield for all four methods (marker colors) each calculated for the six bin counting ranges (marker styles).

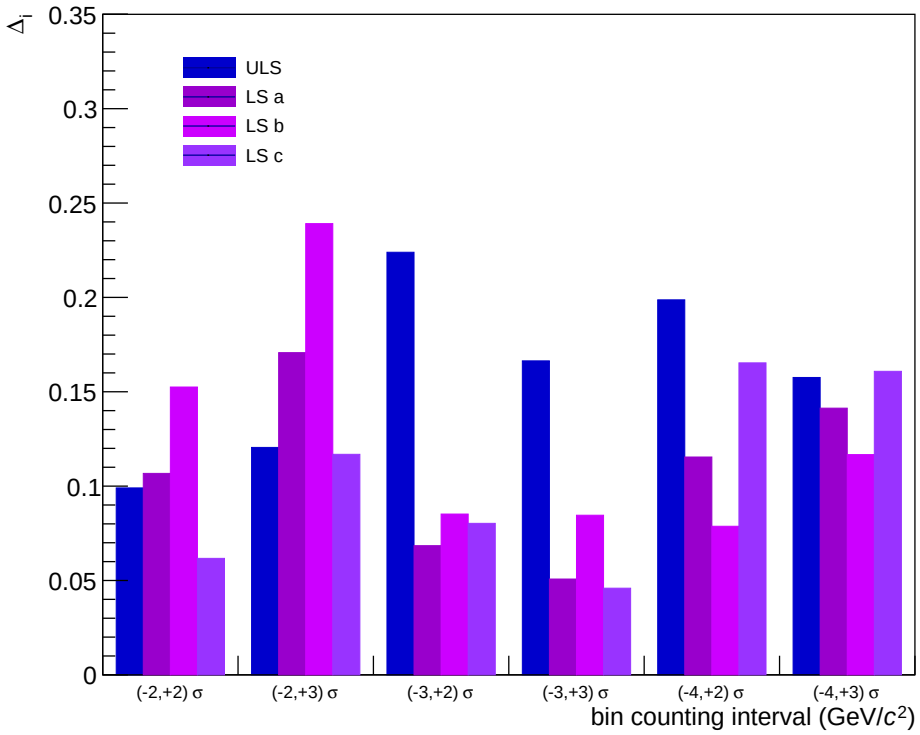

Figure 5.10: The Δ_i-values for each combination of method and bin counting range. The smallest Δ_i-value is given by the LSc method in the bin counting range $(-3, +3)\sigma$.

The smaller the Δ value, the closer the distribution is to the mean over all p_{T} intervals. The Δ_i values for all combinations (method and signal ranges) are shown in Figure 5.10 as a bar chart. It shows that none of the methods (colors) nor bin counting ranges (groups of four) is particularly favored. All values are in a similar range. This is a good indication that all combinations give a reasonable description of the background, although different approaches are used. The smallest value is calculated for the LSc method with a counting range of $[-3\sigma, 3\sigma]$ or $(0.75 - 0.81)\mathrm{GeV}/c^2$, which defines now the default raw yield for the analysis. In Figure 5.11 all raw yields are shown in gray, except the default raw yield, which is shown in violet, and the mean distribution in red.

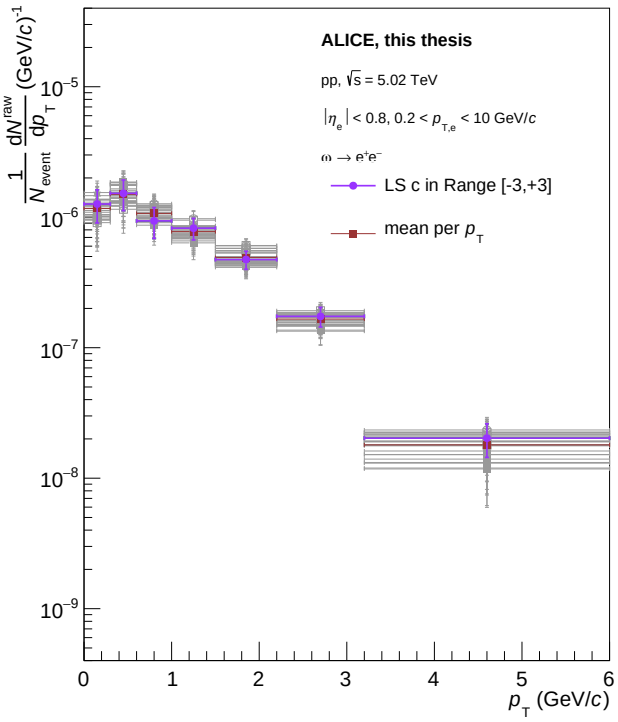

Figure 5.11: Mean values of each p_{T} interval (red) of all 24 raw yields (gray markers) with the yield closest to this mean distribution (violet, LSc method) chosen with Eq. 5.5.

5.2 Corrections

In order to extract the yield of ω mesons produced in pp collisions at $\sqrt{s} = 5.02$ TeV, corrections for efficiency losses in this analysis have to be applied. In the following, the required corrections and their values are discussed in detail.

5.2.1 Corrections for the minimum bias ω yield

To obtain a fully corrected differential yield per rapidity unit in pp collisions at $\sqrt{s} = 5.02$ TeV ($d^2N/dydp_{\mathrm{T}}$), the raw yield (S) has to be normalized and corrected for different experimental inefficiencies and selections. The primary vertex reconstruction efficiency (ϵ_{pv}) is already taken into account in the background estimation steps via the normalization to the correct number of minimum bias events ($\frac{\epsilon_{\mathrm{pv}}}{N_{\mathrm{trigger}}}$). This efficiency is calculated for the dielectron production paper and is taken from the corresponding analysis note with $\epsilon_{\mathrm{pv}} = 96\%$. [22]
Other corrections are needed. One of the most trivial is the *branching ratio* ($\mathrm{BR}_{\omega\to \mathrm{e^+e^-}}$), which takes into account that only a fraction of the ω mesons decay into the dielectron channel, with $\mathrm{BR}_{\omega\to \mathrm{e^+e^-}} = (7.38 \pm 0.22) \times 10^{-5}$. The value is taken from the PDG [3].
The acceptance $\times$ efficiency ($A(p_{\mathrm{T}}) \cdot \epsilon(p_{\mathrm{T}})$) correction will be discussed in more detail in the following section. The corrected differential yield in minimum bias pp collisions is defined as

$$\frac{1}{N_{\mathrm{MB}}} \frac{d^2N}{dp_{\mathrm{T}}dy} = \frac{\epsilon_{\mathrm{pv}}}{N_{\mathrm{trigger}}} \frac{1}{dp_{\mathrm{T}}dy} \frac{1}{\mathrm{BR}_{\omega\to \mathrm{e^+e^-}}} \frac{S(p_{\mathrm{T}})}{A(p_{\mathrm{T}}) \cdot \epsilon(p_{\mathrm{T}})}. \tag{5.6}$$

Acceptance $\times$ Efficiency

The acceptance $\times$ efficiency ($\frac{1}{A(p_{\mathrm{T}})\times\epsilon(p_{\mathrm{T}})}$) correction is applied as a function of p_{T} of ω and is estimated with a full MC simulation. This takes into account the signal losses due to the selection criteria for the tracks and electron candidates (efficiency: ϵ), defined as $\epsilon(p_{\mathrm{T}}) = N_{\omega,\mathrm{rec.}}/N_{\omega,\mathrm{acc.}}$. Also accounted for are effects due to the detector acceptance limits of the daughter particles of generated ω (acceptance: A), defined as $A(p_{\mathrm{T}}) = N_{\omega,\mathrm{acc.}}/N_{\omega,\mathrm{gen.}}$. From these definitions follows the acceptance $\times$ efficiency:

$$A(p_{\mathrm{T}}) \cdot \epsilon(p_{\mathrm{T}}) = \frac{N_{\omega,\mathrm{rec.}}}{N_{\omega,\mathrm{gen.}}}, \tag{5.7}$$

$N_{\omega,\mathrm{gen.}}$: Number of generated ω mesons within the $|y| < 0.8$ window which decays into $\mathrm{e^+e^-}$ pairs.

$N_{\omega,\mathrm{acc.}}$: Number of ω mesons within the $|y| < 0.8$ window which decays into $\mathrm{e^+e^-}$ pairs and for which the decay electrons and positrons are within the fiducial detector acceptance:
and dielectron decay ($\omega \to \mathrm{e^+e^-}$)
and the daughter particles ($\mathrm{e^+e^-}$) within fiducial acceptance: $|\eta_e| < 0.8$ & $p_{\mathrm{T,e}} > 0.2$ GeV/c.

$N_{\omega,\mathrm{rec.}}$: Number of ω (within $|y| < 0.8$) reconstructed from the daughter particles that are within the fiducial acceptance: $|\eta_e| < 0.8$ & $p_{\mathrm{T,e}} > 0.2$ GeV/c and passed the track (see Table 5) and PID (see Table 6) selection criteria.

The results from the MC simulation for $N_{\omega,\mathrm{gen.}}$, $N_{\omega,\mathrm{acc.}}$ and $N_{\omega,\mathrm{rec.}}$ can be seen in Figure 5.12 as a function of p_{T}. In Figure 5.13 the product of acceptance and efficiency is shown. In the lower p_{T} range, acceptance $\times$ efficiency is below 10% going up to 20% for higher p_{T}.

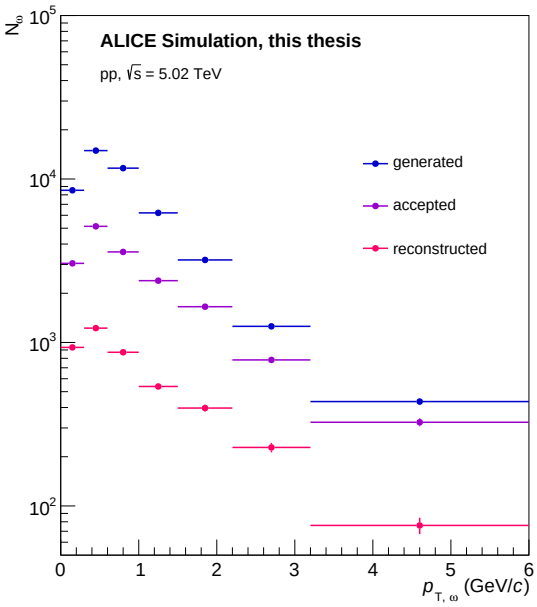

Figure 5.12: The generated (blue), accepted (purple), and reconstructed (magenta) number of ω mesons from the full MC simulation.

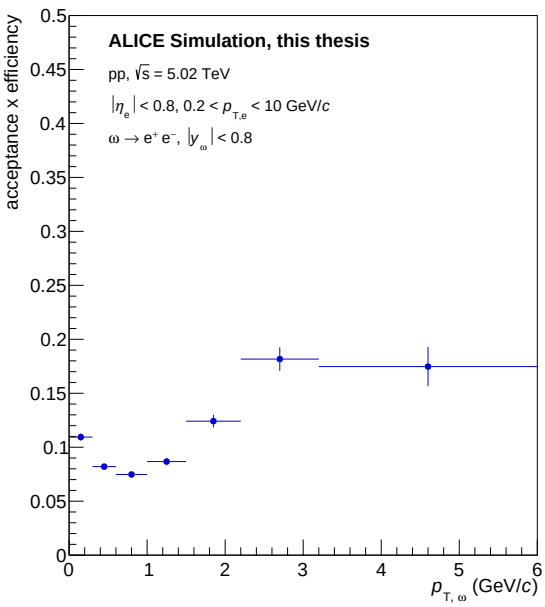

Figure 5.13: Acceptance $\times$ efficiency as a function of p_{T}.

Minimum bias ω yield

With Equation 5.6 the raw yield shown in Figure 5.11 is corrected. The differential yield for MB pp collisions at $\sqrt{s} = 5.02$ TeV is shown in Figure 5.14 as a function of p_{T}.

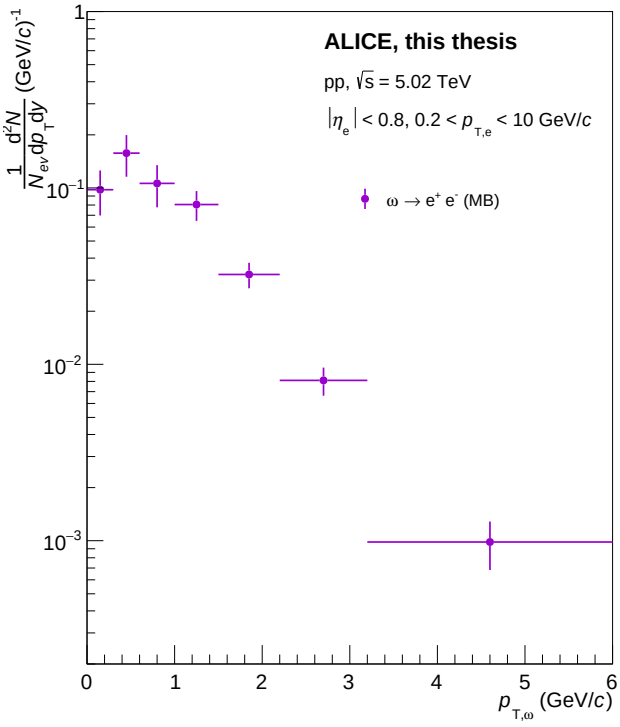

Figure 5.14: Corrected ω spectrum for MB pp collisions at $\sqrt{s} = 5.02$ TeV.

5.2.2 Corrections for the inelastic ω yield

Further corrections can be made, to get a trigger-independent measurement, i.e. the corrected ω yield in inelastic pp collisions. For this, additional corrections are needed, shown as the boxed part in Eq. 5.8.

$$\frac{1}{N_{\text{inel}}} \frac{d^2N}{dp_{\text{T}}dy} = \frac{\epsilon_{\text{pv}}}{N_{\text{trigger}}} \frac{1}{dp_{\text{T}}dy} \frac{1}{\text{BR}_{\omega\to e^+e^-}} \frac{S(p_{\text{T}})}{A(p_{\text{T}}) \cdot \epsilon(p_{\text{T}})} \boxed{\frac{\sigma_{\text{MB}}}{\sigma_{\text{inel}} \cdot \epsilon_{\text{trigger}}(p_{\text{T}})}}. \tag{5.8}$$

Here the cross section for inelastic as well as MB pp collisions at $\sqrt{s} = 5.02$ TeV are needed, with the already mentioned cross section for MB pp collisions $\sigma_{\text{MB}} = 50.87 \pm 0.04$ mb [32]. For the cross section for inelastic pp collisions the value $\sigma_{\text{inel}} = 67.6 \pm 0.6$ mb is used. It is extracted from a precise data-driven parametrization of many measurements performed at LHC energies [33].

Trigger efficiency

To account for the lost ω signal due to the trigger conditions the trigger efficiency ($\epsilon_{\text{trigger}}$) has to be calculated using once again a full MC simulation. Used as reference values for this efficiency is the amount of ω signal within the $|y| < 0.8$ window and with an e^+e^- decay, where no minimum bias trigger is required. The comparison of this reference to the selected ω signal where the event selection and minimum bias trigger condition were fulfilled gives $\epsilon_{\text{trigger}}$. The ratio of selected to reference ω signals is shown in Figure 5.15. The trigger efficiency $\epsilon_{\text{trigger}}$ is applied in each interval of the measurement.

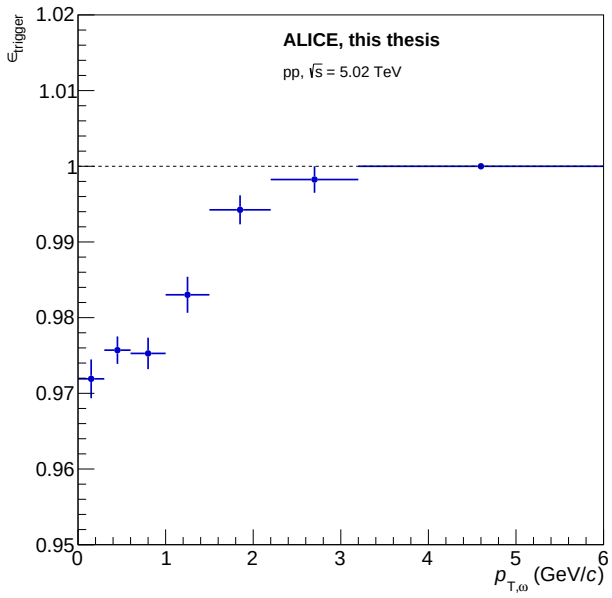

Figure 5.15: Signal loss efficiency due to trigger and event selection for the ω.

Inelastic ω yield

The fully corrected ω spectrum as a function of p_{T} is shown in Figure 5.16. Here the differential yield for inelastic pp collisions at $\sqrt{s} = 5.02$ TeV at midrapidity is compared to the yield in minimum bias pp collisions.

A further check for the previously determined default method is shown in Figure 5.17. Here the integrated ω yield (dN/dy) in the p_{T} interval $0-6$ GeV/c is shown for the 24 different raw yields as results of the method and bin counting range combinations. The default method LSc in the bin counting range $(-3, +3)\sigma$ is highlighted by a gray background. The comparison of the default method with the mean of all methods shows unambiguously that no outlayer was chosen as default.

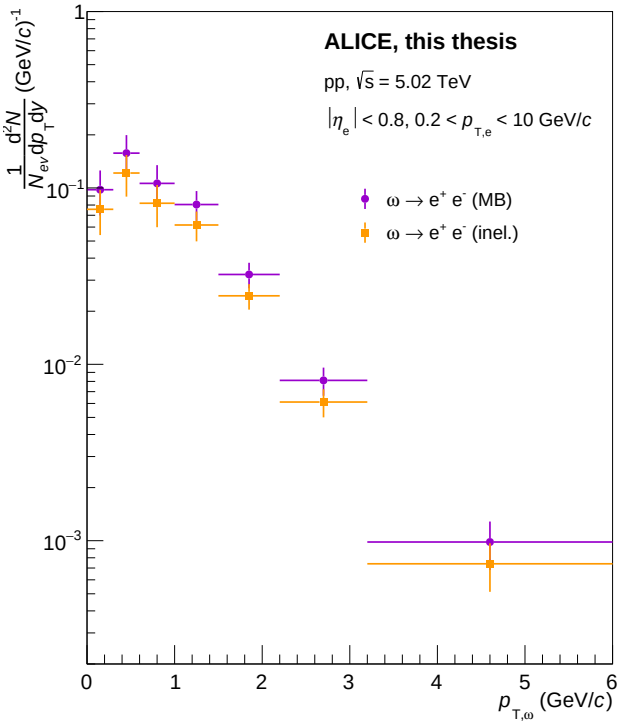

Figure 5.16: Corrected ω spectrum for MB(purple) and inelastic(orange) pp collisions at $\sqrt{s} = 5.02$ TeV.

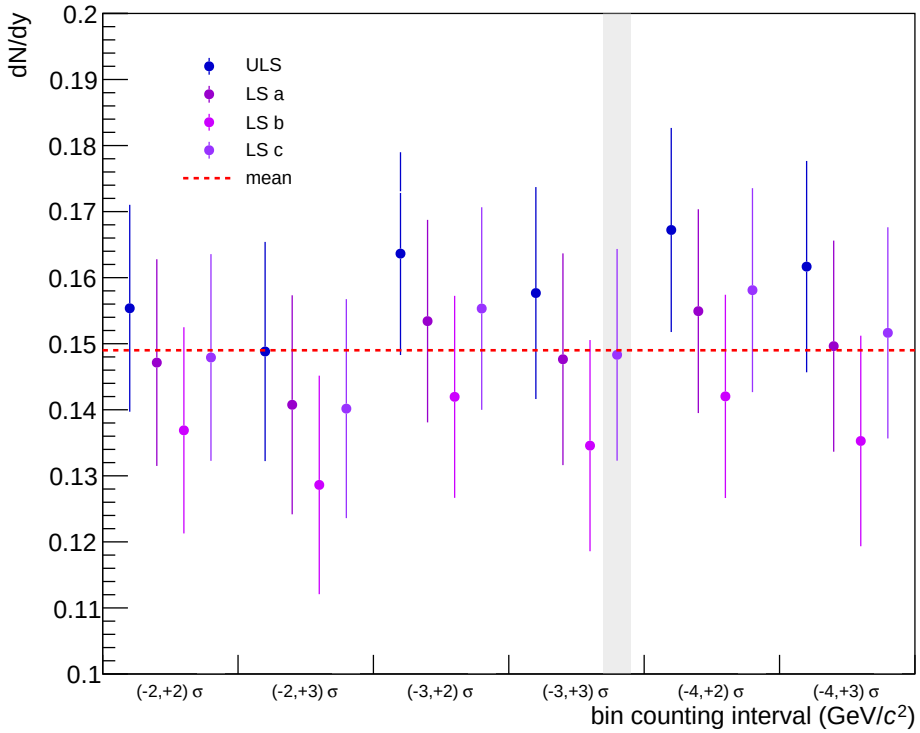

Figure 5.17: Integrated yield in the p_{T} interval $0 - 6$ GeV/c, for every method and bin counting range combination. The yield for the highlighted default method (LSc-method, $(-3, +3)\sigma$) is close to the mean.

5.3 Systematic uncertainties

The estimation of systematic uncertainties of different origins has to be taken into account. These uncertainties are connected to corrections as well as assumptions that were made throughout the analysis. All those assumptions are justified, but may result in small biases. Such assumptions are for example, that the background (all or combinatorial contributions) is smooth and can be described by a `pol2` function.
In the following, the uncertainties originating from the signal shape, the background estimation, the signal extraction, and the Monte Carlo to data matching as well as less relevant sources will be discussed in detail. However, some systematics are correlated with each other such that variations of selection criteria or assumptions for each source on its own would result in an overestimation of those systematic uncertainties. To avoid this, the systematic uncertainties for background estimation and signal extraction are estimated together.

Rectangular distribution

Throughout this section, the assumption is made that the distribution of the results obtained by varying the selection criteria or assumptions to estimate the systematic uncertainties is uniform (rectangular). The rectangular distribution is defined as:

$$f(x) = \begin{cases} \frac{1}{b-a} & \text{for } a < x < b \\ \\ 0 & \text{for } (x < a)||(x > b), \end{cases} \tag{5.9}$$

with a and b being the minimum and maximum of the distribution. The value of $1/(b-a)$ ensures a probability density, here the amplitude is rather irrelevant. The mean or expectation value (first moment) of this distribution ($E(X)$) is then given as

$$E(X) = \int_a^b x^1 dx \times \frac{1}{b-a} = \left[\frac{x^2}{2}\right]_a^b \times \frac{1}{b-a} = \frac{b^2-a^2}{2(b-a)} = \frac{(b+a)}{2}. \tag{5.10}$$

With this, the variance $V(X)$ or the second central moment of the distribution can be calculated as:

$$V(X) = \sigma^2 = E\left((X - E(X))^2\right) = \int_a^b \left(x - \frac{a+b}{2}\right)^2 \frac{dx}{b-a} = \frac{1}{12}(b-a)^2. \tag{5.11}$$

Considering that a and b are the minimum and the maximum of the distribution, then the width of the distribution is given by:

$$\sigma = \frac{\max - \min}{\sqrt{12}}. \tag{5.12}$$

Barlow criterion

If the systematic uncertainties are estimated by using very different distributions that share a large overlap concerning the underlying data, one can follow the suggestions by Barlow to only take statistically significant distributions into account. [34] Here the distributions have to pass the, in the following called, Barlow criterion. The technical steps for the Barlow criterion will be described in the following lines. In a sense, the p_{T}-differential spectra obtained after varying the selection criteria are partial subsets of each other and not statistically independent. To not include results that exhibit large fluctuations the Barlow criterion tests the distributions to be statistically significantly different from a default distribution. To do so the average Barlow number has to be calculated for each distribution i ($\langle B_i \rangle$) as the sum over j p_{T} intervals of the differences of the reference distribution (R_j) to the current distribution (C_{ij}). The differences in each p_{T} interval are normalized to its statistical uncertainties assuming that one distribution is a subset of the other. Finally, the number is normalized to the total number of p_{T} bins (n) that have to be compared

$$\langle B_i \rangle = \sum_{j=1}^{n} \frac{|R_j - C_{ij}|}{\sqrt{|\sigma^2_{C_{ij}} - \sigma^2_{R_j}|}} / n. \tag{5.13}$$

Only if the current distribution passes the Barlow criterion it is taken into account in the estimation of the systematic uncertainty. The exact value is then chosen for the specific application case. In this analysis, only the distributions with $\langle B_i \rangle \leq 2$ are considered. The limit 2 is chosen as a sufficient number for this analysis to select statistically significant different distributions where there are still enough distributions that pass the criterion to be able to estimate the uncertainty.

5.3.1 Signal shape

Since an assumption on the signal shape is made (crystal ball function), tests were carried out to validate this assumption. For this test, other functions were used to parameterize the tail and peak part of ω mass signal from MC simulations in the single p_{T} bins. The used functions are: Landau (L), Landau and Gaussian added with the same mean value (LG(1)), Landau and Gaussian added with different mean values (LG(2), here the Gaussian mean is fixed to the pole mass of the ω), and last a convoluted Landau Gaussian parameterization function (LG(3)). All four alternative functions together with the crystal ball function are shown in Figure 5.18. Once again only for the ($0.3 < p_{\mathrm{T}} < 0.6$) GeV/$c$ interval, the graphs for all p_{T} intervals can be found in Figure A.9.

None of the functions seem to provide a significantly better or worse description. Further tests to investigate the overall agreement of the different functions with the full MC simulation are shown in Table 9. For this test, the integrals of the five parameterized functions were calculated in the range of $0.6 < m_{\mathrm{ee}} < 0.9$ GeV/c^2 and compared to the integration of the MC signal in the same range. The integrals are shown for all p_{T} intervals, as well as for the whole integrated p_{T} range $(0-6)$GeV/c for the MC signal and crystal ball function only.

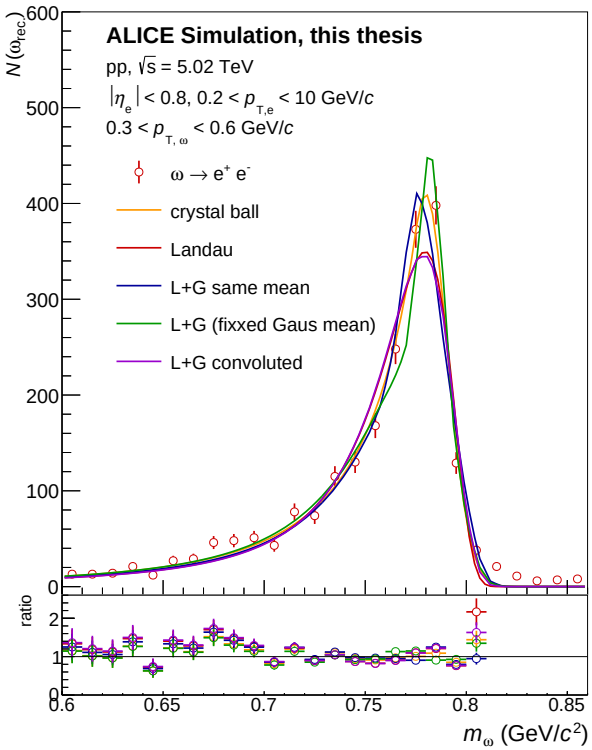

Figure 5.18: Reconstructed ω signal in MC data after fiducial and track selections for the $(0.3 < p_{\mathrm{T}} < 0.6)$ GeV/c interval, described by alternative functions for the CB: Landau (red), Landau+Gaussian (L+G) same mean (blue), Landau+Gaussian fixed Gaussian mean (green) and Landau Gaussian convoluted (purple). Same color code for the ratio of data/parameterization.

p_{T} [GeV/c]	χ^2 MC	CB	L	LG(1)	LG(2)	LG(3)
$0.0-0.3$	13.27	12.56(5.37%)	12.21(7.95%)	12.37(6.78%)	12.72(4.15%)	12.21(7.95%)
$0.3-0.6$	21.44	20.29(5.37%)	19.91(7.14%)	20.13(6.11%)	20.25(5.53%)	19.93(7.04%)
$0.6-1.0$	14.47	13.67(5.51%)	13.36(7.66%)	13.57(6.21%)	13.68(5.47%)	13.37(7.63%)
$1.0-1.5$	9.57	9.00(5.96%)	8.79(8.17%)	8.84(7.64%)	8.95(6.51%)	8.79(8.17%)
$1.5-2.2$	6.24	5.85(6.22%)	5.73(8.22%)	5.86(6.02%)	5.89(5.66%)	5.76(7.63%)
$2.2-6.0$	4.28	4.04(5.63%)	3.92(8.43%)	4.04(5.67%)	4.05(5.39%)	3.99(6.71%)
$0.0-6.0$	69.27	66.19(4.44%)				

Table 9: Integrals of the full monte-carlo simulation (MC), the crystal ball (CB), the Landau (L), and different combinations of a Landau with a Gaussian (LG) function (see text). In parenthesis, the relative differences between the function's integral to the MC integral are given.

It can be observed, that all functions show a systematically smaller integral than the integration of the MC signal. The relative differences between the function's integral to the MC integral and range from around 5 to 8% depending on the function and p_{T} interval.

Since no function was found that describes the signal shape in every p_{T} bin with maximal precision, it was concluded that the MC histograms are used for the parameterization to correct for the bin counting intervals. For systematic uncertainty estimations of the signal extraction the integration of the crystal ball function is later added as an additional variation.

5.3.2 Signal extraction

As already mentioned the systematic uncertainty estimation of background and signal extraction are correlated, there is no way to vary one without influencing the other. In this subsection, the estimated uncertainty arising from the choice of the background estimation method, as well as the region in which the signal is counted and how it is counted is presented. Additional variations compared to those described in section 5.1 are considered. They are all summarized in Tab. 10.

	ULS	LS		
		a	b	c
background estimation (11 variations)				
`pol2`-Fit	X	X	X	X
`pol3`-Fit	X	X	X	X
LS spectrum (no fit)		X	X	X
signal extraction (7 variations)				
bin counting in 6 signal ranges				
integration of the crystal ball function				

Table 10: Variations used for the systematic uncertainty estimation of signal extraction/ background estimation. A total of 77 variations result from 11 background estimations and 7 signal extraction variations. Gray rows indicate the variation used for the default method estimation.

For the determination of the default method, the background was described using a second-order polynomial function (`pol2`) and the extraction of the ω yield is done in six different signal ranges. The correction for the signal outside the signal range was then corrected using the ω signal from MC.
For the systematic uncertainty estimation, the background is also estimated using a third-order polynomial function (`pol3`) to describe the combinatorial background in the first step of the LS methods or all background components in the ULS method. Additionally, the LS spectrum was subtracted without parameterizing the LS spectrum first, as it is done in other analyses. This results in a total of 11 variations for the background estimation. In addition, the signal extraction is varied from the bin counting in different signal ranges to the integration of the crystal ball function. This leads to a total of 7 variations for the signal extraction (six from the bin counting in 6 signal ranges + one from the crystal ball integration).

A total of $(11 \times 7) = 77$ raw yields are used to estimate the systematic uncertainties from background estimation and signal extraction. They are shown in Figure 5.19. Overall the distributions are close to each other, except for the $(0.3 < p_{\mathrm{T}} < 0.6)$ GeV/c interval where

the subtraction of the LS spectrum without a parameterization results in large statistical uncertainties as well as an overall drop of the yield values.

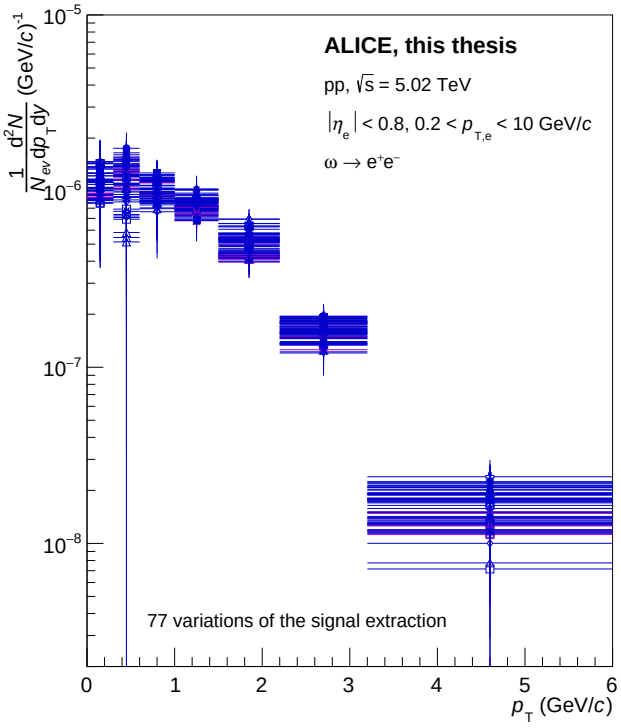

Figure 5.19: Corrected p_{T}-differential yield in MB pp collisions at $\sqrt{s} = 5.02$ TeV for all 77 variations considered in the background and signal extraction estimation.

Since all methods are equally justified the uncertainty is given by the width of the distributions or the spread of the spectra in each p_{T} bin. To estimate the systematic uncertainty two approaches were tested, shown in Figure 5.20. On the left, the systematic uncertainties were estimated using all 77 variations, and on the right using only the 46 variations, that passed the Barlow criterion ($\langle B_i \rangle \geq 2$, Eq. 5.13). Here it can already be seen, that the yields, that had large statistical uncertainties in the ($0.3 < p_{\mathrm{T}} < 0.6$) GeV/$c$ interval are not significant enough to pass the Barlow criterion. In both lower panels of Figure 5.20, the calculated systematic uncertainties are shown, using the RMS (red) and using the $\frac{(max-min)}{\sqrt{12}}$ (blue) shown in percent. The systematic uncertainty shown in the upper panel (left) is obtained with the RMS of all variations, whereas the RMS and on the right the systematic uncertainty for the passed Barlow criterion variations are shown as the results of $\frac{(max-min)}{\sqrt{12}}$. Exact values and percentages for all systematic uncertainty estimations of Figure 5.20 are also shown in Table 11. The systematic uncertainties are ranging from 11% up to 28%.

Taking a closer look at Table 11, RMS and $\frac{(max-min)}{\sqrt{12}}$ using all variations result in very similar values. This leads to the conclusion that the assumption of a rectangular distribution is justified. In addition, the RMS of all variations and the $\frac{(max-min)}{\sqrt{12}}$ values for the variations that passed Barlow are overall in good agreement. The latter is used for the final systematic uncertainties. The systematic uncertainty does not show any significant p_{T} dependence and ranges from 12% to 22%. It is propagated p_{T}-bin per p_{T}-bin.

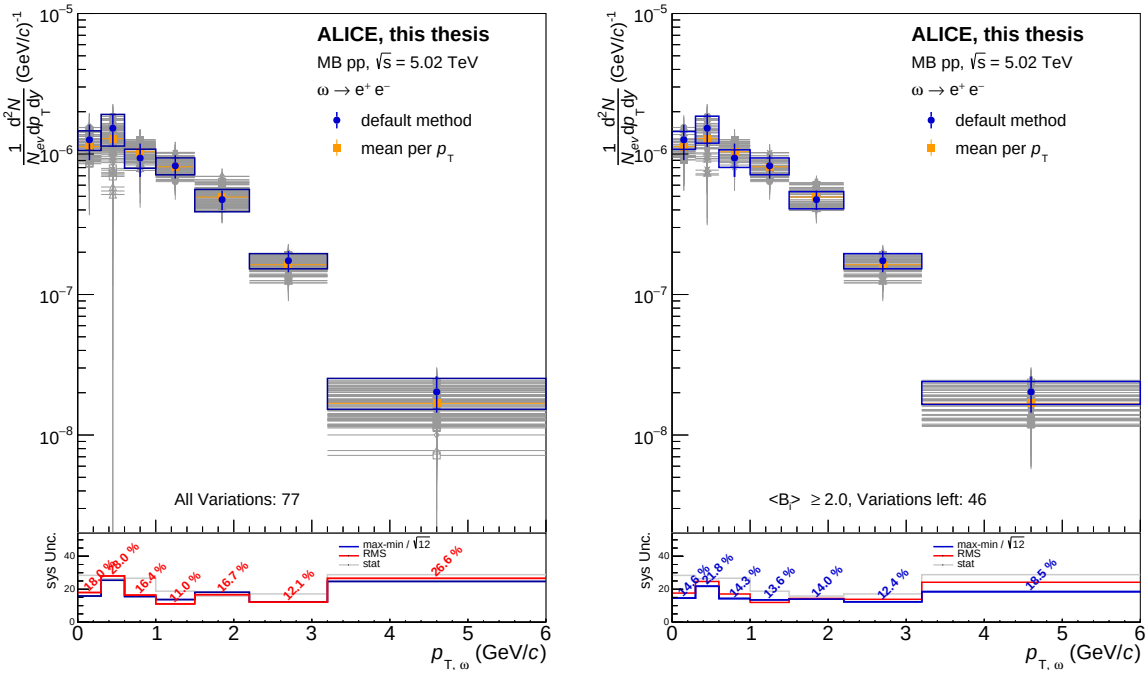

Figure 5.20: Corrected ω yield in MB pp collisions at $\sqrt{s} = 5.02$ TeV with the systematic uncertainties from background estimation and signal extraction. The orange full squares show the mean per p_{T}, in blue the default method, and in gray the variations for the systematic uncertainty estimation. (left) All 77 variations (right) and variations that passed the Barlow criterion. The systematic uncertainties are shown in the lower panel in percentage, for each calculated using the RMS (red) and $\frac{(max-min)}{\sqrt{12}}$ (blue). The statistical uncertainties are shown in comparison as the grey line.

5.3.3 Monte Carlo data matching

The MC simulations are used to correct for the acceptance and efficiency of the detector due to different effects, including inefficiencies in reconstructing particle tracks, selections on the track level to ensure good analysis performance, as well as the selections in the TPC and TOF to select the electron candidates. Since the MC distributions don't describe the real distributions perfectly, the uncertainty that is introduced by this mismatch of MC and real data has to be estimated.

This analysis follows the same approach as already used in several analyses before [28]. Here, the selection criteria for track and PID are varied randomly within reasonable limits of the analysis selections. This analysis uses the same variations as the dielectron production paper [22]. Here the random variations started with a set of 30 different selection criteria, but 8 of those variations required 4 ITS hits. Due to the two SDD layers of the ITS missing in the analysed dataset, those selection sets require hits in all available ITS layers of this datasets. Per consequent with these 8 selection criterion sets the number of reconstructed electrons/positrons was found to be significantly lower, with corrected yields also smaller than the average pointing to an imperfect description of all dead zones of the ITS. Because this analysis needs high statistics, these 8 variations were disregarded. The variations are then done for a set of 22 different selection criteria, summarised in Table A.1 in the appendix. The default selection criteria in this table is No. 4.

p_{T} [GeV/c]	default values $[10^{-8}]$	all $[10^{-8}]$		passed Barlow $[10^{-8}]$	
		RMS	$\frac{(max-min)}{\sqrt{12}}$	RMS	$\frac{(max-min)}{\sqrt{12}}$
$0.0-0.3$	126.2	22.7(18.0%)	20.0(15.8%)	22.3(17.6%)	18.4(14.6%)
$0.3-0.6$	152.6	42.8(28.0%)	38.8(25.4%)	37.7(24.7%)	33.2(21.8%)
$0.6-1.0$	93.7	15.4(16.4%)	14.6(15.5%)	16.0(17.1%)	13.4(14.3%)
$1.0-1.5$	82.5	9.1(11.0%)	11.3(13.7%)	9.9(12.0%)	11.2(13.6%)
$1.5-2.2$	47.4	7.9(16.7%)	8.6(18.1%)	6.8(14.4%)	6.6(14.0%)
$2.2-3.2$	17.4	2.1(12.1%)	2.2(12.4%)	2.4(13.9%)	2.2(12.4%)
$3.2-6.0$	2.0	0.5(26.6%)	0.5(24.7%)	0.5(24.2%)	0.4(18.5%)

Table 11: Systematic uncertainties calculated for the background estimation and signal extraction (see text).

An alternative approach would be to vary each parameter alone and add the variations on the final spectrum. However, the approach followed here has the major advantage, that possible correlations between for example the track parameters are taken into account, which would in the alternative approach lead to a double counting of uncertainties.

The whole analysis is repeated for each set of selection criteria, starting from the background estimation using the signal shape, cocktail templates, and correction factors from the corresponding MC simulation. The default method is chosen each time according to the smallest difference to the mean distribution and then fully corrected for each set using Eq. 5.6. Figure 5.21 shows the variation of the product of acceptance and efficiency, while the 22 resulting corrected ω yields are shown in Figure 5.22.
To check if the default selection criteria of this analysis (variation 4) is close to the mean distribution from all sets of selection criteria, the Δ_i values are calculated for every variation with Eq. 5.5. The results are shown in Figure 5.23. As discussed before the Δ_i shows the average difference to the mean distribution. The default variation (selection set 4) is one of the variations with smaller Δ_i values. Therefore the analysis will continue using this variation as the default setting for this analysis.

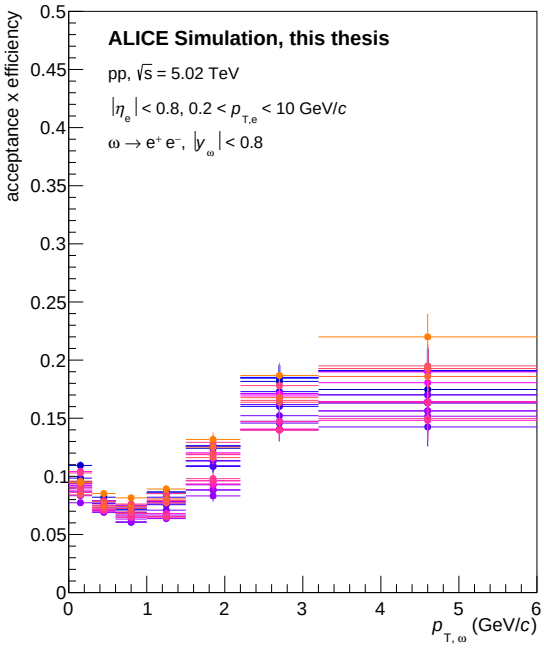

Figure 5.21: Acceptance × Efficiency for all 22 selection criterion variations.

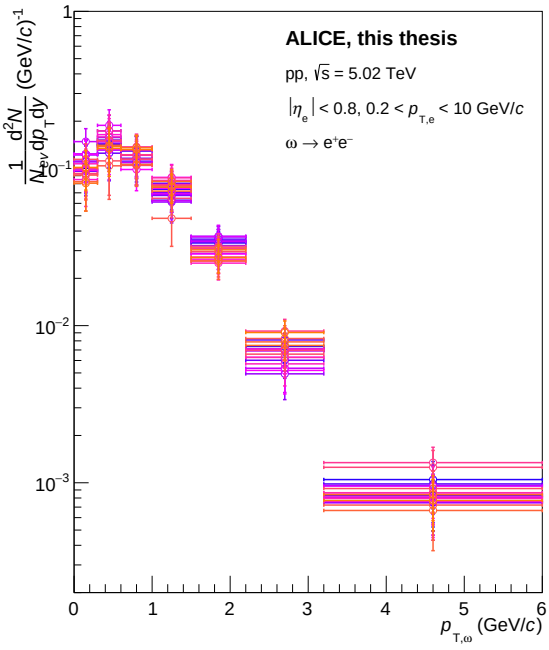

Figure 5.22: Corrected ω yield in MB pp collisions at $\sqrt{s} = 5.02$ TeV for the 22 selection criterion variations.

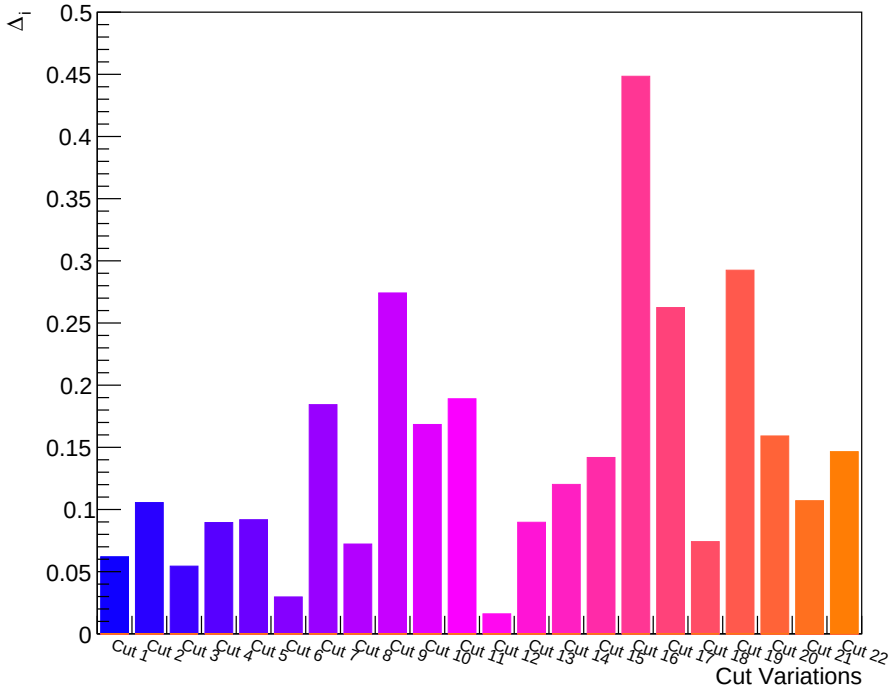

Figure 5.23: Δ_i-values for all 22 selection criterion variations (see text).

The systematic uncertainties are again calculated under the assumption of a flat distribution with Eq. 5.12. Since the different raw spectra are partial subsets of each other, the suggestion of Barlow to take only statistically significant variations are followed. The suggestions by Barlow are followed by calculating the average Barlow number as shown in Eq. 5.13. Only distributions with $\langle B_i \rangle \geq 2$ are then considered to estimate the uncertainty. All in all 13 of the 22 yields fulfill this criterion. In Figure 5.24 the yield obtained with the default selection criteria (purple) is shown together with the 13 significantly different yields (gray). The systematic uncertainties estimated by varying the selection criteria are shown in each p_{T}-bin in the lower pad vary between 10% and 18%.

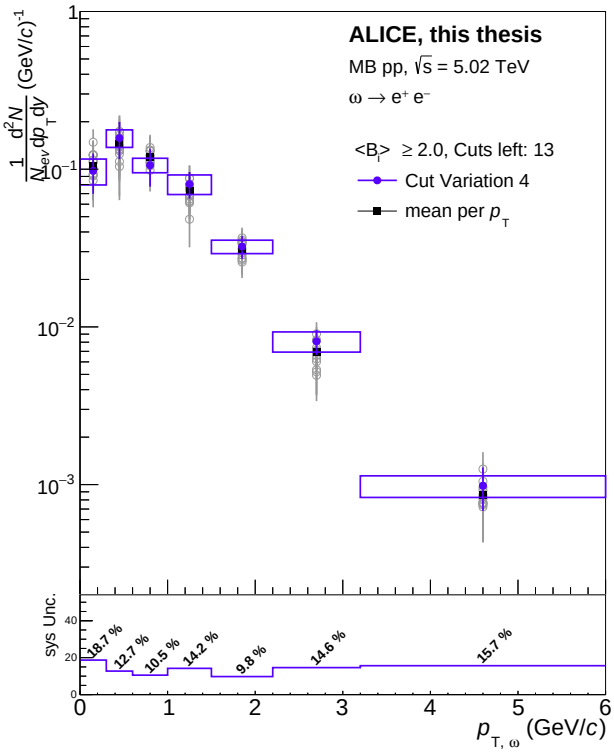

Figure 5.24: Corrected ω yields in MB pp collisions at $\sqrt{s} = 5.02$ TeV with the systematic uncertainties from the variations of selection criteria. In the lower pad, the percentage of the systematic uncertainties is shown for each bin.

The uncertainties as estimated above and the ones calculated using the RMS of all 22 yields is shown in Table 12.

The relative uncertainties determined from the $\frac{(max-min)}{\sqrt{12}}$ of the yields that passed the Barlow criterion are (except in the first p_{T} bin) slightly smaller than the ones using the RMS of the whole set of distributions. As the sample size of 22 corrected spectra and only 13 after applying the Barlow criterion is rather small, it was decided to use the RMS of a rectangular distribution, as already done for the systematic uncertainty of the signal extraction.

5.3.4 Additional contributions

In addition to the contributions to the systematic uncertainties discussed so far, the following contributions are added after discussion with the collaboration. As these contributions do

p_{T} [GeV/c]	default values	passed Barlow $\frac{(max-min)}{\sqrt{12}}$		all RMS	
$0.0-0.3$	0.0977	0.0183	(18.7%)	0.0184	(18.8%)
$0.3-0.6$	0.1575	0.0201	(12.7%)	0.0227	(14.4%)
$0.6-1.0$	0.1061	0.0112	(10.5%)	0.0174	(16.4%)
$1.0-1.5$	0.0805	0.0114	(14.2%)	0.0121	(15.0%)
$1.5-2.2$	0.0323	0.0032	(9.8%)	0.0040	(12.4%)
$2.2-3.2$	0.0081	0.0012	(14.6%)	0.0016	(19.8%)
$3.2-6.0$	0.0010	0.0002	(15.7%)	0.0002	(19.7%)

Table 12: Systematic uncertainties calculated by varying the selection criteria (see text).

not concern only this analysis and were evaluated by members of the ALICE Collaboration, the description of these uncertainties is only briefly discussed. These additional contributors to the systematic uncertainties are corrections concerning the material budget, matching efficiency of ITS and TPC, uncertainties for the requirement of a hit in the first layer of the ITS (SPD1), and bin counting corrections.

Material budget

As discussed in detail in [35], the description of the material budget in the GEANT implementation of the ALICE detector used for the central MC productions is not perfect. Because the tail of the ω signal results from the Bremsstrahlung of the electrons/positrons in the detector material, the impact of a change in the material budget is investigated in the final results and systematic uncertainties resulting from those changes in material budget are derived.

In an updated MC production with an improved description of the detector, the SPD(SDD) layers of the ITS included 20%(8%) more material. Because there is no such updated MC production for pp collisions at $\sqrt{s} = 5.02$ TeV, anchored MC productions to $\sqrt{s} = 13$ TeV pp data (pass2) are used to study the effects of the updated material budget.
This is done by extracting the relative p_{T} resolutions for the electrons from both MC productions with default and updated material budget. This relative p_{T} resolution is then used to estimate the impact on the ω line shape used to estimate the signal shape (see section 5.1.1). To do this, a toy MC is used to generate ω with the p_{T} spectrum measured in this analysis and an $\mathrm{e^+e^-}$ mass distribution based on the relativistic Breit-Wigner function using the PDG [3] value of $m_\omega = (782.66 \pm 0.13)$ MeV/c^2 and a width of (8.68 ± 0.13) MeV/c^2. The decay into $\mathrm{e^+e^-}$ pairs is simulated and the spectrum of the decay products is then smeared using the prior extracted p_{T} resolution.

The ratio of the two different mass shapes of the ω extracted with the default and with the updated material budget is shown in Figure 5.25. As expected the tail of the ω is more pronounced in the simulation with updated (more) material in the detector description in GEANT. To study the impact on the mass shape of the ω signal used in this analysis, as well as the impact on the CB function, the ratio is used to modify the MC signal from the default analysis. The results with and without the modification are shown in Figure 5.26. Here the default MC signal and CB function used in the analysis are shown as red markers and orange, solid line. The updated shape is shown as the open black markers and the corresponding CB

function with the blue dashed line. The CB functions for both parameterizations are very similar.

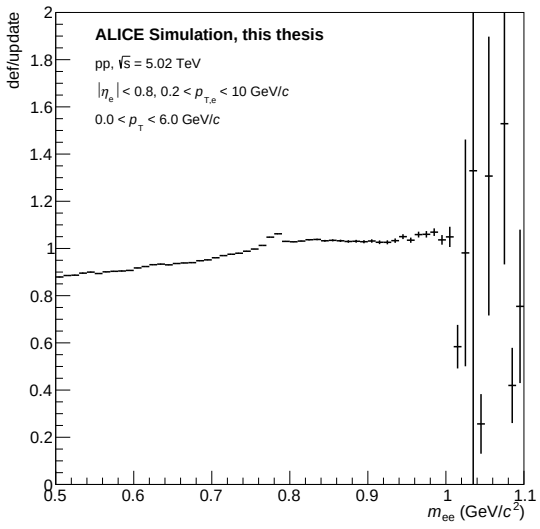

Figure 5.25: Ratio of the e^+e^- mass spectra using the default or the updated p_T resolution.

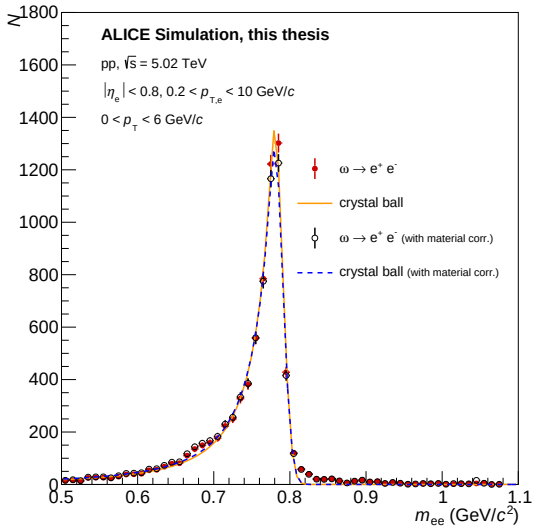

Figure 5.26: MC ω signal without material correction (red, crystal ball orange) and with material correction (black, crystal ball blue).

Following the analysis steps of section 5.1.2 using both MC ω signals (default and updated material budget) shown in Figure 5.26 the corrected ω yields are determined and shown in Figure 5.27. In the upper panel, the results using the default method (black markers) are compared to the results for the same method with the updated CB (green markers). For the bin counting correction, the corresponding MC ω signal is used. The correction factor ($\epsilon = \frac{N_\omega^{\mathrm{MC}}(A,B)}{N_\omega^{\mathrm{MC}}}$, Eq. 5.4) to correct the bincounted raw yield, for signal outside the signal range [A,B] = $(0.75-0.81)\mathrm{GeV}/c^2$, is calculated for different ranges for the updated (ϵ within $(0.5-1.1)$ GeV/c^2) and default material budget (ϵ within $(0-2)$ GeV/c^2) from the MC ω signal (N_ω^{MC}).
In the lower panel, the difference between updated and default raw yield is shown ranging from 1.9% up to 3.2% with no recognizable p_T dependence. The average difference of the whole p_T range is shown as the gray line with a 2.7% difference.
The systematic uncertainty for the material budget is estimated as the differences between the two extracted raw spectra and applied bin by bin.

ITS TPC matching efficiency

The ITS TPC matching efficiency should take into account the differences in the performance of the ITS TPC track matching in data and MC simulations. The study for this efficiency was carried out by the data preparation group and values are provided for the whole collaboration. For the data-taking period used in this analysis, the uncertainties are summarized in Table 13. Assuming that charged particles behave similarly, the available values from pions are taken from [36].
These uncertainties on track level need to be propagated to the ω which is measured by its two decay electrons. To this end, a toy MC approach was used similar to the estimation

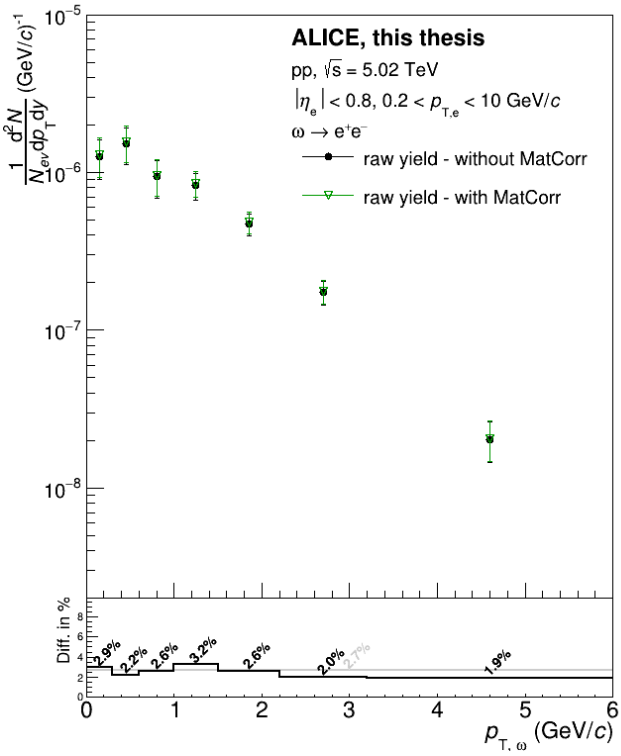

Figure 5.27: Raw ω yield comparison obtained with the default method using the default and material corrected CB function. For the bin counting correction, the corresponding ω signal from MC (see Figure 5.26) is used.

in [22]. It calculates the uncertainty as the sum in quadrature of the uncertainties for the decay electron and the decay positron. The result of the simulation is shown in Figure 5.28 and propagated p_{T}-bin per p_{T}-bin.

p_{T}	uncertainty
0.5 - 2.0 GeV/c	1%
2.0 - 7.0 GeV/c	2%
7.0 - 10.0 GeV/c	1%
10.0 - 15.0 GeV/c	2%

Table 13: Uncertainty on the matching efficiency of ITS and TPC tracks provided by the ALICE data preparation group [36].

Hit in the first layer of the ITS

In the analysis, it is required that each electron candidate has a hit in the first layer of the ITS (SPD1). This selection is not varied, since it would not only vary the selection for primary electrons but massively enhance the contribution from photon conversions. Releasing this requirement for the current analysis is therefore not considered as a reasonable idea.
Under the assumption, that all charged particles are effected similarly by this selection, charged pions with a tight DCA selection are used as a proxy to take only primary pions

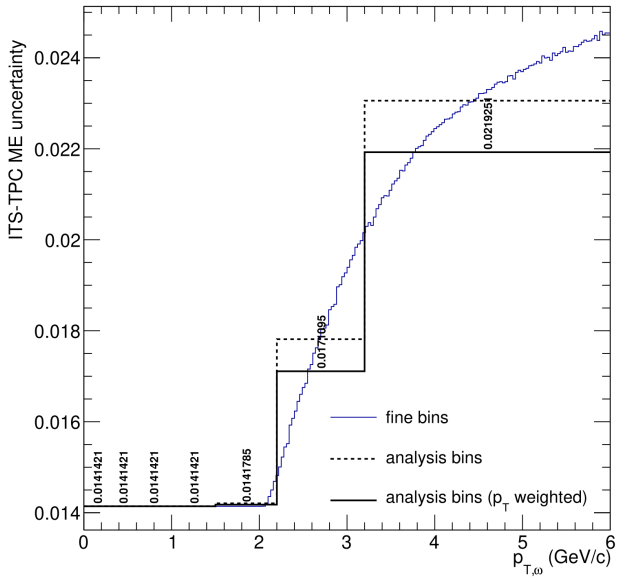

Figure 5.28: Systematic uncertainty on the ω measurement related to the uncertainty of the ITS-TPC matching efficiency.

into account. The double ratio of the raw p_{T}-differential spectra obtained with and without the requirement of a hit in the first ITS layer for data and MC is computed. A deviation from unity of around 2 % is observed. To propagate this uncertainty in the ω spectrum a similar toy MC approach as before is used. The result from the toy MC for the systematic uncertainties of the required hit in the first ITS layer is shown in Figure 5.29 in dependence of p_{T}. The uncertainties are applied p_{T}-bin per p_{T}-bin.

Bin counting correction

As described above, the ω signal from MC histograms is taken into account for the signal outside the bin counting range. Due to the limited statistics of the MC histograms, this correction factor suffers form statistical fluctuations. To account for these fluctuations, the statistical uncertainty is calculated and propagated to the systematic uncertainty of the final measurement. Thus, statistical uncertainties are now incorporated into the systematic uncertainties, as the statistical fluctuations also affect the yield extraction. An overall uncertainty of 2-4% is estimated.

5.3.5 Summary systematic uncertainties

The systematic uncertainties are investigated for the signal extraction method by taking all different approaches into account, values between 12.4% to 21.8% uncertainty were found depending on the p_{T} interval of the measurement. The uncertainty based on different implementations of the material budget in MC ranges from 1.9% to 3.2%. Furthermore, the uncertainty to reflect the differences in the modeling of the detector response in MC and data is estimated by varying the selection criteria. A set of 22 different reasonable variations are used and the full analysis is repeated. The spread of the results in the different p_{T} bins is taken as uncertainty (9.8% to 18.7%). The investigation of possible biases due to the decision to parameterize the signal with a crystal ball function did not lead to additional

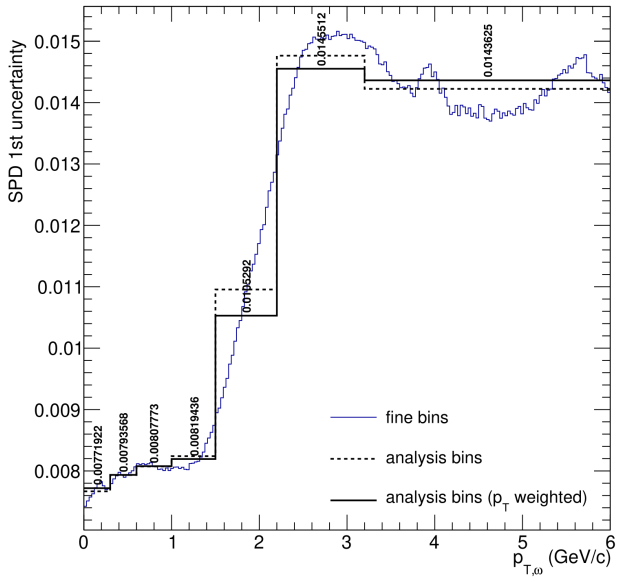

Figure 5.29: Systematic uncertainty on the ω measurement related to the imperfect description of the hit in the first layer of the SPD in MC simulations.

uncertainty.
The different systematic uncertainties are then added quadratically assuming no correlation between them. All uncertainties and the total sum for each p_{T} bin are summarised again in Table 14. Here, the uncertainties of the cross-sections ($\sigma_{\mathrm{MB}} = 50.87 \pm 0.04$ mb and $\sigma_{\mathrm{inel}} = 67.6 \pm 0.6$ mb) are summarized in the table as a combined uncertainty but are propagated separately to the total systematic uncertainties by the quadratic sum. In Figure 5.30 the corrected ω yield in inelastic pp collisions at $\sqrt{s} = 5.02$ TeV is shown with all systematic uncertainties listed in Table 14. In the lower pad, the relative systematic uncertainties are shown for all contributions (blue), the two main contributors signal extraction/background estimation (black), and MC to data matching/via the variations of selection criteria (red). Additionally, the relative statistic uncertainties are shown in gray. In the low and higher p_{T} ranges the statistical uncertainties are larger than the systematics. In the p_{T} between (1 - 3) GeV/c, both statistical and systematic uncertainties are similar.

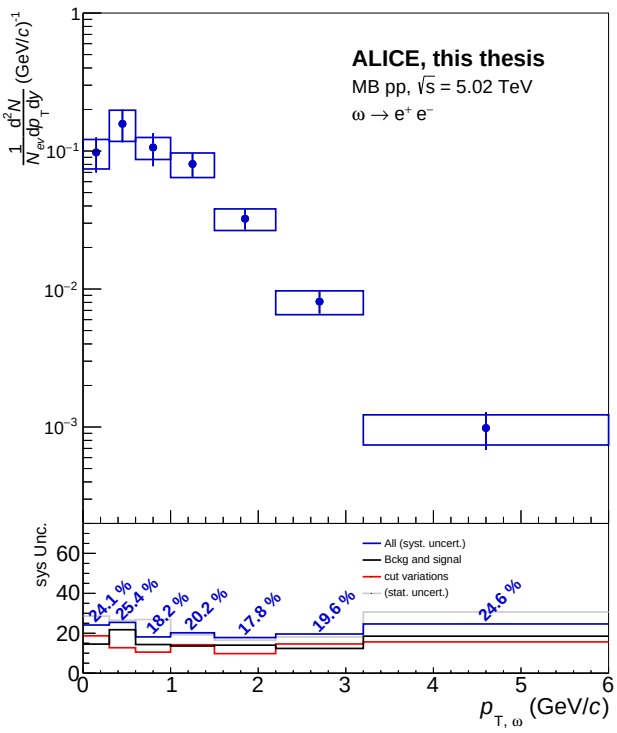

Figure 5.30: Corrected ω yield in inelastic pp collisions at $\sqrt{s} = 5.02$ TeV with all systematic uncertainties listed in Table 14. In the lower pad, the percentage of the systematic uncertainties is shown for each bin. The contributions of the systematic uncertainties for the selection criterion variations (red line), as well as the signal extraction (black line), are shown per p_{T} bin. The statistical uncertainties are shown in comparison in gray.

p_{T} [GeV/c]	signal extraction	material budget	selection criterion variation	ITS-TPC matching	SPD 1st	bin counting	cross sections	sum
$0.0 - 0.3$	14.6%	2.9%	18.7%	1.4%	0.8%	3.0%	0.9%	24.1%
$0.3 - 0.6$	21.8%	2.2%	12.7%	1.4%	0.8%	2.0%	0.9%	25.5%
$0.6 - 1.0$	14.3%	2.6%	10.5%	1.4%	0.8%	2.0%	0.9%	18.2%
$1.0 - 1.5$	13.6%	3.2%	14.2%	1.4%	0.8%	3.0%	0.9%	20.2%
$1.5 - 2.2$	14.0%	2.6%	9.8%	1.4%	1.1%	4.0%	0.9%	17.9%
$2.2 - 3.2$	12.4%	2.0%	14.6%	1.7%	1.5%	3.0%	0.9%	19.6%
$3.2 - 6.0$	18.5%	1.9%	15.7%	2.2%	1.4%	3.0%	0.9%	24.7%

Table 14: Summary of systematic uncertainties of the $\omega \to \mathrm{e}^+\mathrm{e}^-$ measurement in inelastic pp collisions at $\sqrt{s} = 5.02$ TeV. Here the uncertainties of the uncertainties of the cross-sections ($\sigma_{\mathrm{MB}} = 50.87 \pm 0.04$ mb and $\sigma_{\mathrm{inel}} = 67.6 \pm 0.6$ mb) are propagated separately. The 0.9% are for reference.

6 Results

In Figure 6.1 the final spectrum of the fully corrected ω yield in inelastic pp collisions at $\sqrt{s} = 5.02$ TeV is compared to the preliminary ω measurement reconstructed in the $\omega \to \pi^+\pi^-\pi^0$ decay channel [6], as well as to the PYTHIA Monash prediction [37]. Here one can see, that the PYTHIA overpredicts the ω yield, especially in the low p_{T} range, which is the focus of this thesis.

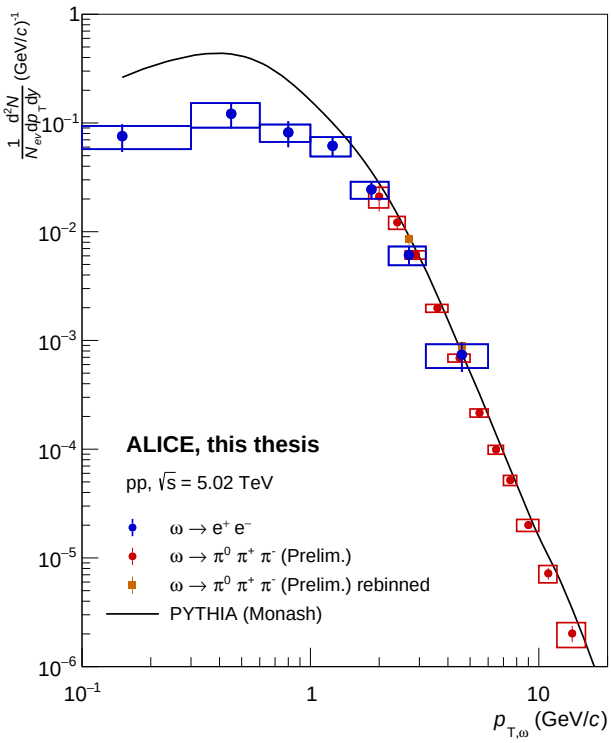

Figure 6.1: Measured ω yield in inelastic pp collisions at $\sqrt{s} = 5.02$ TeV via the decay channel $\omega \to \mathrm{e}^+\mathrm{e}^-$ (this analysis) and $\omega \to \pi^+\pi^-\pi^0$ (preliminary results) [6].

In the overlap region of $(2.2 < p_{\mathrm{T}} < 6)$ GeV/c the complementary measurement is rebinned to the same binning as in this analysis, shown as orange markers. The integral in the overlap region is calculated for both measurements. The result with the statistical and systematic uncertainties is listed in Table 15.

$\omega \to \mathrm{e}^+\mathrm{e}^-$	$10.86 \times 10^{-3} \pm 1.70 \times 10^{-3}(\mathrm{stat.}) \pm 2.27 \times 10^{-3}(\mathrm{sys.})$
$\omega \to \pi^+\pi^-\pi^0$	$14.47 \times 10^{-3} \pm 0.85 \times 10^{-3}(\mathrm{stat.}) \pm 1.56 \times 10^{-3}(\mathrm{sys.})$

Table 15: Comparison of measured yields within the overlap p_{T}-interval $2.2 - 6.0$ GeV/c.

To quantify the agreement between the two measurements, the difference between them divided by its uncertainty (σ) is calculated, assuming that the two analyses are uncorrelated. It amounts to about 1.08σ, so both measurements are in good agreement within their uncertainties.

To construct the ω/π ratio the charged pion spectra measured in pp collisions at $\sqrt{s} = 5.02$ TeV by ALICE [38] are used. Since the $\pi^{\pm}$ is only measured down to 0.1 GeV/c an

extrapolation to $p_{\mathrm{T}} = 0$ is needed. This is done by the parameterization of the full spectrum with a Lévy-Tsallis function. The integration down to $p_{\mathrm{T}} = 0$ takes the missing 0.1 GeV/c into account. For the ratio the $\pi^{\pm}$ measurement is used and only for p_{T} below 0.1 GeV/c the parameterization with the Lévy-Tsallis function is utilized.

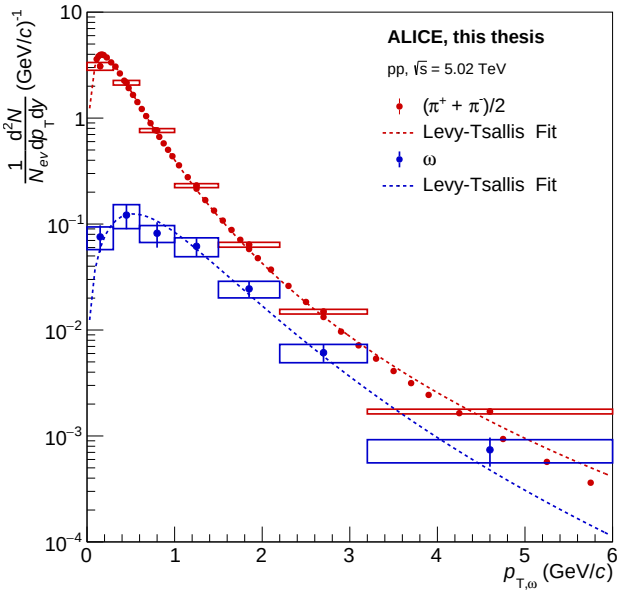

Figure 6.2: Measurements of ω (this thesis) and charged pions by the ALICE collaboration [38] parameterized with a Lévy-Tsallis function.

The charged pion spectrum, in the fine (published) binning as well as in the binning of this analysis, is shown in Figure 6.2 together with the measured ω spectrum. Both are shown with parameterizations based on the Lévy-Tsallis function.

The ratio of both spectra ($\omega/\pi^{\pm}$) is shown in Figure 6.3, the results of this thesis as blue markers. To evaluate the systematic uncertainties, the data points were shifted up and down coherently within their systematic uncertainties. The uncertainties on the ω and $\pi^{\pm}$ measurements are assumed to be uncorrelated.

Further comparisons of the ω/π ratio to different measurements are shown in Figure 6.3. The ratio is compared to preliminary results of the ω/π^0 ratio in pp collisions (red diamond markers) and p–Pb collisions (orange cross markers) at $\sqrt{s_{NN}} = 5.02$ TeV. Here can be seen, that the ratio of the ω/π^0 ratios are slightly above the dielectron measurement but within the uncertainties. In addition, published measurements of the ω/π^0 ratio in pp collisions at 7 TeV by ALICE are shown [5]. All the ALICE ω measurements were performed in the 3 pion channel and have a lower p_{T} threshold of about 2 GeV/c. Taking into account the statistical and systematic uncertainties as well as the difference between the pion baseline (ω to π^0 or $\pi^{\pm}$), the ALICE measurements are consistent, as shown in Figure 6.3. Moreover measurements in pp collisions at $\sqrt{s} = 200$ GeV performed by the PHENIX collaboration are shown. A tension of the here presented measurement at $\sqrt{s} = 5.02$ TeV with the PHENIX measurement at $\sqrt{s} = 200$ GeV can be observed below 2 GeV/c. Such tension is partially expected from PYTHIA simulations, which predict a slightly lower $\omega/\pi^{\pm}$ ratio at higher energies. Nevertheless, PYTHIA overestimates the $\omega/\pi^{\pm}$ ratio at low p_{T} at both energies. Finally, different implementations in the hadronisation mechanisms implemented in PYTHIA

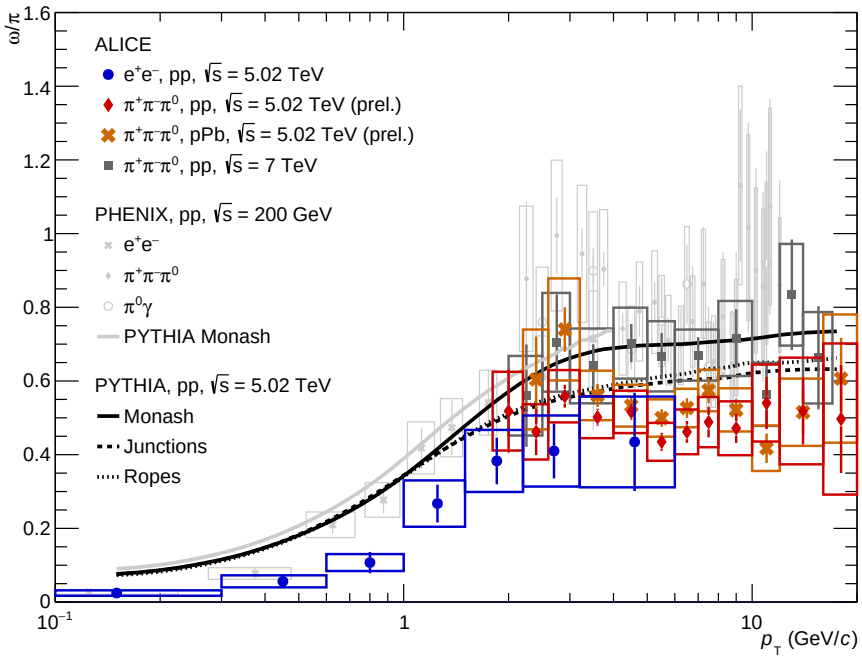

Figure 6.3: Ratio comparison with different implementations of PYTHIA [37] and ω/π^0 ratio measurement performed by the ALICE collaboration (pp, p–Pb at $\sqrt{s} = 5.02$ TeV ($\omega \to \pi^+\pi^-\pi^0$) [6] & pp at $\sqrt{s} = 7$ TeV ($\omega \to \pi^+\pi^-\pi^0$) [5]) and the PHENIX measurements at $\sqrt{s} = 200$ GeV ($\omega \to \mathrm{e}^+\mathrm{e}^-$, $\omega \to \pi^+\pi^-\pi^0$ and $\omega \to \pi^0\gamma$ [7]).

like the inclusion of ropes or junctions seem to only show effects at momenta above 2 GeV/c.

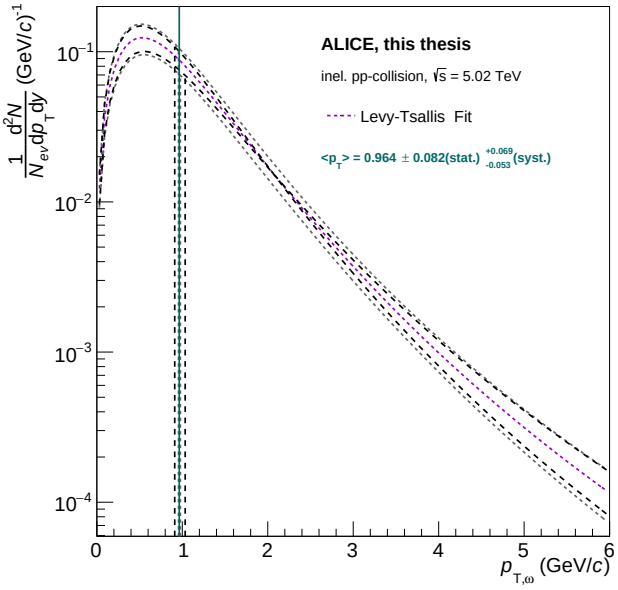

Figure 6.4: Lévy-Tsallis parameterizations to extract $\langle p_{\mathrm{T}} \rangle$ and systematic uncertainties. For detailed description see text.

To extract the mean p_{T} of the ω meson spectrum the parameterization of the spectrum with the Lévy-Tsallis function shown in Figure 6.4 is used. The value is calculated as

$$\langle p_{\mathrm{T}} \rangle = \frac{\int p_{\mathrm{T}} \times f(p_{\mathrm{T}}) dp_{\mathrm{T}}}{\int f(p_{\mathrm{T}}) dp_{\mathrm{T}}}. \tag{6.1}$$

To estimate the uncertainty of the extracted value the covariance matrix of the parameterization is used. The resulting value is $\langle p_{\mathrm{T}} \rangle = 0.964 \pm 0.082(\mathrm{stat.})^{+0.069}_{-0.053}(\mathrm{syst.})$. The systematic uncertainty is evaluated by shifting the data points within their uncertainties. In the case of a point-by-point correlated uncertainty, the data points are coherently shifted up and down, and in the case of an anti-correlation, the data points are shifted by a tilt from up to down, and from down to up over the p_{T} range $(0-6)$ GeV/c within their uncertainties to gain the maximum variation. In both cases, the same parameterisation is redone. The resulting set of functions is shown in Figure 6.4. The gray lines show the results of the point-by-point correlation and the black lines the result of anti-correlation.

The dashed purple line shows the default parameterisation, the dashed gray lines correspond to the assumption of fully correlated uncertainties between the p_{T}-bin, and the dashed black lines correspond to the anti-correlated uncertainties. In all cases the procedure to extract $\langle p_{\mathrm{T}} \rangle$ is repeated and the maximum variation is taken as the systematic uncertainty.

The yield at midrapidity is extracted by integrating the measured spectrum. As the measurement is performed down to $p_{\mathrm{T}} = 0$ no extrapolation downwards is needed. The systematic uncertainties in the data are propagated assuming a full point-to-point correlation as before done for the systematic uncertainty of the $\langle p_{\mathrm{T}} \rangle$, resulting in an integrated ω yield in inelastic pp collisions of $dN/dy = 0.148 \pm 0.016(\mathrm{stat.}) \pm 0.031(\mathrm{syst.})$ To estimate the yield above 6 GeV/c (last data point) the fraction of the integration of the Lévy-Tsallis parameterization above 6 GeV/c and overall was found to be $< 10^{-4}$. This fraction is assumed to be negligible given the uncertainties of the extracted yield at midrapidity. This can be compared to the integrated yield of charged pions as published in [38] $dN/dy_{\pi^+ + \pi^-} = 4.1342 \pm 0.0005(\mathrm{stat.}) \pm 0.3032(\mathrm{syst.})$.

7 Summary and outlook

The ω meson has been reconstructed in pp collisions at $\sqrt{s} = 5.02$ TeV via the dielectron decay channel using four different methods to estimate the background. For this, the unlike-sign as well as the like-sign spectrum are used. MC simulations are utilized to fix the shape of the ω signal and allows for the determination of the physical background (shape or fully normalized) using a cocktail of known hadronic sources.

The ω yield is extracted by bin counting using six different m_{ee} ranges. The default ω yield is chosen as the closest spectrum to the mean distribution of the 24 extracted ω yields. To correct for signal outside the signal ranges, the ω signal from MC simulations is used. For the fully corrected differential yield in inelastic pp collisions at $\sqrt{s} = 5.02$ TeV losses due to the detector acceptance and efficiency, to the minimum bias trigger requirements, as well as to the branching ratio of the used decay channel are taken into account. Systematic uncertainties, are raising mainly from the signal extraction (around $12.4\% - 21.8\%$), as well as an imperfect description of the tracking and PID in MC estimated by varying the selection criteria (around $9.8\% - 18.7\%$).
With this, a first fully corrected ω spectrum down to $p_{\mathrm{T}} = 0$ was reconstructed in this thesis for pp collisions at $\sqrt{s} = 5.02$ TeV.

The first measurement down to $p_{\mathrm{T}} = 0$ at LHC energies of ω and the $\omega/\pi^{\pm}$ ratio is finally presented. The results are compared to complementary measurements at higher p_{T} by the ALICE Collaboration, measurements down to $p_{\mathrm{T}} = 0$ at RHIC by the PHENIX Collaboration, and PYTHIA simulations. A hint for a smaller $\omega/\pi^{\pm}$ ratio for $p_{\mathrm{T}} < 2$ GeV/c at LHC compared to RHIC energies is observed and qualitatively expected from the calculations, due to feed-down pions. Nevertheless, PYTHIA overestimates the $\omega/\pi^{\pm}$ ratio at low p_{T} at both energies.

To improve the precision of this measurement, increased statistics are essential. A significantly larger data set has recently been collected by the upgraded ALICE detector. This will allow for a ω yield extraction with smaller uncertainties on both the yield and the ω/π ratio. Due to the larger statistics, a p_{T} reach higher than 6 GeV/c will be possible, therefore the overlap with the $\omega \to \pi^{+}\pi^{-}\pi^{0}$ measurements will be larger and makes a wider comparison of the measurements possible. The study of multiplicity dependence, system size dependence, and more differential studies (e.g. elliptic flow) will be enabled. Smaller systematic uncertainties due to better charm rejection using DCA information will be possible.
The methods introduced in this thesis to extract the ω yield will be beneficial for future measurements.

A Appendix

A.1 Dataset & Selection Criteria - Detail

The in this analysis used list of runs that is declared as good for electron identification by the data preparation group are following the run numbers:

282343, 282342, 282341, 282340, 282314, 282313, 282312, 282309, 282307, 282306, 282305, 282304, 282303, 282302, 282247, 282230, 282229, 282227, 282224, 282206, 282189, 282147, 282146, 282127, 282126, 282125, 282123, 282122, 282120, 282119, 282118, 282099, 282098, 282078, 282051, 282050, 282031, 282025, 282021, 282016, 282008.

Cut variations for Monte Carlo data matching

Cut	Nb_{ITScls}	χ^2_{ITS}	$\mathrm{Nb}^{TPC}_{cros.rows}$	$\frac{Nb^{\mathrm{TPC}}_{\mathrm{Cross.R.}}}{Nb^{\mathrm{TPC}}_{\mathrm{findablecls.}}}$	shared TPC cls. frac.	χ^2_{TPC}	$n^{TOF}_{\sigma_e}$	$n^{TPC}_{\sigma_e}$	$n^{TPC}_{\sigma_\pi}$	$n^{TPC}_{\sigma_K}$	$n^{TPC}_{\sigma_p}$
1	3	5.5	100	0.6	0.4	4	3	3	3.5	-3–3	-3–3
2	2	4.5	120	0.6	0.4	3	2	3	3.5	-2.5–3.5	-2.5–3.5
3	3	6.5	120	0.6	0.4	3	2	3	3.5	-3–3	-2.5–3.5
4	2	6.5	100	0.7	0.4	3	2	3	4.0	-2.5–3.5	-3–3
5	3	4.5	120	0.5	0.4	4	3	3	4.0	-3–3	-2.5–3.5
6	3	6.5	140	0.7	0.4	3	2	3	4.0	-3–3	-3–3
7	2	5.5	140	0.7	0.4	5	3	3	3.5	-3–3	-2.5–3.5
8	3	5.5	120	0.6	0.4	4	2	3	3.5	-3–3	-3–3
9	3	4.5	140	0.6	0.4	3	3	3	3.0	-3.5–2.5	-2.5–3.5
10	3	5.5	140	0.7	0.4	4	3	3	3.5	-3.5–2.5	-2.5–3.5
11	3	6.5	140	0.6	0.6	5	3	2.5	3.0	-3–3	-3.5–2.5
12	3	6.5	100	0.7	0.6	5	2	2.5	4.0	-3–3	-2.5–3.5
13	2	5.5	120	0.5	0.6	4	2	2.5	3.5	-3.5–2.5	-3–3
14	2	6.5	140	0.6	0.6	5	3	2.5	3.0	-2.5–3.5	-3–3
15	2	6.5	140	0.7	0.6	4	2	2.5	4.0	-3.5–2.5	-3–3
16	2	5.5	140	0.6	0.8	5	2	3.5	3.5	-3.5–2.5	-3.5–2.5
17	2	6.5	140	0.7	0.8	5	2	3.5	4.0	-2.5–3.5	-2.5–3.5
18	3	6.5	100	0.5	0.8	3	3	3.5	4.0	-3.5–2.5	-3.5–2.5
19	3	4.5	100	0.7	0.8	5	3	3.5	3.0	-2.5–3.5	-3.5–2.5
20	2	4.5	120	0.6	0.8	5	2	3.5	3.0	-3.5–2.5	-3.5–2.5
21	3	6.5	100	0.7	0.8	4	2	3.5	4.0	-3–3	-3–3
22	3	6.5	100	0.6	0.8	5	2	3.5	3.0	-3.5–2.5	-3–3

Figure A.1: 22 cut variations to estimate the systematic uncertainties for the cut settings [22].

A.2 Signal shape - additional figures

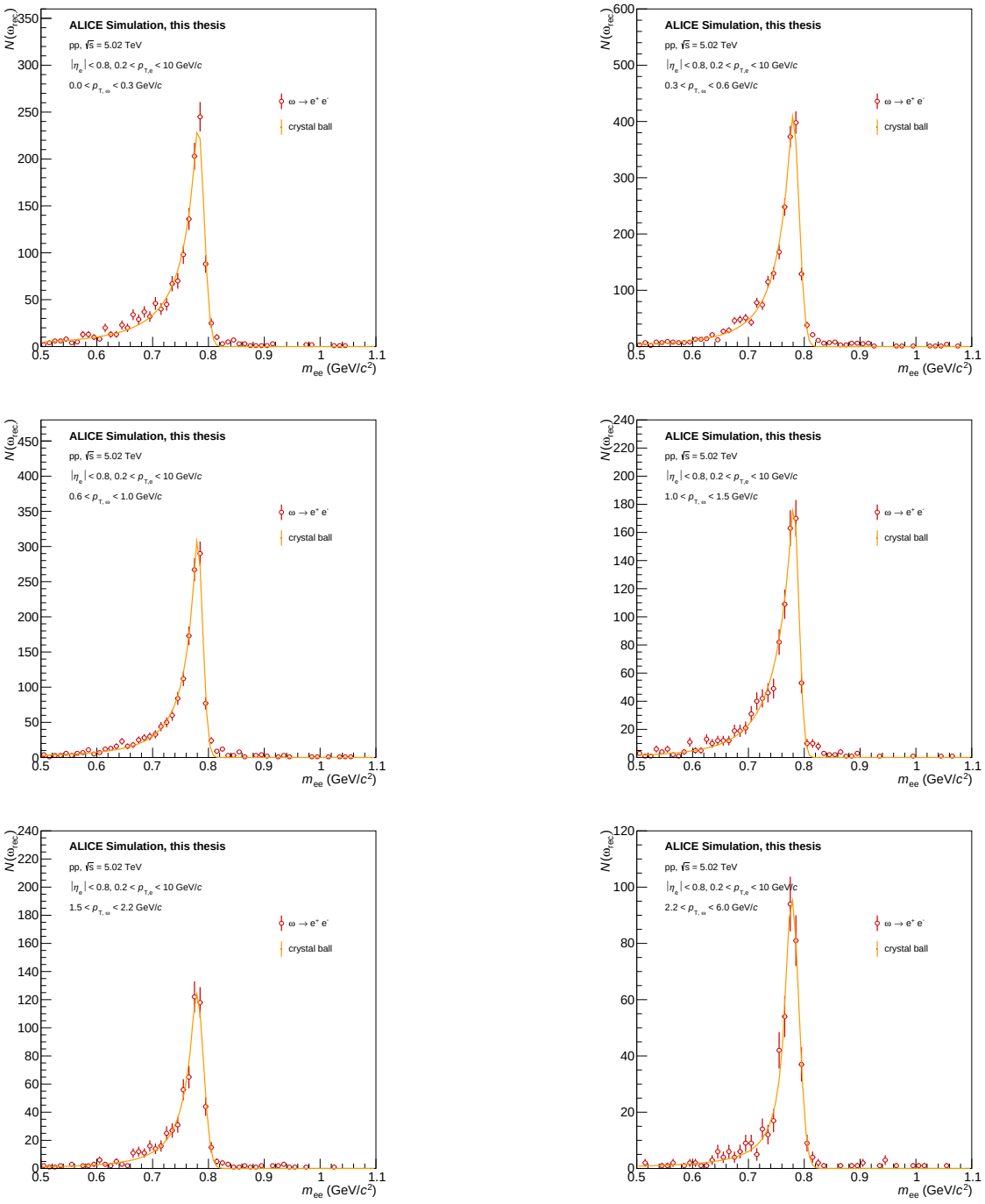

Figure A.2: Reconstructed ω signal in MC after fiducial and track selections described by a CB function for six p_{T} slices.

A.3 Background estimation - additional figures

cocktail templates

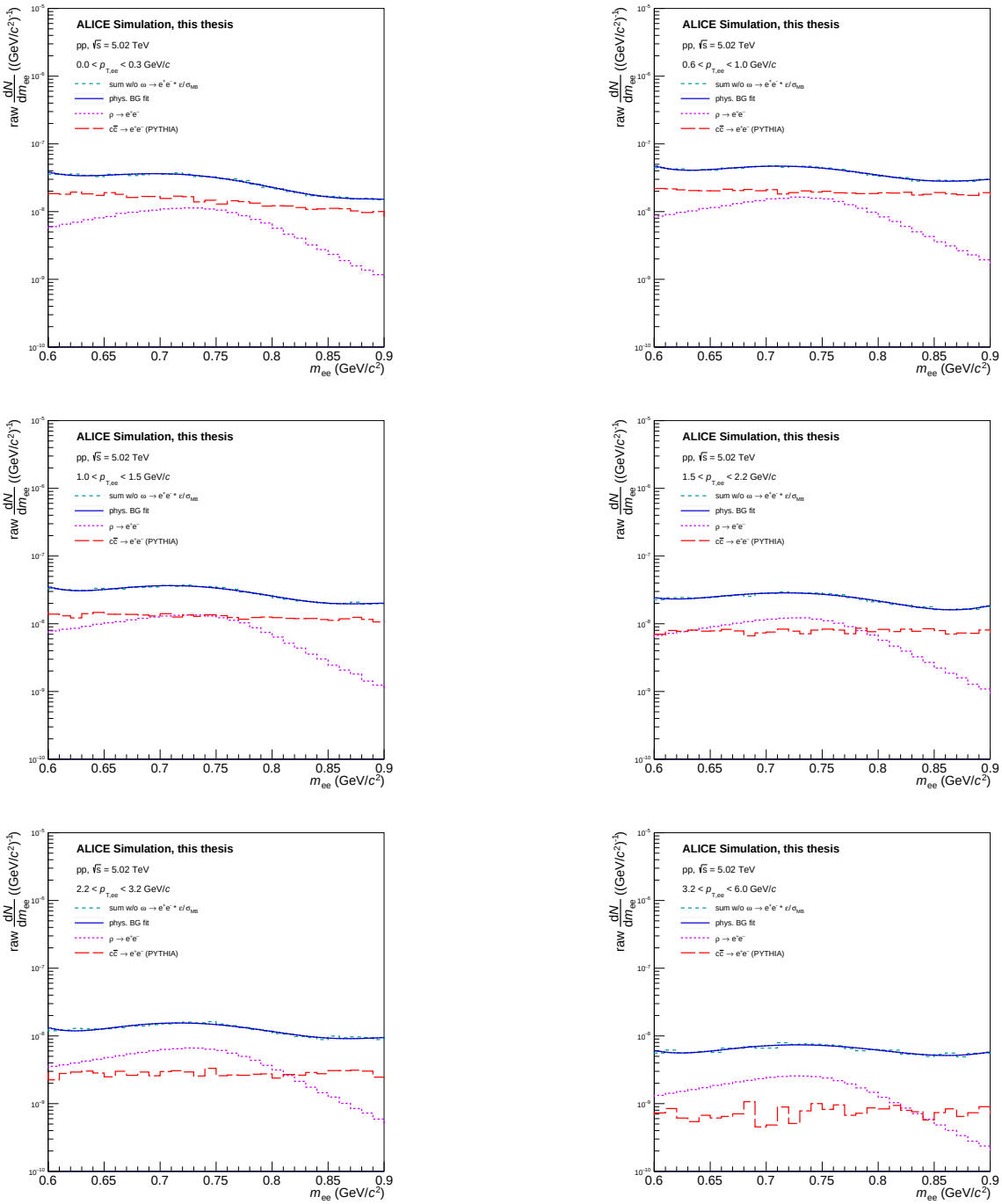

Figure A.3: Cocktail templates `pol5` fits, as the blue solid lines, for the background estimation of method 2a) and 2b) by the fit of the cocktail sum without the ω signal shown in Fig. 5.5 corrected by an efficiency map and the minimum bias cross section ($\sigma_{MB} = 50.87 \pm 0.04$ mb) [32]) to be comparable to the data. Two main contributors to the physical background are shown as well $c\bar{c}$(red line) and ρ (purple line).

Method 1 - ULS

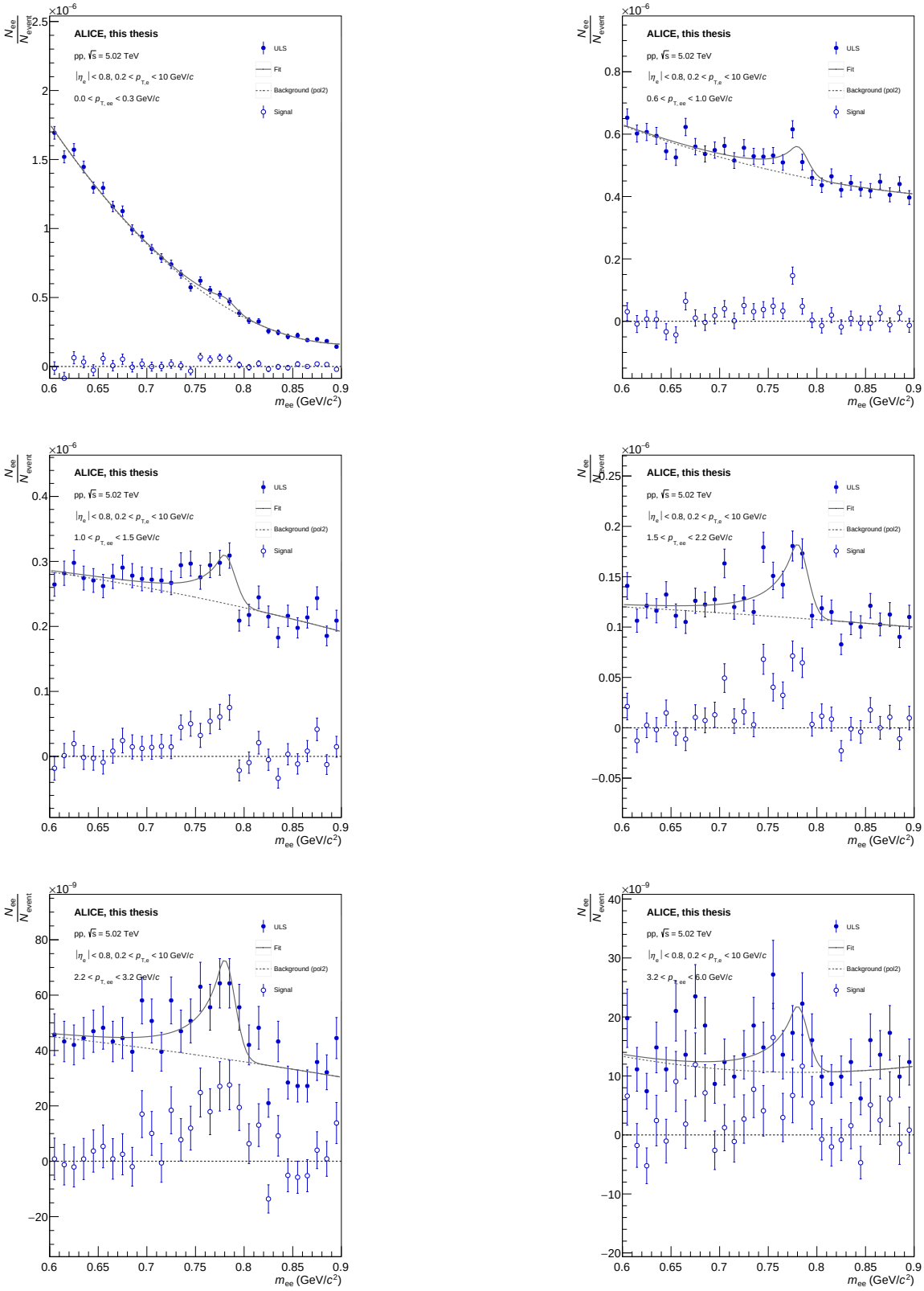

Figure A.4: ULS - method for the remaining p_{T} bins: the solid gray line is the combined (Background+Signal) fit to the ULS, the dashed line (background) is then subtracted from the ULS resulting in the signal (blue open markers)

Method 2 - LS: Step 1

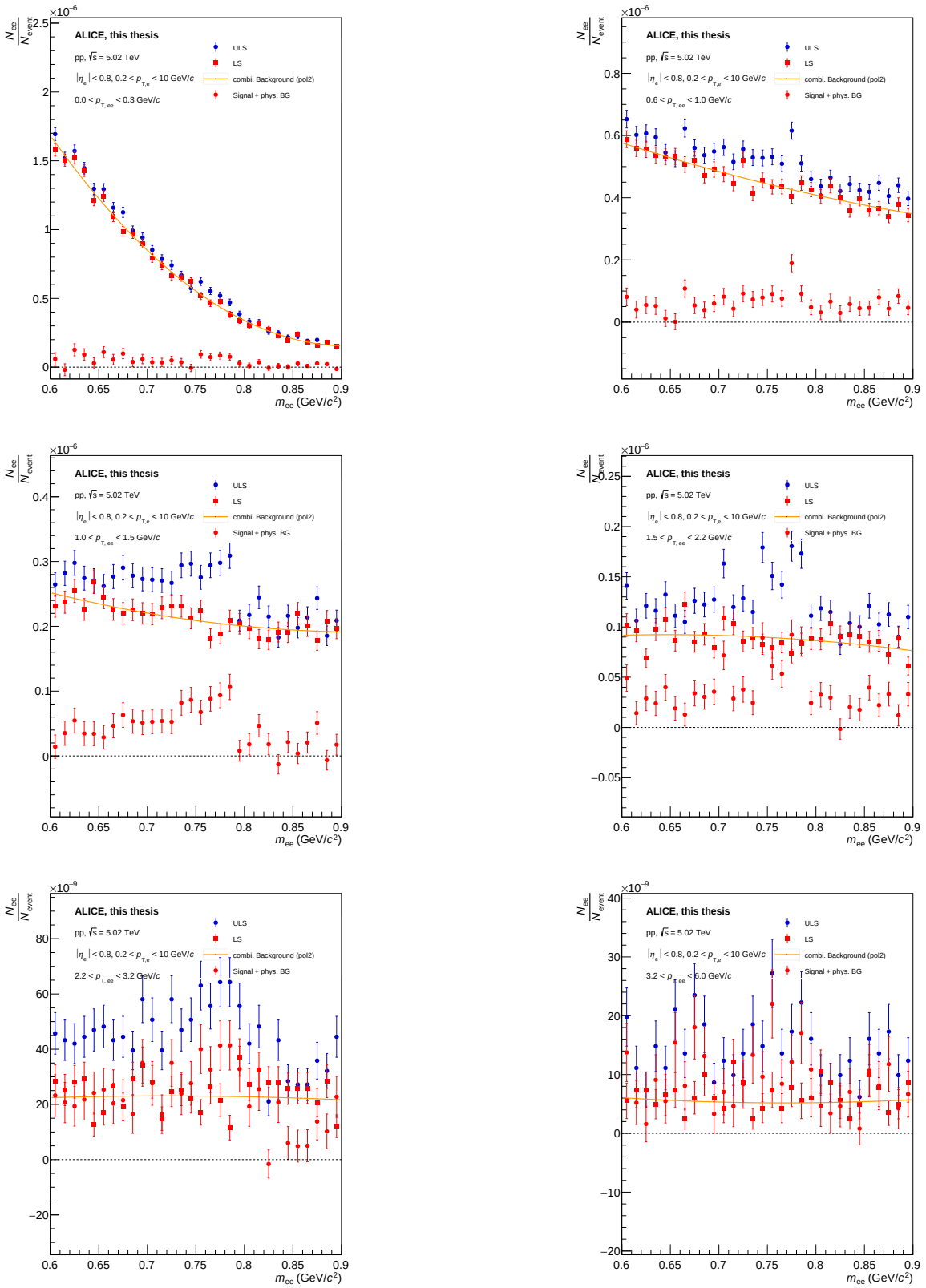

Figure A.5: 1st step LS - method for the remaining p_{T} bins: the solid orange line is the combinatorial background fit to the LS(red, full markers), which is then subtracted from the ULS resulting in the physical background + signal (red open markers)

R_{acc} factor

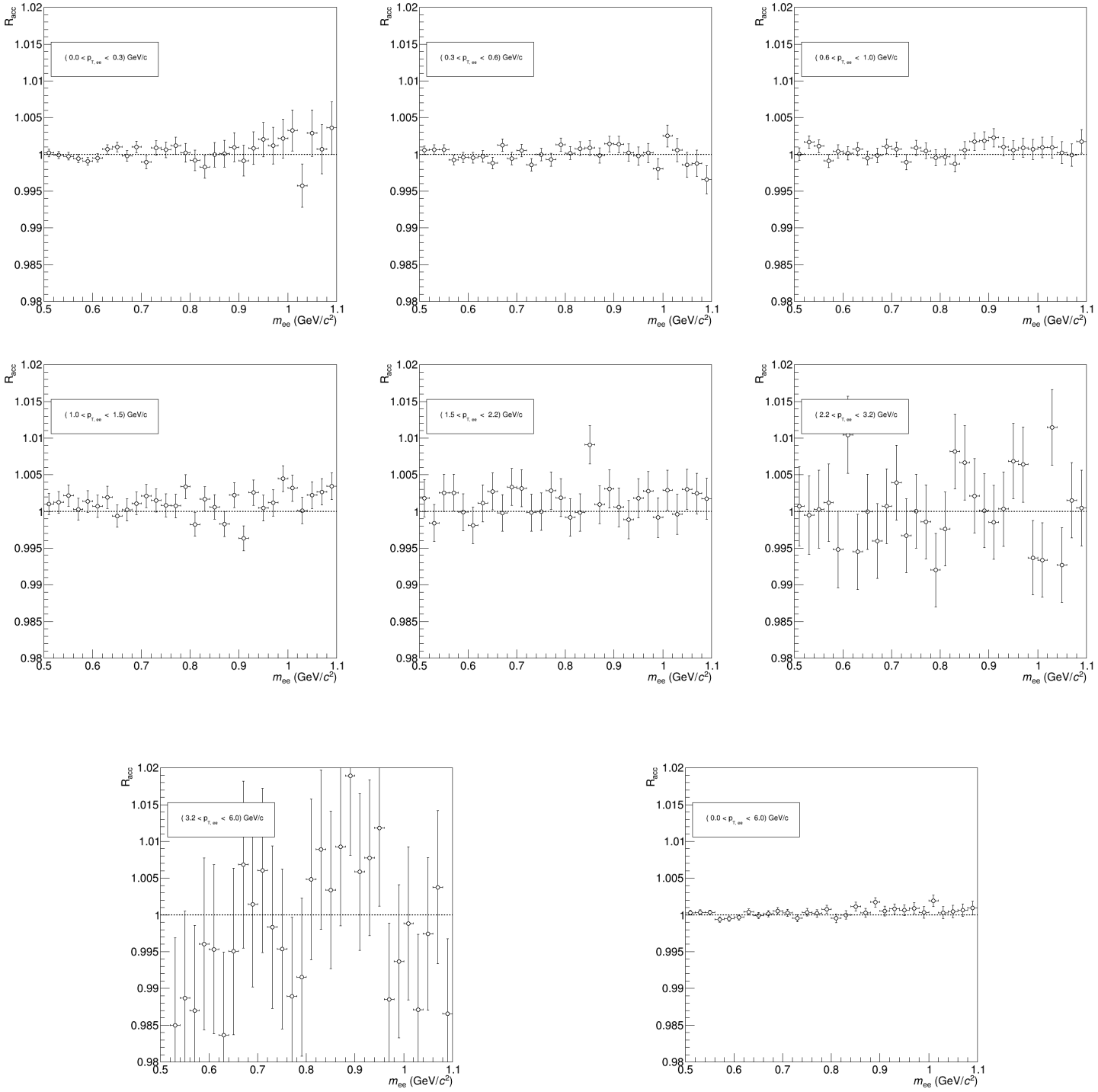

Figure A.6: R_{acc} factor for the single p_{T} intervals as well as the whole integrated p_{T} range of $(0-6)\mathrm{GeV}/c$.

Method 2 - LS: Step 2

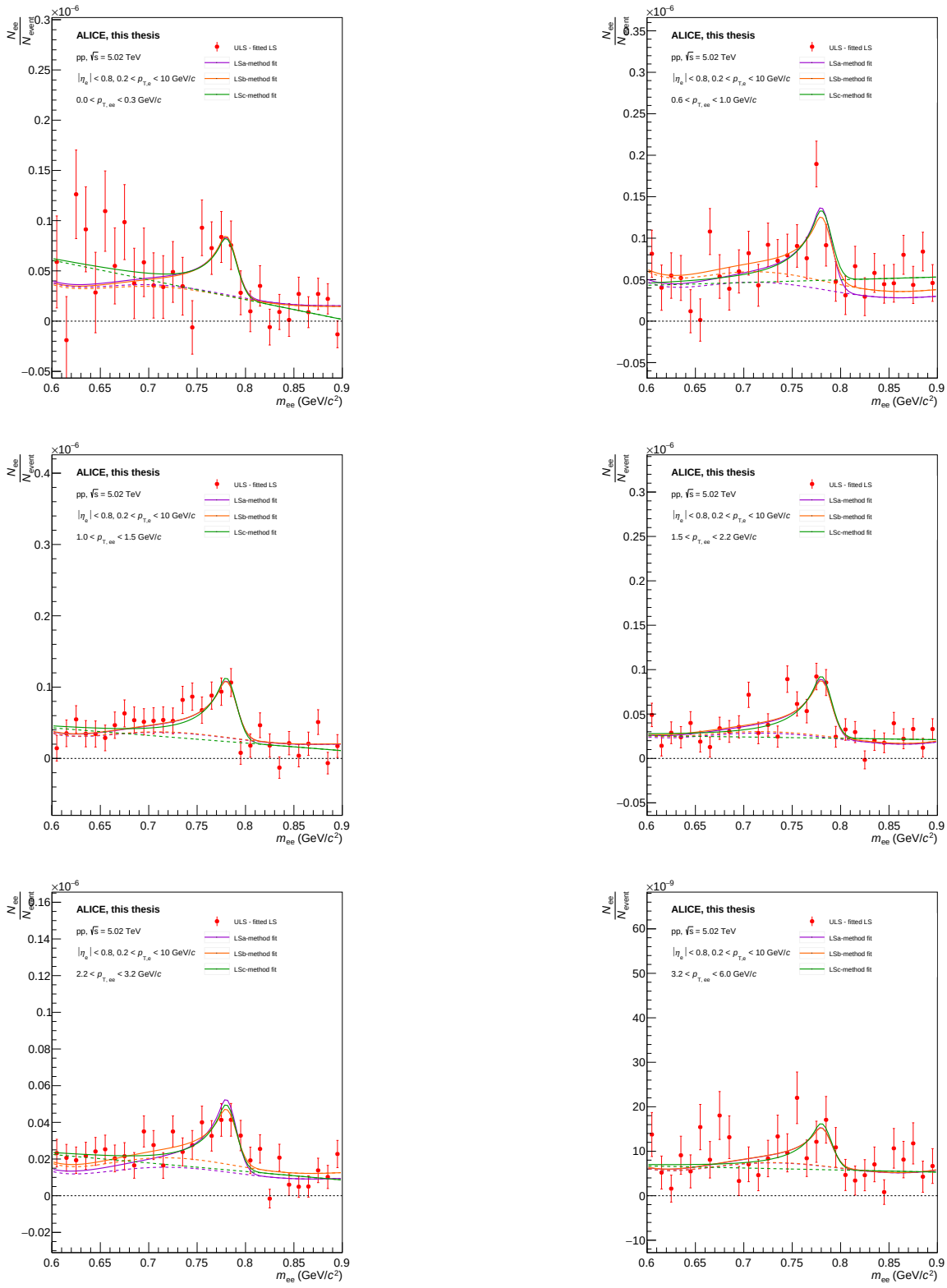

Figure A.7: 2nd step of the LS - methods for the remaining p_{T} bins: the three solid lines are the combined (physical background+signal) fits (purple: cocktail template + CB; orange: cocktail template with parameterization + CB; green: constant polynomial + CB) of the subtracted ULS in Fig. 5.4. The dashed lines show the physical background that is still underneath the ω signal.

ω Signal

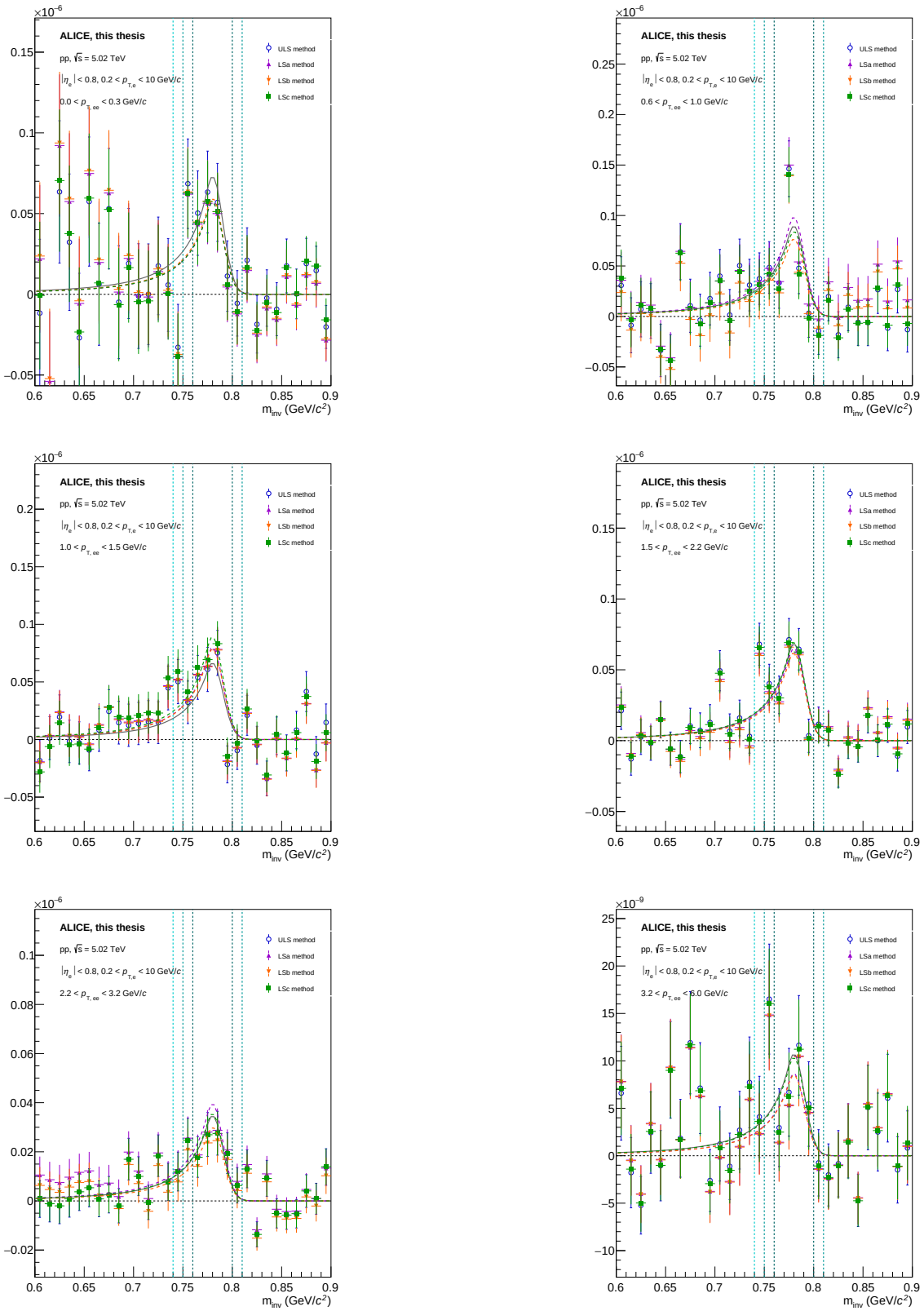

Figure A.8: Resulting ω signal for each p_{T} bin for all four methods, each with an associated crystal ball function. Bin counting ranges are indicated as vertical dashed lines.

A.4 Systematic uncertainties - additional figures

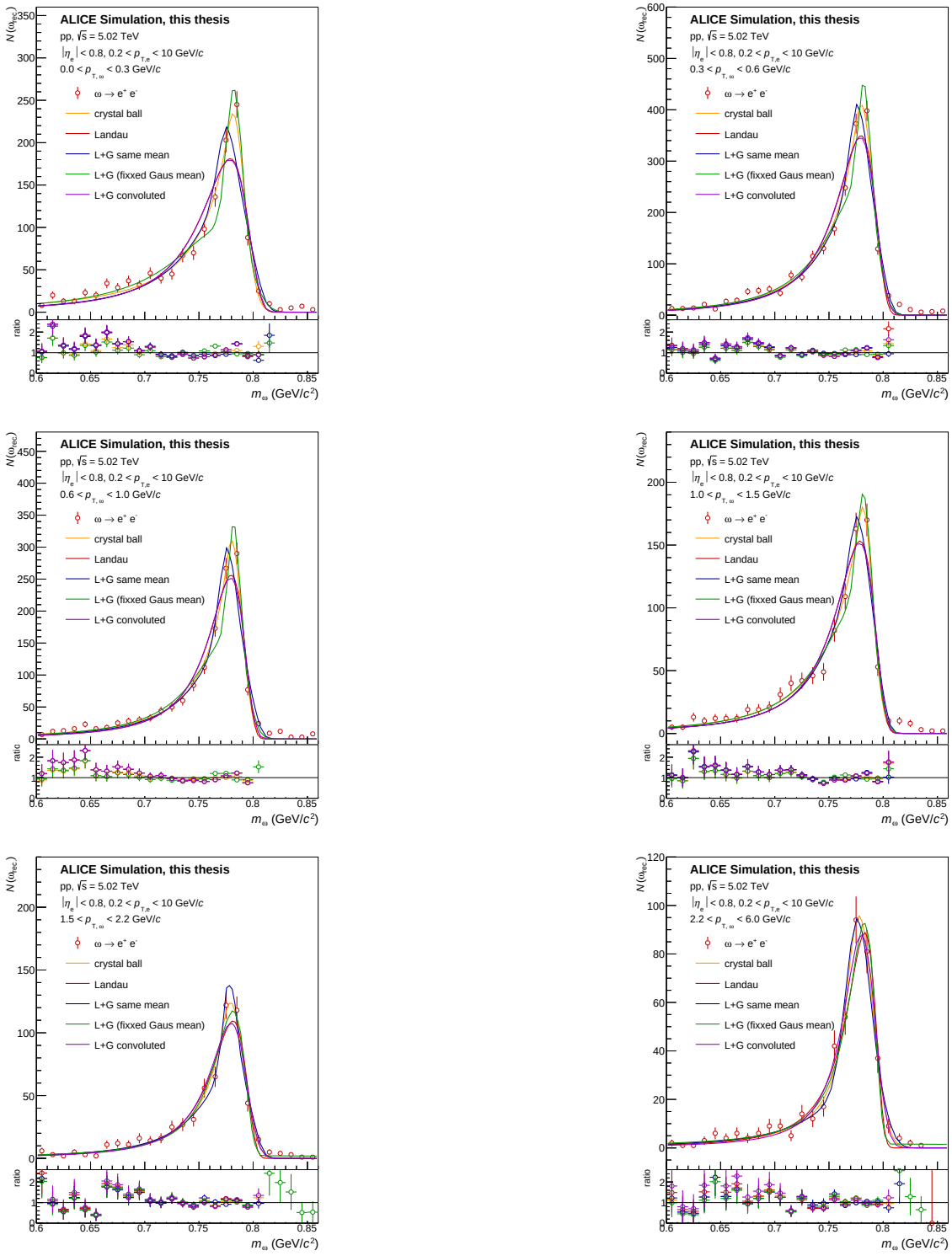

Figure A.9: Reconstructed ω signal in MC data after fiducial and track selections for six p_{T} slices, described by alternative functions for the CB: Landau (red), Landau+Gaussian same mean (blue), Landau+Gaussian fixed Gaussian mean (green) and Landau Gaussian convoluted (purple). Same color code for the ratio of data/fit.

References

[1] A. Rubbia, *Phenomenology of Particle Physics*. Cambridge University Press, 2022.

[2] H. Schopper, *Particle Physics Reference Library: Volume 1: Theory and Experiments*. Cham: Springer Nature, 2020. https://doi.org/10.1007/978-3-030-38207-0.

[3] R. L. Workman *et al.*, "Review of Particle Physics," *PTEP*, vol. 2022, p. 083C01, 2022. https://doi.org/10.1093/ptep/ptac097.

[4] "Meson baryon multiplets." https://tikz.net/sm_isospin/, Jun 2024.

[5] S. Acharya *et al.*, "Production of ω mesons in pp collisions at $\sqrt{\mathbf{s}} = \mathbf{7}$ TeV," *Eur. Phys. J. C*, vol. 80, no. 12, p. 1130, 2020. https://doi.org/10.1140/epjc/s10052-020-08651-y.

[6] N. Strangmann, "Measurement of ω meson production in pp and p–Pb collisions at $\sqrt{s_{\mathrm{NN}}}$ = 5.02 TeV with ALICE," *PoS*, vol. HardProbes2023, p. 195, 2024. https://doi.org/10.22323/1.438.0195.

[7] A. Adare *et al.*, "Measurement of neutral mesons in p+p collisions at $\sqrt{s}$= 200 GeV and scaling properties of hadron production," *Phys. Rev. D*, vol. 83, p. 052004, 2011. https://doi.org/10.1103/PhysRevD.83.052004.

[8] H. S. Scheid, "Low-mass dielectron measurements in pp, p-Pb, and Pb-Pb collisions with ALICE at the LHC," *Nucl. Phys. A*, vol. 1005, p. 121852, 2021.

[9] ALICE, "ALICE Experiment - CERN Alice." https://alice.cern/.

[10] A. Figure. https://alice-figure.web.cern.ch/system/files/figures/General/atauro/2017-May-11-ALICE_RUN2_HD.png, 11 2017.

[11] K. Aamodt *et al.*, "The ALICE experiment at the CERN LHC," *JINST*, vol. 3, p. S08002, 2008. https://doi.org/10.1088/1748-0221/3/08/S08002.

[12] E. Botta, "ALICE ITS: Operational Experience, Performance and Lessons Learned," *PoS*, vol. Vertex2019, p. 002, 2020. https://doi.org/10.22323/1.373.0002.

[13] P. Kuijer, "The inner tracking system of the ALICE experiment," *Nucl. Instrum. Meth. A*, vol. 530, pp. 28–32, 2004. https://doi.org/10.1016/j.nima.2004.05.042.

[14] M. M. F. P. E. Bruna, A. Dainese, "Vertex reconstruction for proton-proton collisions in ALICE." https://cds.cern.ch/record/1225497/files/notavert_v15_final.pdf, 2009.

[15] B. B. Abelev *et al.*, "Performance of the ALICE Experiment at the CERN LHC," *Int. J. Mod. Phys. A*, vol. 29, p. 1430044, 2014. https://doi.org/10.1142/S0217751X14300440.

[16] C. Lippmann, "Particle identification," *Nucl. Instrum. Meth. A*, vol. 666, pp. 148–172, 2012. https://doi.org/10.1016/j.nima.2011.03.009.

[17] J. Alme *et al.*, "The ALICE TPC, a large 3-dimensional tracking device with fast readout for ultra-high multiplicity events," *Nucl. Instrum. Meth. A*, vol. 622, pp. 316–367, 2010. https://doi.org/10.1016/j.nima.2010.04.042.

[18] J. Wiechula, "Commissioning and Calibration of the ALICE TPC," *Nucl. Phys. A*, vol. 830, pp. 531C–534C, 2009. https://doi.org/10.1016/j.nuclphysa.2009.10.046.

[19] Francesco Barile, ALICE Collaboration, "Distribution of dE/dx as a function of momentum in the TPC (pp collisions at sqrt(s) = 7 TeV)." "{https://alice-figure.web.cern.ch/node/7764}".

[20] "TOF Beta vs Momentum performance in pp at 5.02 TeV (LHC15n)." https://alice-figure.web.cern.ch/node/11822, 7 2017.

[21] Y. Zoccarato *et al.*, "Front end electronics and first results of the ALICE V0 detector," *Nucl. Instrum. Meth. A*, vol. 626-627, pp. 90–96, 2011. https://doi.org/10.1016/j.nima.2010.10.025.

[22] S. Acharya *et al.*, "Dielectron production in proton-proton and proton-lead collisions at $\sqrt{s_{NN}} = 5.02$ TeV," *Phys. Rev. C*, vol. 102, no. 5, p. 055204, 2020. https://doi.org/10.1103/PhysRevC.102.055204.

[23] T. Sjostrand, S. Mrenna, and P. Z. Skands, "A Brief Introduction to PYTHIA 8.1," *Comput. Phys. Commun.*, vol. 178, pp. 852–867, 2008. https://doi.org/10.1016/j.cpc.2008.01.036.

[24] R. Brun, R. Hagelberg, M. Hansroul, and J. C. Lassalle, *Simulation program for particle physics experiments, GEANT: user guide and reference manual*. Geneva: CERN, 1978. https://cds.cern.ch/record/118715.

[25] D. Leermakers, "Systematic study of track quality cuts at ALICE," 2015. https://cds.cern.ch/record/2045797.

[26] Wikipedia contributors, "Crystal ball function — Wikipedia, the free encyclopedia." https://en.wikipedia.org/w/index.php?title=Crystal_Ball_function&oldid=990932753, 2020. [Online; accessed 18-August-2024].

[27] F. Geurts and R.-A. Tripolt, "Electromagnetic probes: Theory and experiment," *Progress in Particle and Nuclear Physics*, vol. 128, p. 104004, 2023. https://doi.org/10.1016/j.ppnp.2022.104004.

[28] S. Acharya *et al.*, "Dielectron production in proton-proton collisions at $\sqrt{s} = 7$ TeV," *JHEP*, vol. 09, p. 064, 2018. https://doi.org/10.1007/JHEP09(2018)064.

[29] A. Adare *et al.*, "Detailed measurement of the e^+e^- pair continuum in $p+p$ and Au+Au collisions at $\sqrt{s_{NN}} = 200$ GeV and implications for direct photon production," *Phys. Rev. C*, vol. 81, p. 034911, 2010. https://doi.org/10.1103/PhysRevC.81.034911.

[30] R. Arnaldi *et al.*, "Precision study of the $\eta \to \mu^+\mu^-\gamma$ and $\omega \to \mu^+\mu^-\pi^0$ electromagnetic transition form-factors and of the $\rho \to \mu^+\mu^-$ line shape in NA60," *Phys. Lett. B*, vol. 757, pp. 437–444, 2016. https://doi.org/10.1016/j.physletb.2016.04.013.

[31] S. Acharya *et al.*, "Evidence of rescattering effect in Pb-Pb collisions at the LHC through production of $K^*(892)^0$ and $\phi(1020)$ mesons," *Phys. Lett. B*, vol. 802, p. 135225, 2020.

[32] "ALICE 2017 luminosity determination for pp collisions at $\sqrt{s} = 5$ TeV," 2018. https://cds.cern.ch/record/2648933.

[33] C. Loizides, J. Kamin, and D. d'Enterria, "Improved Monte Carlo Glauber predictions at present and future nuclear colliders," *Phys. Rev. C*, vol. 97, no. 5, p. 054910, 2018. https://doi.org/10.1103/PhysRevC.97.054910.

[34] R. Barlow and C. Beeston, "Fitting using finite monte carlo samples," *Computer Physics Communications*, vol. 77, no. 2, pp. 219–228, 1993. https://doi.org/10.1016/0010-4655(93)90005-W.

[35] S. Acharya *et al.*, "Data-driven precision determination of the material budget in ALICE," *JINST*, vol. 18, no. 11, p. P11032, 2023. https://doi.org/10.1088/1748-0221/18/11/P11032.

[36] ALICE - Data Preparation Group, "DPG - Analysis Object Tools - Systematic uncertainties on TPC-ITS matching in various Run-2 data samples." https://twiki.cern.ch/twiki/bin/genpdfauth/ALICE/AliDPGtoolsTrackSystematicUncertaintyBookkeping, 2021.

[37] C. Bierlich *et al.*, "A comprehensive guide to the physics and usage of PYTHIA 8.3," *SciPost Phys. Codeb.*, vol. 2022, p. 8, 2022.

[38] S. Acharya *et al.*, "Production of charged pions, kaons, and (anti-)protons in Pb-Pb and inelastic *pp* collisions at $\sqrt{s_{NN}} = 5.02$ TeV," *Phys. Rev. C*, vol. 101, no. 4, p. 044907, 2020.

Danksagung

Zuallererst möchte ich Herrn Professor Dr. Harald Appelshäuser für seine Unterstützung und die Möglichkeit danken, meine Masterarbeit in der Frankfurter ALICE-Arbeitsgruppe schreiben zu können.

Frau Dr. Raphaelle Bailhache möchte ich ebenfalls für ihre stetige Unterstützung und Hilfe danken, auch zu Zeiten, die nicht selbstverständlich waren.

Sebastian Scheid und Jerome Jung danke ich für die Betreuung, die es mir ermöglicht hat, Lösungen für die Herausforderungen des Masterthemas zu finden. Vielen Dank für die zahlreiche Hilfe und die Unterstützung.

Ich danke der Arbeitsgruppe vorallem auch für die moralische Unterstützung bei der Vorbereitung einiger Präsentationen.

Ich danke meiner Familie für ihre Unterstützung in jeglicher Hinsicht, ohne die mein Studium nur schwer möglich gewesen wäre.

Danke auch an meine Freunde, die sich immer Zeit für mich genommen haben und mir mit Rat und Kaffee zur Seite standen.

Statutory Declaration / Ehrenwörtliche Erklärung

I hereby declare that I have written this thesis independently and without the use of sources or aids other than those indicated. All passages in the thesis that have been taken verbatim or in spirit from publications or other external texts have been identified by me as such. Furthermore, I declare that this thesis has not been used, not even in part, for any other examination.

Erklärung nach § 39 (15) Prüfungsordnung 2020 für den MA-Studiengang Physik:
Hiermit erkläre ich, dass ich die Arbeit selbstständig und ohne Benutzung anderer als der angegebenen Quellen und Hilfsmittel verfasst habe. Alle Stellen der Arbeit, die wörtlich oder sinngemäß aus Veröffentlichungen oder aus anderen fremden Texten entnommen wurden, sind von mir als solche kenntlich gemacht worden. Ferner erkläre ich, dass die Arbeit nicht - auch nicht auszugsweise - für eine andere Prüfung verwendet wurde.

Merle Luisa Wälde